

**DEVELOPMENT OF RAPID ASSESSMENT TOOLS
FOR STRUCTURAL MEMBERS USING
ULTRASONIC STRESS WAVE TECHNIQUES**

by

Andrew Chen

A thesis submitted to the Faculty of the University of Delaware in partial fulfillment of the requirements for the degree of Master of Civil Engineering

Fall 2013

© 2013 Andrew Chen
All Rights Reserved

**DEVELOPMENT OF RAPID ASSESSMENT TOOLS
FOR STRUCTURAL MEMBERS USING
ULTRASONIC STRESS WAVE TECHNIQUES**

by

Andrew Chen

Approved: _____
Thomas Schumacher, Ph.D.
Professor in charge of thesis on behalf of the Advisory Committee

Approved: _____
Harry W. Shenton III, Ph.D.
Chair of the Department of Civil & Environmental Engineering

Approved: _____
Babatunde Ogunnaike, Ph.D.
Dean of the College of Engineering

Approved: _____
James G. Richards, Ph.D.
Vice Provost for Graduate and Professional Education

ACKNOWLEDGMENTS

It has been my honor and privilege to work with my advisor, Thomas Schumacher. Since the first day I met him and decided I wanted to learn from him, I have never doubted his sincere passion for his work and for guiding his students as they make their own paths. As a mentor, he has set an exemplary standard of how to approach and conduct research. But more than that, his enthusiasm and genial nature has provided much needed motivation for me to finish the thesis that not very long ago, I never imagined I would undertake. Yet, persistence has paid off and I owe Thomas my sincerest thanks for being the example that I needed.

During my time at the University of Delaware, I have had the opportunity to meet and get to know a variety of people. My time with fellow graduate students has contributed greatly to my overall experience. I am grateful for the friends that I have made and for their assistance and camaraderie.

Most of all, there is one person who has made all the difference. We came into each other's lives by chance. Yet, you were always there listening, as I whined about my research and threatened to quit. You helped me find the reason and the will to keep going, even when I did not know any remained. Thank you, Adam Faranda.

TABLE OF CONTENTS

LIST OF TABLES	vi
LIST OF FIGURES	vii
ABSTRACT	xii

Chapter

1	INTRODUCTION	1
1.1	Safety of Bridges	1
1.2	Ultrasonic Testing	2
1.3	What's Missing in NDT?.....	4
1.4	Ultrasonic Wave Propagation.....	6
2	ACOUSTOELASTICITY	11
2.1	Research Goal.....	11
2.2	Limits of Ultrasonic Testing.....	12
2.3	What is Acoustoelasticity?	15
2.3.1	Connection to Photoelasticity.....	19
2.3.2	Departure from Elastic Theory.....	20
2.3.3	The Case for Nonlinear Shear Waves	22
2.3.4	Complications.....	24
2.3.5	Contributing Factors	25
2.3.5.1	Environmental and Structural Factors	26
2.3.5.2	Micro-cracking	29
2.4	Acoustoelasticity Experiment Using Polarized Ultrasonic Shear Waves	32
2.4.1	Specimens and Test Setup.....	32
2.4.2	Testing Overview	35
2.4.3	Finding the Optimal Frequency.....	41
2.4.4	Effects of Cyclic Loading.....	42
2.5	Data Processing and Analysis	47
2.5.1	Frequency	47
2.5.2	Filtering	51
2.5.3	Time of Flight.....	56
2.5.4	Different Options in Computing Time of Flight	63

2.6	Results and Discussion	68
2.6.1	Advantage of Acoustoelasticity.....	68
2.6.2	Effects of Cyclic Loading.....	72
2.7	Conclusions and Future Work.....	84
3	DIFFUSE WAVE FIELDS	87
3.1	Research Goal.....	87
3.2	What are Diffuse Wave Fields or Coda Waves?	88
3.2.1	Development of Methodology.....	89
3.3	Coda Wave Experiment.....	92
3.3.1	Specimens and Test Setup.....	92
3.3.2	Testing Overview	96
3.4	Data Analysis.....	97
3.4.1	Cross-correlation	100
3.4.2	Magnitude-squared Coherence	101
3.4.3	Fixed vs Sliding Windows.....	103
3.5	Results and Discussion	104
3.5.1	Static Windows.....	104
3.5.1.1	Passive Measurements.....	104
3.5.1.2	Active Measurements	106
3.5.2	Sliding Window.....	110
3.5.2.1	Receiver 1	110
3.5.2.2	Receiver 2.....	117
3.6	Conclusions and Future Work.....	120
4	CONCLUSIONS	122
4.1	Conclusions	122
4.2	Future Work.....	123
	REFERENCES	124

LIST OF TABLES

Table 1:	Tested specimens.....	33
Table 2:	Numerical values of bilinear regression shown for Cylinder 2 for received signal's positive peaks.....	67
Table 3:	Block 2 adjusted r-square values and slope of linear fit for each loading and unloading cycle.....	75
Table 4:	Block 1 adjusted R-square values and slope of linear fit at shown loads	79
Table 5:	Linear fit values corresponding to specified windows analyzing <i>MSCI</i>	109

LIST OF FIGURES

Figure 1:	Isotropic wave radiating from a transmitter (source) to a receiver	7
Figure 2:	Longitudinal waveform (top) and shear waveform (bottom), showing wavelength and direction of particle motion [12].....	8
Figure 3:	Ultrasonic transducer configurations: (a) direct; (b) semidirect; and (c) indirect [1]	15
Figure 4:	Principal stress field for an initially isotropic body.....	17
Figure 5:	Relative sizes of test specimens	33
Figure 6:	Test setup for ultrasonic shear wave measurements, showing cross section of concrete specimen.....	35
Figure 7:	Ricker wave used in below FE simulation	36
Figure 8:	2D Finite element simulation of wave propagation in concrete showing p-wave and s-wave components from a shear pulse input polarized vertically at (a) $t = 0.01$ ms, (b) $t = 0.02$ ms, (c) $t = 0.03$ ms and (d) $t = 0.05$ ms. Boundary reflections are shown in (c) and (d)	37
Figure 9:	Diagram of ultrasonic transducers attached to concrete, oriented (left) parallel to applied stress and (right) perpendicular to applied stress, shear waves polarized along Axis 2, in directions 1 and 3	39
Figure 10:	(left) Concrete cylinder setup and (right) same cylinder at failure	40
Figure 11:	(left) concrete block with shear transducers and (right) compression machine and data acquisition system, DAQ.....	40
Figure 12:	Concrete block specimen in compression machine with bearing pads on the top and bottom.....	43

Figure 13:	Loading and unloading cycles for Block 1, specimen failing at 110 kips load.....	44
Figure 14:	Concrete block 1 failure: (left) side view and (right) top view	45
Figure 15:	Loading and unloading cycles for Block 2, specimen failing at 115 kip load	46
Figure 16:	Transmitted excitation and received signals (normalized) at 25, 50, 75 and 100 KHz (top to bottom).....	47
Figure 17:	Cylinder 1 shear wave readings at 25 KHz, not aligned at same origin.....	49
Figure 18:	Cylinder 1, <i>time of flight</i> ratio increasing as function of applied stress	51
Figure 19:	FFT of (top) input wave with center frequency of 50 kHz, (mid) unfiltered received signal and (bottom) received signal with applied bandpass filter	52
Figure 20:	(top) unfiltered received signal at unloaded state and (bottom) signal with applied bandpass filter	54
Figure 21:	Comparison of received signal from transmitted waveform at (top) 50 kHz and (bottom) 100 kHz frequency, all else the same	55
Figure 22:	Example of normalized transmitted input signal (green, left) and received signal (blue, right) with the elapsed TOF labeled.....	57
Figure 23:	Received signals at 5 kip load for both polarized shear waves	60
Figure 24:	Difference between signals in transverse direction at different applied stresses, magnification showing change in the <i>time of flight</i>	60
Figure 25:	Combined <i>TOF ratios, B</i> using Equation (8)	62
Figure 26:	Cylinder 2 comparison of wave velocity calculated with input wave and chosen (top) second positive peak and (bottom) sixth peak of the received wave	64
Figure 27:	The <i>TOF</i> bilinear fit lines shown in with 95% confidence (green) and prediction (blue) limits for different peaks for Cylinder 2	66

Figure 28:	Comparison of residuals for bilinear regression of <i>time of flight</i> ratios for Cylinder 2.....	67
Figure 29:	Calculated individual <i>TOFs</i> (left) and combined <i>TOF ratios, B</i> (right) with marked regions at percentage of ultimate strength for Cylinder 2	70
Figure 30:	<i>TOF</i> of loading cycles for (left) 21 direction, parallel to stress and (right) 23 direction, perpendicular to stress for Block 1.....	73
Figure 31:	Block 1, <i>time of flight</i> ratios for each successive loading cycle until failure (five total)	77
Figure 32:	Block 2 successive (left) loading and (right) unloading cycles shown with <i>time of flight</i> ratios and fitted linear regression and corresponding 95% confidence intervals.....	78
Figure 33:	(left) Total <i>time of flight</i> ratios for each loading cycle at 5, 25 and 50 kips in the Block 1 experiment and (right) corresponding <i>time of flight</i> for the separate directions	81
Figure 34:	Block 2, <i>time of flight</i> ratios recorded for the same load over the course of several loading cycles	82
Figure 35:	<i>Time of flight</i> ratios for each (top) loading cycle and (bottom) unloading cycle in Block 2	83
Figure 36:	Entire recorded signal of Plate 2 baseline and with (a) 1 mm groove and magnified portion of (b) coherent and (c) incoherent (diffuse) portion of wave field.....	90
Figure 37:	Point-contact sensor used in the experiment	93
Figure 38:	Dimensions of test setup for (top) Plate 1 and (bottom) Plate 2	94
Figure 39:	Test setup for ultrasonic wave measurements with Glaser/NIST point-contact sensors for Plate 2 to measure signals with increasing groove size. The direct (= shortest) wave paths are indicated by red arrows	95
Figure 40:	(left) Test setup for Plate 2 with one transmitter T and two receivers S1 and S2 and (right) close up of sensor mount with attached cable at S2	97

Figure 41:	Selection of possible travel paths to arrive at given receiver, for waves traveling through plate and reflecting off flaws and boundaries.....	98
Figure 42:	(top) Analyzed portion of Plate 1 signal divided into four equal windows with (bottom) zoom-in of initial wave arrival at the receiver	99
Figure 43:	Example of <i>MSCI</i> (<i>MSC Integral</i>) = 1.0	102
Figure 44:	Example of <i>MSCI</i> (<i>MSC Integral</i>) = 0.2	102
Figure 45:	(top) <i>MSCI</i> values and (bottom) cross-correlation plotted vs change in groove depth for Plate 1	105
Figure 46:	<i>MSCI</i> values for Plate 1 (top) comparing the entire signals of different groove depths with reference and (bottom) using four static windows	107
Figure 47:	<i>MSCI</i> values in Plate 1 analyzing the signal in 100 static windows.....	109
Figure 48:	(top) <i>MSCI</i> between the baseline and signals from the grooved Plate 2, Receiver 1 with noise shown as shaded area and (bottom) the coefficient of variation (<i>CV</i>) showing dispersion between all sets of <i>MSCI</i> with first wave arrival and point of maximum dispersion marked with dashed lines.....	111
Figure 49:	Magnification of first arrival of ballistic (direct) waves shown as <i>MSCI</i>	113
Figure 50:	Amplitude comparison between (top) baseline signal and increasing groove size signals in time window in early portion of coda and (bottom) later in the coda as waves continue to scatter in the plate	115
Figure 51:	<i>MSCI</i> as function of damage level between entire recorded signal and results of time window approach with fitted exponential regression models (left) and magnified plot of the same results (right) for Receiver 1	116

Figure 52: (top) *MSCI* between the baseline and signals from the grooved Plate 2, Receiver 2 with noise shown as shaded area and (bottom) the coefficient of variation (CV) showing dispersion between all sets of *MSCI* with first wave arrival and point of maximum dispersion marked with dashed lines..... 118

Figure 53: *MSCI* as function of damage level between entire recorded signal and results of time window approach with fitted exponential regression models (left) and a magnification of the same results (right) for Receiver 2 119

ABSTRACT

The requirements for inspecting a structure depend on a variety of factors, including: routine inspections, change in operating conditions, rehabilitation, accidents and after extreme events. Although visual inspections are generally adequate for maintaining the safety of most structures, if quantitative information is required, then non-destructive testing (NDT) techniques are needed. Methods of rapidly estimating in-situ stresses and characterizing flaws in structures are both highly desirable for supplementing visual inspections. Currently, there is no existing NDT method for determining in-situ stresses in a concrete member. Additionally, established methods of characterizing flaws in steel members are generally time consuming and most do not allow for remote monitoring. The objective of this research is twofold: to test the viability of using (1) polarized ultrasonic shear waves to estimate in-situ stresses in concrete members and (2) analysis of diffuse ultrasonic wave fields for detecting and characterizing flaws in a steel member. This thesis establishes basic research for these two subjects and covers the fundamental observations derived from experimental testing, signal and data processing. The results demonstrate that the two approaches could potentially be used in an integrated method for monitoring changes in the integrity of structural members remotely.

Chapter 1

INTRODUCTION

1.1 Safety of Bridges

A bridge is an extraordinarily complex system. Under typical conditions, it will be in operation from the day it opens to the day it is decommissioned. As structurally deficient and functionally obsolete bridges deteriorate, they threaten the safety of everyone travelling over them or in the immediate area. Furthermore, a structural failure can be a major disruption in the transportation network, resulting in major economic and social cost. In order to avoid any catastrophic failures, structural inspections are performed regularly to meet local, state and federal mandates.

The requirements for inspecting a bridge depends on a variety of factors, including: routine inspections, change in operating conditions, rehabilitation, accidents and after extreme events. Although visual inspections are generally adequate for maintaining the safety of most structures, if quantitative information is required, then non-destructive testing (NDT) techniques are needed. Ultrasonic stress wave methods have been investigated in pursuit of these goals since they are relatively inexpensive and safe compared to other NDT methods, adaptable to different situations and sensitive to microscopic changes in a material. Some examples of ultrasonic

applications include estimation of member thickness, detection of discontinuities and corrosion, or characterizing materials [1].

Potential applications for the latter include estimation of prestressing forces or evaluation of load distribution in walls or columns after extreme events. Currently, there is no accepted method for determining in-situ stresses in a concrete structure non-destructively [2]. Additionally, established methods of characterizing flaws in steel members are generally time consuming and most do not allow for remote monitoring. This thesis covers research that evaluates two techniques that are fast, robust, and can be implemented into a monitoring scheme. Specifically, Chapter 2 investigates polarized ultrasonic shear waves to estimate in-situ stresses in concrete members and Chapter 3 investigates analysis of diffuse wave fields for detecting and characterizing flaws in a steel member.

In this remainder of this chapter, we review the general concepts involved in ultrasonic testing that will be utilized in explaining the experiments covered in Chapter 2 and Chapter 3. This includes:

- An introduction to ultrasonic testing (Sections 1.2)
- The benefits to developing new NDT techniques (Section 1.3)
- The fundamentals of ultrasonic wave propagation (Section 1.4)

1.2 Ultrasonic Testing

While no technology is appropriate in all situations, certain types of testing have advantages over others in structural inspection and monitoring applications. In 1929, Sokolov first proposed to use ultrasound to detect flaws in steel that were not

detectable by the human eye [3]. Then in the 1950s, researchers started developing methods to evaluate and characterize material properties. By measuring ultrasonic wave velocities, they were able to analyze the effects of temperature and external loading on a material. By measuring ultrasonic attenuation and its change with frequency, they were able to analyze the effects of heat treatments on a material's microstructure. Since then, many researchers have developed other applications for ultrasonic testing.

In structural engineering applications, the most commonly evaluated materials are concrete and steel. In particular, structural concrete is the most prevalent manufactured construction material used across the world [4]. In the US, much of the existing infrastructure has already exceeded its original design life [5]. Detecting any problems in a structure would not only aid in keeping the public safe, but would also reduce overall maintenance and rehabilitation costs. Visual and NDT inspections both can contribute towards a more accurate estimate of the remaining service life of a structure.

Compared with other NDT methods, ultrasonic techniques provide a cost-efficient, mobile and relatively safe means for detecting discontinuities (e.g. voids or cracks), material properties, obtaining thickness measurements or many other characteristics. Moreover, there are techniques that have been used to monitor deterioration and to estimate strength and stiffness over time [1] [6]. Although there are many factors that influence the behavior of ultrasonic waves in structural materials, this study seeks to establish some basic information regarding some of these factors. The context is the

effect of acoustoelasticity in concrete and diffuse wave fields in steel with an end goal to establish quantitative information about changes in the materials.

1.3 What's Missing in NDT?

There is an ever increasing need for nondestructive testing (NDT) and structural health monitoring (SHM) techniques for validating the effectiveness and condition of civil structures. To this end, ample research has been dedicated not only to methods for detecting and characterizing flaws, but also in estimating stresses in structural members.

Yet, most established methods for determining residual stresses in metal elements are destructive [7]. For in-services structures, this is normally not a feasible option. By using NDT, it is possible to better understand the structural health of a bridge and more accurately assess its remaining service life. Bridges generally consist of a combination of steel, concrete or concrete-encased prestressed components. Thus, the ability to estimate the strength of early age concrete is critical in knowing whether formed elements are ready to be released, bridges can be opened to traffic, or when prestressing can be applied [8]. Moreover, since long term effects (creep, shrinkage, relaxation) in prestressed members decrease stresses in concrete, it would also be beneficial to monitor the prestressing forces over time [2]. If there were a sudden unloading of a prestressing tendon, this usually equates to a major failure in the structure [9]. Even considering the use of NDT, this broad category encompasses many different technologies, each with its own set of advantages and limitations.

For any given engineering application, there is likely more than one unique approach for solving it. Although a certain approach may be widely accepted for a

particular use, it may be limited in its scope and a different technology altogether may potentially be able to address it. For instance, applied stresses in bridges are usually estimated by measuring strain from the surfaces of the structure. Although this is an accepted form of NDT, this is a time-intensive process and limited in use. This method can only measure additional strains, typically as a result of live load from vehicle traffic. The absolute strain (and stress) in a member remains unknown.

In contrast, ultrasonic testing has potential for surpassing this limitation and could potentially be able to provide results in a shorter time frame. One approach for changing this situation is evolving through the study of acoustoelasticity (further examined in Chapter 2). Acoustoelasticity has more commonly been applied to steel materials using bulk waves to study railroad tracks or bolts, or welded structures. Since this involves the detection of small changes in wave velocity, surface waves have also been used in an attempt to maximize the sensitivity in steel [9]. Although concrete behaves differently than steel, ultrasonic testing using acoustoelasticity has also been adapted for use in concrete in recent years [10].

Similarly, research in ultrasonic diffuse waves has largely been focused on the testing of metallic materials due to fewer complicating factors. In general, ultrasonic technology has been widely used for flaw detection and characterization [1]. Although there exist methods for performing this type of testing, there are limitations in how quickly, accurately and comprehensively the monitoring of a given in-service structure can be. A significant component is due to influences from environmental factors [11]. Even holding these constant, there remain significant signal and data processing challenges to contend with when dealing with diffuse waveforms (explained in Chapter 3). To

understand the varying inspection and monitoring processes considered in this thesis, it is critical to first have a working knowledge of ultrasonic wave propagation.

1.4 Ultrasonic Wave Propagation

Ultrasonic testing is a type of NDT with many applications for evaluating various materials. This section provides a brief review of the basics of ultrasonic wave propagation in isotropic materials. In solids, these waves can be characterized as either bulk or guided waves. An understanding of these concepts is an important prerequisite for following the later discussions on acoustoelasticity in Chapter 2 and on diffuse waves in Chapter 3.

Ultrasound refers to the range of sound waves that vibrate at frequencies higher than the range of human hearing: approximately above 20 kHz. These waves carry energy from one location to another and equate to physical displacements of points in a material from their equilibrium positions [1]. An example of a wave is the sine wave; this is mathematically associated with a frequency, wavelength and velocity. In ultrasonic testing, at least one transmitter and one receiver are required (the same device can function as both). A transducer is an electrical device that converts ultrasonic energy to a voltage based on the principle of piezoelectricity [12]. They are used to emit an ultrasonic wave pulse into a medium (= transmitter) and to record the resulting signal (= receiver) after it has travelled through the medium, respectively. When a particular waveform is induced in a material, it radiates from the contact point isotropically—in all directions—into the material (Figure 1). When analyzing the wave using ultrasonic testing, the input and output signals are measured in volts (V).

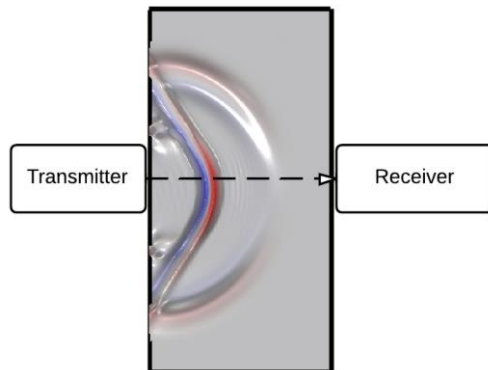


Figure 1: Isotropic wave radiating from a transmitter (source) to a receiver

As the wave travels and spreads out from the source, it loses energy as it is distributed across a spherical volume. As it travels across distance through a solid, it also loses energy through *attenuation*, until the wave can no longer be detected [12]. This means that the amplitude of the voltage decreases over time. This *attenuation* is attributed to a combination of *absorption* and *scattering*. During the course of propagation, a wave loses some energy to heat as potential is converted to kinetic energy (*absorption*). It can also be *scattered* when it reaches a boundary, whether between the interface of different materials or a discontinuity (including local changes in a heterogeneous material); as a result, a fraction of the energy is reflected isotropically. In solids, waves can also be *dispersed* as a result of local changes in material, changing the shape of the waveform as it propagates. While each of these effects should be considered in an ultrasonic test, the effect of scattering is of particular interest to the study of diffuse waves in Chapter 3.

In ultrasonic testing, the types of waves are divided into either bulk waves, surface, or plate waves. While surface waves propagate only along the interface between two different materials (e.g. a solid structure and air), bulk waves propagate

through a material. Plate waves exist in thin materials only and are dispersive, i.e. the velocity is a function of the frequency. Bulk waves are not dispersive and the type that this thesis focuses on; this category is divided into *longitudinal* and *shear* (transverse) waves. Each has a direction of wave propagation and a direction of particle motion. As seen in Figure 2, the difference is that while *longitudinal* waves have particle motion in the same direction as its travel path, the particle motion of a *shear* wave is perpendicular to the direction of propagation.

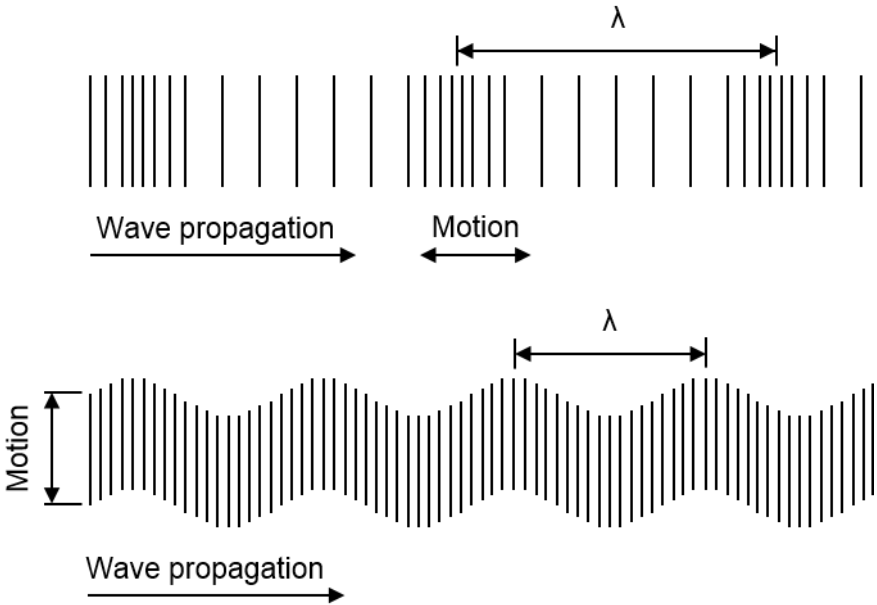


Figure 2: Longitudinal waveform (top) and shear waveform (bottom), showing wavelength and direction of particle motion [12]

Each wave has a given wavelength λ , which is associated with its frequency f and velocity v through the following relationship:

$$\text{wavelength, } \lambda = \frac{v}{f} \quad (1)$$

Many ultrasonic testing techniques establish relationships between the received signals and stresses or material properties of a structural member by measuring changes in velocity or attenuation. Since bulk wave velocity is dependent on wavelength, this is an important parameter to consider when performing a test; the choices depend on the available equipment, the studied materials and the method of analysis. Typically, the *time of flight (TOF)* is used to correlate the ultrasonic wave behavior to certain analyzed variables. The *TOF* is generally considered the time elapsed between when the wave pulse is emitted into a material from the source and the time when it is first detected at the receiver. This first arrival corresponds with the shortest possible path that the wave travels. The theories explaining the mechanisms determining how long it takes for a wave to travel in a medium is generally broken into linear and nonlinear systems [13].

The techniques focusing on linear ultrasonic testing are well established. Although linear wave equations adequately simplify analyses for certain applications such as estimating material properties, they are technically only valid for members in a stress-free state. In considering acoustoelasticity, which expresses the relationship between wave velocity and stress, this is not possible. Thus, nonlinear methods are necessary. The corresponding equations are similar to the linear ones, except they also

include higher-order elastic terms. The difference between these two classes of methods is described more thoroughly in Section 2.3.2. Other methods do not directly consider the change of velocity from the direct waves. This is the case when analyzing diffuse wave fields. Instead of focusing on the beginning portion of a recorded signal, the analysis focuses on the information gathered after that. This class of analysis is explained in Section 3.2.

Chapter 2

ACOUSTOELASTICITY

2.1 Research Goal

There are many difficulties in developing a consistent, repeatable and directly applicable method for analyzing concrete structures. Guided ultrasonic waves have been used for monitoring prestressed components (e.g. steel strands, bars and anchorage bolts) on elongated civil waveguide structures using acoustoelastic theory [14]. However, literature shows that currently in-situ tests are only able to offer qualitative results [15].

It is well known that ultrasonic wave velocity is affected by the amount and type of aggregate in concrete, as well as internal discontinuities (e.g. cracks and voids). Additionally, since concrete is a porous material, moisture content and curing conditions also impact ultrasonic wave speed [1]. At the same time, these factors also affect the strength of concrete.

The nuances of concrete behavior are endless. In this chapter, we seek to use basic research to gain a better understanding of the behavior of ultrasonic waves in concrete. This focuses on a departure from classic linear elastic wave propagation theory and centers on the theory of acoustoelasticity, which details a nonlinear relationship between wave velocity and applied stress. Through experimentation, we

draw conclusions about the relationship between ultrasonic shear wave velocity and applied stress in concrete. We developed the methodology explained in the following sections with the intent that this resulting basic research will ultimately be useful for estimating in-situ stresses in concrete structures.

In Section 2.2, we first start by examining some of the difficulties of using ultrasound to test concrete structural members. Section 2.3 then follows with a history of acoustoelastic theory and an explanation of how it can be used to analyze the behavior of concrete. This leads into an overview of the experiments performed in this study in Section 2.4, followed by the analysis and discussion in Sections 2.5 and 2.6.

2.2 Limits of Ultrasonic Testing

Since the effect of ultrasonic wave propagation in concrete is affected by a multitude of factors, for any test to be repeatable it is necessary to identify the contributions of each. In a comprehensive monitoring scheme for an in-service structural member, the behavior of that particular material composition must be understood. Given that each factor itself (e.g. aggregate content or moisture content) can be research project by itself, it is not within the scope of this project to analyze each contribution.

Since the purpose of this research is to gain a better understanding of stress in a particular element, it follows that knowledge of the concrete strength is first required. Thus, compressive strength is the first factor we consider. It is possible to roughly estimate this by assuming that there is a relationship between the stiffness and density

of a material and its strength. The longitudinal wave speed in an elastic isotropic and homogeneous material is defined as:

$$V = \sqrt{\frac{KE}{\rho}} \quad (2)$$

where $K = \frac{1-\mu}{(1+\mu)(1-2\mu)}$; E = modulus of elasticity; μ = Poisson's ratio; and

ρ = density. For a review of ultrasonic testing, please refer to Section 1.4.

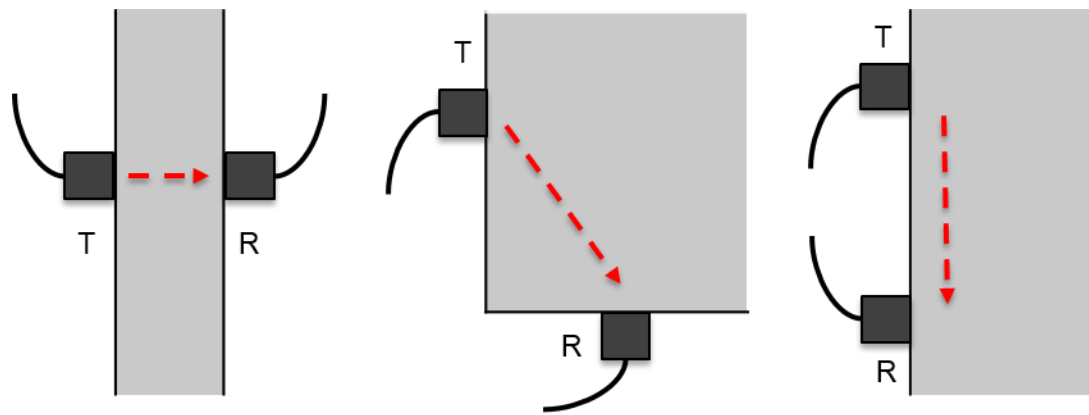
Equation (2) can be compared to previously determined correlations between wave velocity and strength. However, this is problematic for a number of reasons, particularly for concrete. Firstly, the stress-strain curve is nonlinear. Secondly, the relationship between velocity and strength is dependent on factors such as aggregate content, moisture and curing conditions. Also, since acoustoelasticity is sensitive to small changes, the actual heterogeneous nature of concrete and local material differences complicates the results and can result in large errors [1].

Furthermore, research has shown that damage in the form of cracks disrupts the linear relationship between ultrasonic wave velocity and strength of concrete. Both micro- and meso-level cracks can contribute to nonlinear terms in the damaged concrete. As a result, the linear approach of directly measuring wave velocity or attenuation produces inaccurate results [15]. Consequently, the simplified linear elastic

assumption would be inadequate for an in-situ quantitative test. However, these factors can be mitigated using a nonlinear approach using modern acoustoelastic theory.

Another complication is that structural steel normally also includes steel reinforcement. Not only are ultrasonic wave speeds higher in steel than concrete, but the behavior of each is also influenced differently by a variety of factors. It is possible in some cases to take test readings in order to avoid steel in the wave path. For certain applications, it may be even be possible to use correction factors to account for the different materials [16]. However, this typically involves a degree of undesirable simplification and in situations with a high degree of reinforcement, this may not be possible at all.

Moreover, it is important to maintain consistent contact between the transducers and concrete surface to ensure no additional error is introduced. Assuming a consistent coupling method is established, there are also different configurations for placing transducers on a material. While through-thickness (direct) transmission is preferred – thus preserving the maximum energy in the system – this is not always possible. Due to practical constraints, there are situations where access is limited and a semi-direct or indirect configuration may be used (Figure 3) [1]. However, due to lower resulting amplitudes, these configurations must contend with the lower signal-to-noise ratio. For the sake of simplicity, this chapter only considers situations where direct transmission (pitch-catch) configurations are possible (case (a)).



T = transmitting transducer
R = receiving transducer

(a)

(b)

(c)

Figure 3: Ultrasonic transducer configurations: (a) direct; (b) semidirect; and (c) indirect [1]

2.3 What is Acoustoelasticity?

The modern theory of acoustoelasticity originated in 1953 with Hughes and Kelly, expanding on Murnaghan's laws of nonlinear elasticity. The acoustoelastic effect refers to stress-induced anisotropic behavior caused by nonlinear strain in an isotropic solid. In effect, the speed of elastic ultrasonic waves propagating through the solid depends on the elastic deformation of the body [17]. This effect has been studied for both longitudinal and shear waves polarized in different directions travelling either parallel or perpendicular to the stressed axis [18].

Starting in the 1800s, Cauchy initially derived some of the fundamental equations for the theory of finite deformations, with Love extending this work [17]. Afterward, Brillouin and Murnaghan revised and extended the formulation of the original equations. In 1951, Murnaghan introduced the three *third-order elastic constants (TOEC)* l , m and n as additions to the well-known *second-order elastic Lamé constants (SOEC)* λ and μ in a Lagrangian coordinate system. The strain energy relationships were taken a step further by Hughes and Kelly [17].

In 1953, they used Murnaghan's *TOECs* to develop analytical equations to relate ultrasonic wave velocity and stress in a homogeneous isotropic material [4]. Hughes and Kelly formulated the governing equations of acoustoelasticity and confirmed their theory with the testing of Polystyrene, Armco iron and Pyrex (three materials with significantly different elastic properties). They presented a set of five equations for determining the *SOECs* and *TOECs* in terms of strain energy: two for hydrostatic and three for uniaxial pressure. With these, it is possible to calculate the *TOECs* in solids using three measurements of changing wave velocity [17].

Following their pioneering work, Benson and Raelson [19] as well as Bergman and Shahbeder [20] respectively established in 1958 and 1959 that the behavior of elastic waves in metallic materials under stress is directly dependent on the direction of propagation. The effect of stress is different for each wave as an applied stresses causes an initially isotropic material to behave anisotropically. This behavior is analogous to photoelasticity, which is based on the principle of birefringence and has been used to visualize stress in transparent bodies from changes in light speed [3]. As

the waves propagate, these produce small deformations in a material undergoing finite deformation from applied stress [21]. Since these early years, continual research has been performed from the engineering perspective and shown that experimental results support the theoretical relationships.

Building on this foundation, in 1967 Crecraft evaluated the potential for using acoustoelasticity for measuring residual stress in metallic engineering components [22]. Figure 4 shows a common convention for establishing stress axes used in literature. Crecraft imposed uniaxial tension on metallic specimens along Axis 1 and propagated longitudinal waves and shear waves along Axis 2 – where the shear waves are polarized along Axes 1 and 3. Through multiple experiments, he confirmed the proportional relationship between wave velocity and applied stress.

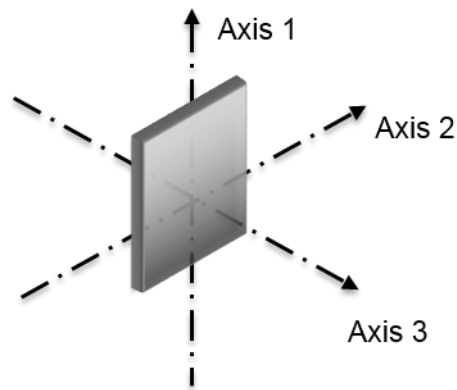


Figure 4: Principal stress field for an initially isotropic body

It is important to note that this only holds when elastic strains are small. As long as this condition is satisfied, the difference in wave speed between two polarized shear waves is proportional to the difference in principal stresses [3]. This equates to the underlying assumption that acoustoelasticity is applicable only within the elastic region of a given material.

In 1976, Egle and Bray demonstrated that it was possible to measure the effects of acoustoelasticity in rail steel by polarizing ultrasonic waves in different orientations. For the first time, the changes in wave speed were compared to elastic strain. They determined that longitudinal waves propagating parallel to the stress axis (Axis 1) showed the largest change in speed as axial strain increased. In addition, shear waves propagated along Axis 2 were more sensitive to changes in stress and strain when polarized along the stress axis, compared to the perpendicular direction [18]. Typically though, most research conducted on steel and concrete only experimentally measure stress and not strain [10] [23] [24]. This difference between the results that can be obtained in different polarized directions is integral to the experimental analysis explained later in Section 2.6.

The primary points of discussion relevant to the experimental analysis considered in this chapter are summarized:

1. Linear elastic theory provides an inaccurate expression of the effect of stress on ultrasonic velocity (Section 2.3.2).
2. Detecting nonlinear changes requires high sensitivity measurements and can be achieved using shear waves (Section 2.3.3).

3. Several factors influence ultrasonic velocity, including material composition and micro-cracking (Section 2.3.5).

2.3.1 Connection to Photoelasticity

The results of acoustoelasticity research demonstrate that a normally isotropic elastic medium behaves anisotropically when it is subjected to an applied stress. This translates into a change in the velocity of shear waves traveling through a solid, dependent on the direction of wave propagation. This behavior is related to the phenomenon observed as photoelasticity in the field of optics.

Photoelasticity demonstrates that light wave velocity is dependent on stress in transparent materials. The analogous behavior with ultrasonic waves is the reason that the term acoustoelasticity is used to describe the phenomenon in solids. When analyzing polarized shear waves and transverse light waves, the velocity depends on the direction of particle motion when the initially isotropic material is stressed [22]. Thus, both light waves and ultrasonic waves exhibit anisotropy in a stressed state.

In the past, acoustoelasticity has also been referred to as sonoelasticity or acoustic birefringence. Birefringence refers to double refraction which is studied in the field of optics. However, when dealing with ultrasound, birefringence is a misnomer. Yet, although the two behave similarly, the two do not share a one-to-one relationship. As Hsu (1974) [24] explains, although light waves are split and polarized through double refraction, elastic waves do not resolve into strictly two resultant waves. Instead, the result is one quasi-longitudinal and two quasi-transverse waves. Thus, the term

birefringence does not strictly apply to acoustic waves. The full analogy can only be satisfied if the shear wave propagates exactly along the principal symmetric axis of an isotropic solid. Thus, pre-existing texture effects and residual stresses in a given material alter the acoustoelastic relationship between wave speed and stress even in an unstressed state.

2.3.2 Departure from Elastic Theory

Classic linear elastic theory relates strain energy with first and second order coefficients, consistent with Hooke's law. However, this can only predict with reasonable accuracy the infinitesimal deformations in perfectly elastic solids (where strain is a function of only stress and temperature). In fact, it has been shown that there is a nonlinear relationship between stress and strain in different materials even at infinitesimal deformation [25]. Since higher order constants affect the strain to a lesser degree, ignoring them in linear ultrasonic methods may produce acceptable results in certain tests. When describing inelastic or plastic behavior in a material or when a tested solid is subjected to substantial deformation though, this can result in significant errors. When taking measurements requiring high precision, these higher order constants are critical. The corresponding expressions can be differentiated with respect to strain to form the elastic constants in terms of *SOECs* and the products of *TOECs* and strains [17].

In linear elastic theory, material properties such as mass density and stiffness are assumed to be constant with wave speeds dependent only on *SOECs*. Thus, they are not affected by changes in applied stress. The nonlinear behavior dependent on strain can only be represented with higher order coefficients [26]. When a material is

nonlinearly elastic (nonlinear stress-strain relationship), the change in wave speed is affected by the change in density from strain. More specifically, the speed is significantly affected by the change in the elastic modulus. By introducing *TOECs*, the stress-strain relationship changes from a linear to a quadratic approximation [22]. As mentioned in earlier, Murnaghan formulated a version of these expressions in a Lagrangian system. This derivation does not include any simplifying assumptions that had previously been used, such as the smallness of strain [27].

As implied earlier, the typical convention in a given solid medium subjected to a uniaxial load is to define Axis 1 in the direction of the stress. Axes 2 and 3 are the two perpendicular directions. The expressions for elastic wave velocities for longitudinal and shear waves in a uniaxially stressed medium are given as [17]:

$$\rho_0 v_{11}^2 = \lambda + 2\mu - \frac{\sigma_{11}}{3K} \left[2l + \lambda + \frac{\lambda + \mu}{\mu} (4m + 4\lambda + 10\mu) \right] \quad (3)$$

$$\rho_0 v_{12}^2 = \rho_0 v_{13}^2 = \lambda - \frac{\sigma_{11}}{3K} \left[m + \frac{\lambda n}{4\mu} + 4\lambda + 4\mu \right] \quad (4)$$

$$\rho_0 v_{22}^2 = \lambda + 2\mu - \frac{\sigma_{11}}{3K} \left[2l - \frac{2\lambda}{\mu} (m + \lambda + 2\mu) \right] \quad (5)$$

$$\rho_0 v_{21}^2 = \mu - \frac{\sigma_{11}}{3K} \left[m + \frac{\lambda n}{4\mu} + \lambda + 2\mu \right] \quad (6)$$

$$\rho_0 v_{23}^2 = \mu - \frac{\sigma_{11}}{3K} \left[m + \frac{\lambda + \mu}{2\mu} n - 2\mu \right] \quad (7)$$

where ρ_0 is the density; v_{ij} is the velocity of a wave propagating in direction i , polarized in direction j ; σ_{11} is the normal stress in direction 1; $\lambda, \mu = \text{Lamé's}$

coefficients; l, m, n = Murnaghan's coefficients; and bulk modulus $K = \lambda + \frac{2}{3}\mu$. The nonlinear behavior explained by these equations is not defined by the particular values of *TOECs* l, m and n but rather the ratio between these and *SOECs* λ and μ [28].

Using these equations, various crystalline materials tested by Hughes and Kelly and by Egle and Bray showed *third-order constants* l, m, n to all be negative values [17] [18]. Likewise, Payan et al. determined this to also be the case for concrete. These values are similar to those found in rocks and are two orders of magnitude greater than materials like steel [28]. The polarized shear wave Equations (6) and (7) for waves propagating along Axis 2 are of primary interest in the experimental analysis covered in Section 2.5.

2.3.3 The Case for Nonlinear Shear Waves

An understanding of residual or applied stress in a structure is relevant to structural engineers and other related professions. To this end, ultrasonic shear waves provide certain advantages over other methods. Since a bulk waves average the properties of a medium along the wave path, results are not restricted to surface measurements which are more sensitive to even structurally insignificant surface changes [22].

Although longitudinal waves propagated in the same direction as stress are more sensitive to changes, as described in the opening of Section 2.3, oftentimes the practical constraints of a structure do not allow for measurements to be taken along this axis. This additional sensitivity can actually be detrimental since it means that the measurements are more sensitive even to slight changes in material properties between

different test samples. Furthermore, the difference between the speeds of waves polarized along different stress axes is directly related to the magnitude of stress. By comparing the relative difference between the two, there is no need for a precise measurement of the wave path length. This conclusion is supported by Hsu's experiments, where relative velocity changes from applied stress in a steel specimen were the same when the waves propagated along two different path lengths [24] [22]. Other experiments studied the effect on wave velocity within specific ranges of stress.

In 1970, Shah and Chandra found no significant change in longitudinal wave velocity in compressed concrete until 90% of the ultimate strength [29]. However, this may be due to lack of sensitive in the method for collecting measurements. In a similar study, Popovics et al. (1990) determined that the longitudinal wave velocity increased with stress up to 20% of the ultimate strength and did not change significantly again until approximately 70% [30]. In another study by Shah and Hirose in 2010, they observed that the traditional ultrasonic velocity measurements only detected damage after 60% [31]. In contrast, and the results of our experimental testing also on concrete with shear waves shows that although the rate of change varies, the velocity changes consistently during the entire loading process (Section 2.6.1). This is consistent with other nonlinear ultrasonic methods for concrete [28] [31] [32]. Although shear waves have demonstrated sensitivity to changes in stress, there are complications in data collection and analysis. These are discussed in the subsequent section.

2.3.4 Complications

Traditional linear methods of ultrasonic NDT typically rely on measures of wave speed and attenuation and are useful in certain applications. However, they are not as sensitive to changes as nonlinear methods. As a result, they may not detect changes in a material's microstructure. Even with an improvement in sensitivity using nonlinear elastic theory, existing methods have not yet proven to be ready for in-situ applications. The downside to increased sensitivity is that the contribution from environmental and surface effects are also magnified and need to be identified and understood [28]. Only then can one form accurate conclusions about the state of stress in a material through changes in wave speed, separate from other effects.

Another complication is the laboratory setup versus a field setting. On one hand, the same equipment can generally be used with minor modifications and when a shear transducer is rotated about its axis, the wave is unchanged [24]. However, this means it is necessary to establish a method for fixing transducers to a structure that can be consistently rotated to approximately the same alignment over time in order to obtain meaningful results [33]. Thus, this type of testing lends itself to a permanent or long-term SHM configuration.

Although couplants improve the transmission of an elastic wave between the sensor and the test surface, they add an undesired degree of variability. While liquid couplants are commonly used to transmit compression waves, they cannot be used for shear waves. Instead, transducers can be pressed directly to a test surface to establish direct contact. Although dry contact reduces the effective contact of the respective

microstructures, shear wave transmission is still comparable to that of when using couplant. Thus, it is preferable to press the transducer against the surface directly with an applied force to maintain maximum surface contact. Since the waves are propagated perpendicular to the uniaxial stress axis, this force acts equally for both polarized measurements and thus does not affect the resulting wave speeds. Although an automated system may be preferable from a long-term monitoring standpoint, since the exact angle of perpendicular polarization minimally affects the accuracy of a stress measurement, holding the transducers by hand in a lab setting should also produce acceptable results [22] [34].

2.3.5 Contributing Factors

Since Hughes and Kelly's initial experiments over 60 years ago, extensive acoustoelasticity research has been performed on polycrystalline laboratory specimens. The effect of metallic material properties in particular on the acoustoelastic effect has been an active area of research since the 1980s [3]. While ample research has also been performed for the effect in rocks, such as for petroleum industry applications [35], the equivalent research for concrete (characterized by its complex heterogeneity) was not as prevalent for many years [29].

Ultrasonic velocity variation measurements due to concrete cracking under compression were first taken by Jones in 1952 [6]. Although other critical research had been performed during the next few decades, it wasn't until 1991 that Berthaud considered anisotropy in axially loaded concrete [36]. Based on this work, the effect of micro-crack growth and cyclic loading on the relationship between wave velocity and

stress (Section 2.3.5.2) has also been studied [6] [29]. Recently, studies specifically of the acoustoelastic effect started to emerge in the late 2000s. Some experiments relied on direct bulk wave measurements in compressed concrete lab specimens, such as those performed by Lillamand et al. [10] and Shoukuni [37]. Others utilized methods such as the *coda wave interferometry (CWI)* method for analyzing diffuse wave fields (discussed in more detail in Chapter 3) in order to measure the acoustoelastic effect [2] [4] [28] [32] [38] [39] [40]. All of these studies build on the idea that as stress changes in a material, the velocity of the wave changes with it— particularly when the particle motion is aligned in the same direction as the stress.

In order to effectively use acoustoelasticity to estimate in-situ residual or applied stresses, it is critical to obtain sensitive and accurate measurements. Acoustoelasticity has been attributed as the most sensitive bulk wave method for doing so, resulting in velocity variations on the order of 0.1% [22]. Since the changes in wave velocity are relatively small [24], the effect of other contributors would need to be distinguished from the changes due to stress. The nonlinear acoustoelastic response is linked to several factors, including environmental effects and structural composition, and microstructure changes. In turn, an understanding of the nano- to meso-scale behavior that characterizes the elastic nonlinear response can be used for applications such as predicting material strength or applied stresses [41].

2.3.5.1 Environmental and Structural Factors

Research has clearly demonstrated that variations in ultrasonic velocity due to temperature changes is a linear function of stress. This has been demonstrated experimentally in metallic alloys by Salama and Ling [42] and in concrete by Zhang et

al. [32]. In general, the temperature effect on velocity is considered negligible for many applications, unless the tested element undergoes extreme temperature (below 0 °C/-32 ° F or subject to fire) [43]. Yet, this appears to have a significant effect on sensitive measurements such as for acoustoelasticity, especially considering the possible range of temperatures encountered for structures such as bridges. In the findings by Zhang et al., the correction for temperature (± 2 °C/ 35.6 °F) reduced their standard error from $\pm 15.5\%$ to $\pm 2.7\%$. As they explain, an applied stress on an element causes geometric changes resulting in linear deformation, assumed to be uniform over the entire medium. Likewise, a change in temperature similarly affects the strain linearly. Although the theory of acoustoelasticity accounts for *SOECs* and *TOECs*, these were found to not have a significant impact on the velocity changes and were ignored in their study [4].

In most unstressed solids, there are variations in wave velocity due to initial internal anisotropy and texture [3]. Further variations beyond these are induced due to applied stress. With polycrystalline materials, texture effects typically arise as a result of grain orientation due to rolling or extrusion [44]. Due to these preferred orientations, the experimental measurements will not completely match the theoretical expressions (Section 2.3.2), which assume initially isotropic behavior [23]. These relationships are important to understand in order to establish an in-situ method of testing.

Experiments have been performed to study this sensitivity to variations in microstructure. For example, one experiment showed a linear relationship between ferrite content in steel with a measure of acoustoelasticity and another found similar results between the percentages of SiC present in aluminum [42]. It was also

determined from testing of aluminum that density varies linearly according to shear and elastic moduli and *TOECs* m and n . In contrast, l remained constant. Aside from original material composition, density can vary in a structural member from creep or fatigue [3]. This is important since material properties not only affect the strength of a material, but can also affect the ultrasonic velocity.

In concrete, there is no anisotropy due to grain orientation. However, there are several material properties which can alter the wave velocity through this material. The nonlinear response is influenced by factors such as dispersion and attenuation, which are related to aggregate content, porosity (w/c ratio) [45], and water saturation [41]. Additionally, the material structure is closely related to the microstructure, which can undergo large changes due to cracking [6].

Research has shown that although geometric variations affect velocity, these do not affect the dispersion and attenuation in concrete. Instead, these are strongly related to w/c; aggregate content and size [45]. Furthermore, since density and stiffness depend on the degree of porosity in concrete, the relationship between wave velocity and density is partially influenced by porosity. To investigate this relationship, Hernández et al. used destructive and NDT data to determine that longitudinal wave velocity in concrete would theoretically have a nonlinear relationship with porosity [46]. Afterward, Lafhaj et al. produced data matching a theoretical linear relationship between, velocity, porosity and permeability in mortar. They also found that shear wave velocity in mortar was half of the longitudinal velocity and seemed to be less sensitive to water content [47]. Despite differing models of the relationship, it is clear that porosity affects wave propagation in concrete. This is consistent with Wu and Lin's observations that velocity in mortar at a

stress-free state during cyclic loading decreases as w/c decreases. Moreover, they show that the velocity is proportional to the fine aggregate content in the mortar [29]. Despite the importance of all of these factors on the end result of ultrasonic testing in concrete, these were not explicitly considered in the context of this study. Instead, the primary characteristic that influenced the analysis was micro-cracking.

2.3.5.2 Micro-cracking

As previously discussed, Hughes and Kelly's classical theory of acoustoelasticity (Section 2.3.2) may be used when a tested element is considered as a homogeneous isotropic medium. Although concrete is heterogeneous—causing strong wave scattering—it can be simplified and considered as homogeneous when the ultrasonic pulse wavelength is large compared to the size of discontinuities (e.g. aggregates and cracks). Additionally, the isotropic assumption is generally considered a valid assumption since the aggregates are randomly distributed throughout the cement matrix and as mentioned in Section 2.3.3, bulk waves average the material properties along a wave path. Given that the velocity changes in concrete are ten times higher than in steel, the acoustoelastic effect is very sensitive to even slight changes in microstructure [10]. This is why it is important to ultimately consider all the factors that can influence the velocity in a comprehensive testing method.

Since the wavelengths used are much larger than the microscopic changes, concrete has also been demonstrated to show higher sensitivity to nonlinear parameters [25]. As concrete is compressed, it does not fracture instantaneously as a

result of excessive stress; the process begins at the atomic-molecular level and damage accumulates until it culminates in fracture at the macroscopic level. In addition to the acoustoelastic effect, the resulting decrease in ultrasonic velocity and nonlinear behavior has been attributed primarily to micro-defects: micro-pores, micro-cracks or discontinuities (i.e. voids or defects) [25]. These are subjects of considerable research in concrete, as they strongly affect wave propagation and scattering through an element.

Previous studies of ultrasonic behavior in concrete have shown that within approximately 30% of ultimate strength (the elastic region), there is a linear relationship between wave velocity and applied stress—corresponding to the classical theory of acoustoelasticity [4] [28] [29] [38] [39]. After this point, cracks are observed to rapidly increase in number and size [25]. Yet, micro-cracks and during the manufacturing process affect the elastic behavior even before an element is subject to any loading [10] [29]. Longitudinal and shear wave velocity has been observed to decrease as micro-cracking evolves even at low stress levels (below 20% stress level). The changes are small until velocity rapidly changes starting at approximately 75% of ultimate strength—corresponding to the nonlinear rapid slope change in the stress-strain diagram. Popovics et al. also observed that repetitive compressive loading up to 30% of ultimate strength showed no relation with changes to wave velocity [6] [30]. Afterward, Wu and Lin tested the range beyond this level, using three cycles of increasing load up to 50, 70 and 80% of the ultimately strength. Their findings revealed that wave velocity clearly decreased with each subsequent cycle. During the

first cycle, the total velocity change from unloaded state to the maximum cycle load was relatively small. It is evident though that each cycle changed the history of the concrete and the total velocity change increased with each additional load cycle [29].

In comparison, Shoukuni et al. studied the effect of cyclical loading on concrete using surface (Rayleigh) waves and *CWI* analysis. They observed four phases of velocity change: (1) up to 15% stress level: small changes in velocity while low stresses were inadequate to close existing micro-cracks; (2) 15 – 45%: rapid increases in velocity at low stress levels as stresses closed micro-cracks; (3) 45 – 80%: velocity increases at a slower rate as existing micro-cracks widen and new micro-cracks were formed; and (4) over 80%: velocity rapidly decreased as micro-cracks developed into macrocracks. They also concluded that micro-cracking occurred in accordance to the Kaiser effect [38].

The Kaiser effect specifies that micro-cracking only occurs if the current loading exceeds any previous loads previously applied during the life of the concrete member. This phenomenon is also corroborated by Zhang et al. using *CWI* in a through-transmission setup. This means that during the course of continual loading, irreversible strains are induced in the concrete. As a result, this shows that velocity changes from stress cannot be explained fully by acoustoelasticity, as micro-cracking also affects the behavior of the concrete. By separating the velocity changes due to reversible elastic deformation from that of irreversible changes from micro-cracking, they were able to show the acoustoelastic effect within the elastic region [4]. The influence of micro-cracking and its connection with cyclical loading is integral to

developing a method of estimating in-situ stresses in concrete and is further analyzed in Section 2.6.

2.4 Acoustoelasticity Experiment Using Polarized Ultrasonic Shear Waves

2.4.1 Specimens and Test Setup

This chapter encompasses the setup, results and analysis of four similar experiments on plain unreinforced concrete in a lab setting. The experiments referred to in this chapter are designated as shown in Table 1 and Figure 5. These are also listed in the order in which the experiments are performed; Cylinders 1 and 2 were used for continual loading and Blocks 1 and 2 were used for cyclical loading.

These prismatic unreinforced concrete specimens were the subject of the following feasibility study. The Cylinder 1 specimen measured 152 mm (6 in.) in diameter and had a height of 305 mm (12 in.). Two additional cylinders were loaded to failure to determine concrete cylinder compressive strength. Each specimen was cast in a cylindrical mold and were cured for over 28 days before being tested. The mean concrete cylinder strength at test day was 20.0 MPa (2898 psi) with a standard deviation of 1.30 MPa (186 psi). The specific cylinder presented in this paper had a concrete cylinder strength of 19.2 MPa (2790 psi). The singular Cylinder 2 was prepared similarly and had a strength of 22.1 MPa (3200 psi) at test day.

The Block 1 and Block 2 specimens were both cut from a larger slab of concrete cast in a rectangular mold and cured for over 28 days. While the remaining

specimens cut from this mold tested a mean strength of 26.1 MPa (3788 psi), Block 1 had a strength of 21.0 MPa (3046 psi) on the test day and Block 2 had a strength of 22.8 MPa (3301 psi).

Table 1: Tested specimens

<i>Test Name</i>	Tested Specimens
<i>Cylinder 1</i>	152 mm (6 in.) in diameter x 305 mm (12 in.) in height
<i>Cylinder 2</i>	152 mm (6 in.) in diameter x 305 mm (12 in.) in height
<i>Block 1</i>	152 mm (6 in.) x 152 mm (6 in.) x 305 mm (12 in.) in height
<i>Block 2</i>	152 mm (6 in.) x 152 mm (6 in.) x 533 mm (21 in.) in height

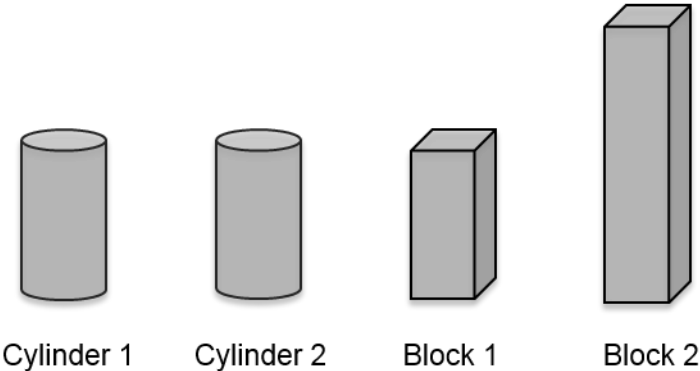


Figure 5: Relative sizes of test specimens

The vertical faces of the specimens were locally smoothed in order to ensure optimal surface contact between the transducers and the concrete. The ultrasonic shear

wave transducers were pressed against the specimen surface by hand without using any couplant. A preliminary study had shown that this method is repeatable and produces signals with sufficient amplitude and quality.

During the experiment, the concrete cylinder was loaded in a standard hydraulic concrete compression testing machine. The two identical ultrasonic shear transducers were used to transmit a polarized pulse and receive the transmitted signal. The sampling rate was 5 MHz with low-pass anti-aliasing filters set to 2 MHz. A diagram of the experimental setup is shown in Figure 6. The transducers were placed in a through-transmission (pitch-catch) configuration, with the transmitted and received signals recorded by the data acquisition system and transferred to a standard personal computer. An arbitrary waveform generator in conjunction with a high-fidelity amplifier were used to generate the input signal. In total, the equipment used for the test setup consist of:

- Elsys AG TraNET 4045 data acquisition system
- Two Olympus V153-SB 1MHz center frequency shear transducers
- KRN AMP-4BB-J amplifier (to amplify signal from receiving transducer)
- Trek 2100HF amplifier (to amplify signal from waveform generator)
- BK Precision 21.5 MHz waveform generator
- PC running TranAX data acquisition software

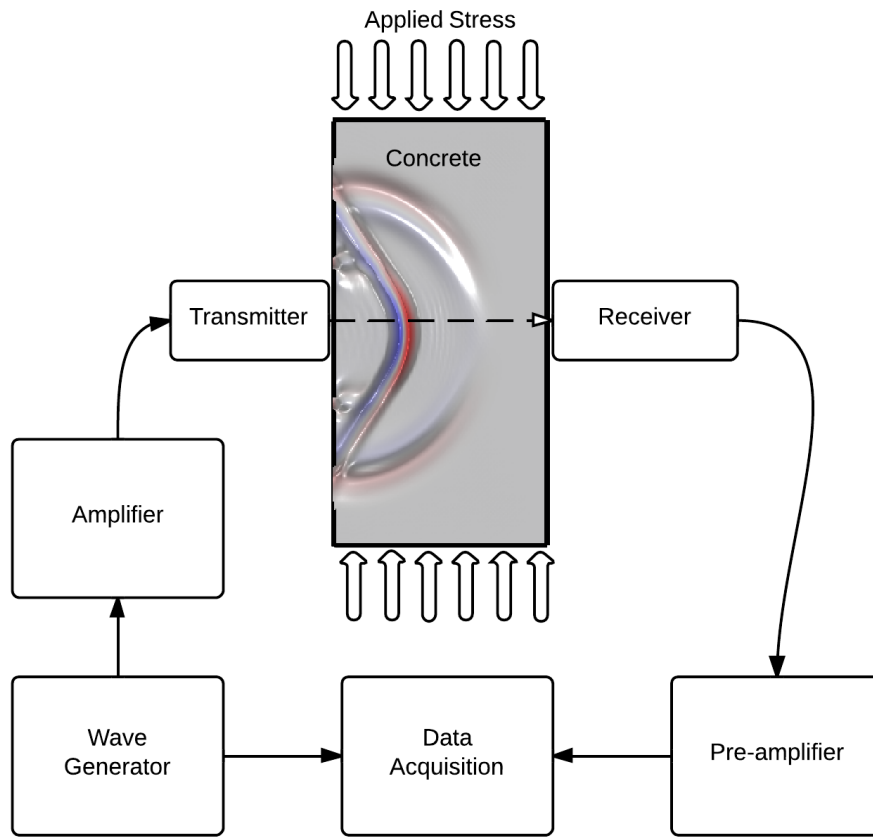


Figure 6: Test setup for ultrasonic shear wave measurements, showing cross section of concrete specimen

2.4.2 Testing Overview

To illustrate the goal of this set of experiments, first we looked at a 2D simplified finite element analysis (FEA) of the test setup. This model consisted of rectangular mapped elements in an extremely fine mesh. For demonstration, the Ricker waveform shown in Figure 7 with a singular positive and negative peak was used as the initial excitation that will propagate throughout the material. A Morlet waveform was used in the experiment (see Figure 22). The pulse was modeled to

represent a shear-type transducer that transmits a shear pulse with a particle motion oriented vertically, i.e. up and down.

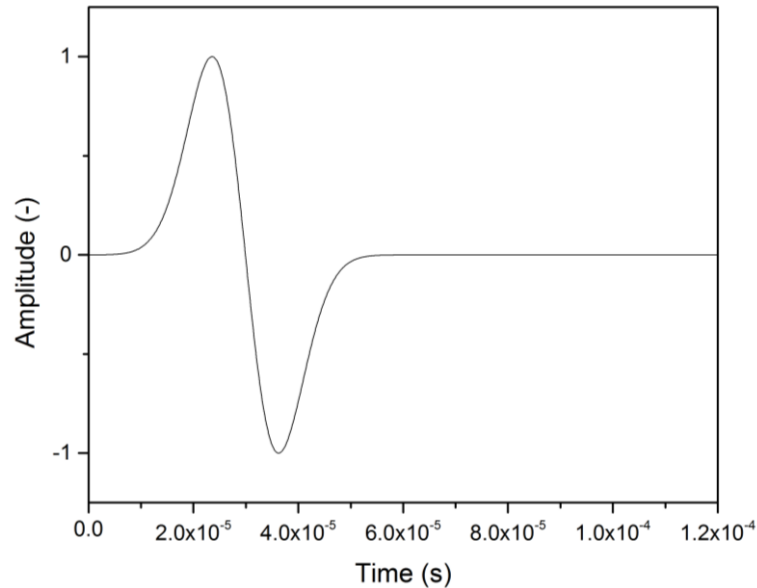


Figure 7: Ricker wave used in below FE simulation

Starting from the middle of the left boundary, the waveform spreads out in all directions. However, the area of interest is the other end of the horizontal axis, where the receiving transducer would be placed in the physical experiment. As the wave propagates through the rectangular medium, as shown the series of diagrams in Figure 8, two components of the travelling excitation pulse become apparent: the p-wave and s-waves.

While the p-wave precedes the s-wave, its magnitude is much smaller and is essentially nonexistent along the horizontal travel path and between where the

transducers will be placed. Although the p-wave will reach the opposite boundary first and initiate reflections back into the material, the behavior of the s-wave is the one of interest in this study. The first arrival of the s-wave can be seen in the last right-most frame, corresponding to the initial increase in slope from the positive amplitude of the input waveform.

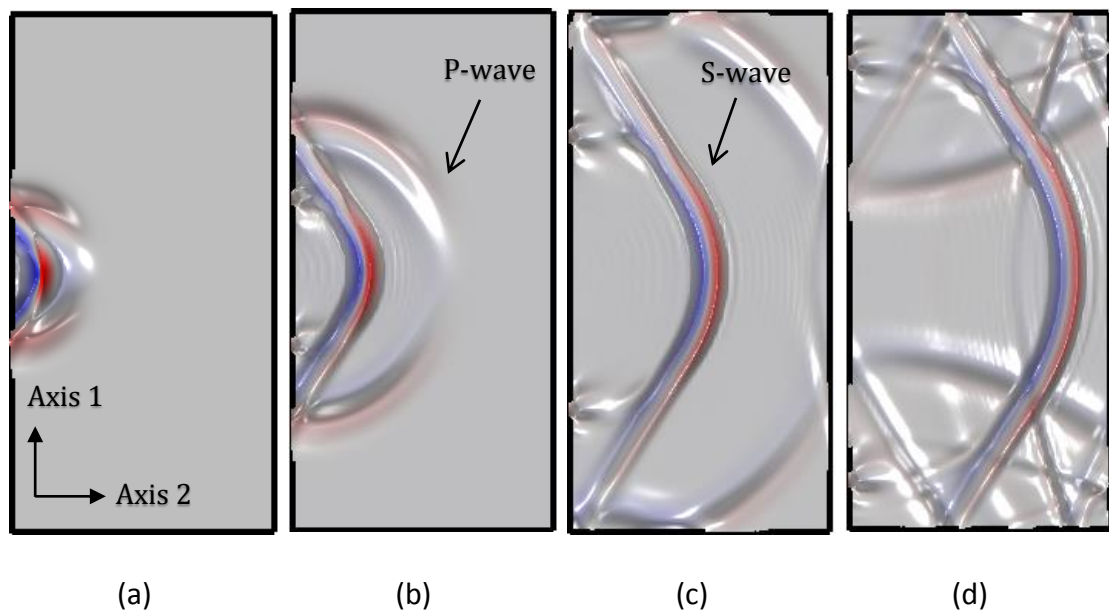


Figure 8: 2D Finite element simulation of wave propagation in concrete showing p-wave and s-wave components from a shear pulse input polarized vertically at (a) $t = 0.01$ ms, (b) $t = 0.02$ ms, (c) $t = 0.03$ ms and (d) $t = 0.05$ ms. Boundary reflections are shown in (c) and (d)

The red and blue rings indicate the positive and negative amplitudes of the waveform, respectively. While we are interested in the time it takes for the elastic wave to travel from one end of a specimen to the other, we were not concerned with

determining the exact *time of flight (TOF)* or velocity. Instead, we focused on the relative difference of velocity between vertically (1-direction) and horizontally (3-direction) polarized shear waves applied to the system.

For each of the four experiments, the concrete specimen was installed in the compression testing machine and initial reference measurements were taken in the unloaded state with the shear transducers. The transducers were manually pressed against the concrete surface with dry contact. The transmitting transducer was triggered to emit an ultrasonic shear wave at 50 kHz central frequency, which propagated through the cylinder specimen along Axis 2. Unlike the Ricker wave shown earlier to illustrate the concept of wave propagation, the actual experiments used a Morlet-type pulse (shown in Figure 22). The data acquisition system was set to start recording once a threshold of 0.5 V was exceeded at the waveform generator. Signals were recorded for a duration of 0.8 ms.

Three measurements were taken for each of the two directions: parallel and perpendicular to the applied stress. The configurations of the experimental setup at these two stages are illustrated in Figure 9, following the orthogonal axis convention introduced in the Section 2.3. Thus, there are two waves of interest in this experiment: the wave in the 21 direction and the one in the 23 direction. More specifically, the wave path between the transmitting and receiving transducer runs along Axis 2. However, the particle motion of the shear wave is aligned with either Axis 1 (parallel to applied stress) or Axis 3 (perpendicular to applied stress).

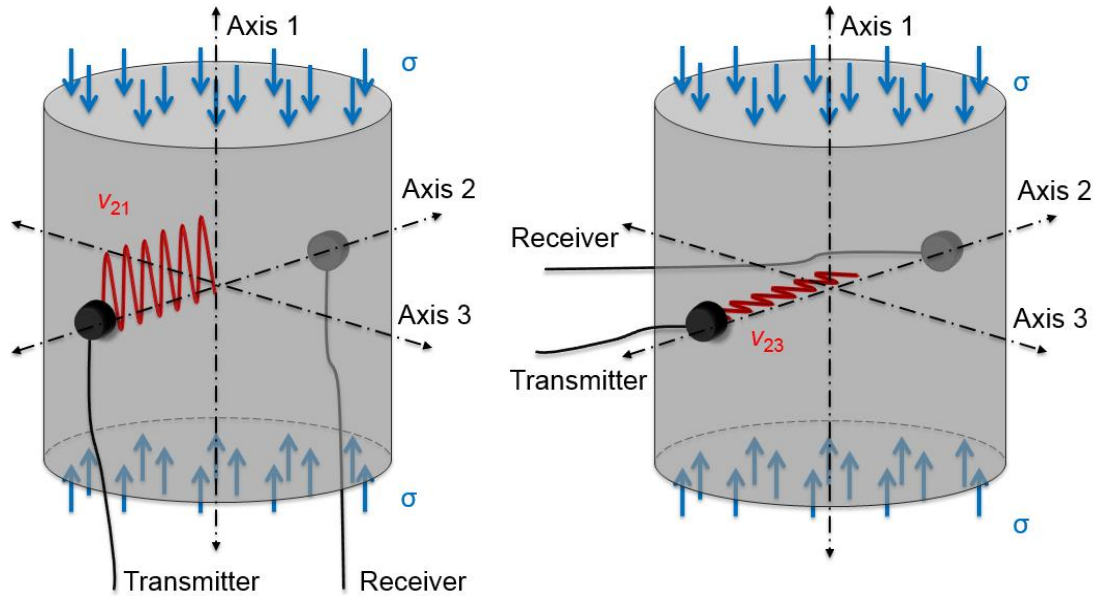


Figure 9: Diagram of ultrasonic transducers attached to concrete, oriented (left) parallel to applied stress and (right) perpendicular to applied stress, shear waves polarized along Axis 2, in directions 1 and 3

After the initial reference measurement was recorded, the compression machine was used to apply an increasing uniaxial load onto the specimen along Axis 1 in approximately 20 kN (5 kip) increments. At each step, this load was maintained at the specified level and the transducers are applied again to take a set of measurements. This was continued until the specimen reached its ultimate strength and failed. For each load step, the input and received signals were both recorded and then analyzed and visualized using MATLAB, Microsoft Excel, and OriginPro.

The experimental setup for the first test is shown in Figure 10 and the following test with Block 1 is shown in Figure 11. Aside from the dimensions of the specimens, the primary difference between each scenario is the loading protocol.



Figure 10: (left) Concrete cylinder setup and (right) same cylinder at failure



Figure 11: (left) concrete block with shear transducers and (right) compression machine and data acquisition system, DAQ

The Cylinder 1 test was first performed to establish some baseline information and to test the feasibility of our approach. The data from both the sender and receiver were recorded through the data acquisition system (DAQ) and onto the computer. Afterward, the transducers were detached and the compression machine used to apply a uniaxial load onto the specimen in 5 kip increments. At each step, this load was maintained at the specified level and the transducers were applied again to take another set of readings. This was continued until the specimen exceeded its ultimate strength and failed. Two additional concrete specimens were loaded to failure, confirming similar physical properties and failure characteristics. Following this, the next experiment with Cylinder 2 was performed to corroborate the initial findings, establishing a correlation between the applied stress and the velocity of the ultrasonic shear wave.

To expand on the initial findings, the next step was to look at how the shear waves behaved in concrete of different geometry. Adding an extra level of complexity, we also took additional measurements as we performed cyclical loading on concrete Blocks 1 and 2 (of different dimensions), detailed in the following section.

2.4.3 Finding the Optimal Frequency

The first experiment, Cylinder 1, was performed to establish a reference point for the remainder of our work. After choosing a suitable input waveform, it was important to find the frequency that provides the clearest data. Since we know that frequencies between 25 – 100 kHz are typical for testing concrete [1], this is the first

parameter that was analyzed. The four cases: 25, 50, 75 and 100 KHz, cover a significant spectrum and produce varying results. The key was to determine the frequency at which we have the clearest signal that also showed sensitivity under applied stress. Through this process, we determined that 50 kHz was generally a good compromise between sensitivity and amplitude strength.

2.4.4 Effects of Cyclic Loading

After establishing the baseline information, another parameter that was analyzed in this study was the effect of cyclic loading. This process can theoretically indicate whether there is any variation in the readings as a result of internal changes in the concrete and consequently induced damage. To test this, the compressive loading was performed in discrete loading cycles. This portion of the study was performed in two experiments, using two concrete blocks of varying heights (Blocks 1 and 2). During both experiments, elastomeric pads were placed above and below the concrete block to balance the distribution of stress (Figure 12). The bottom of the compression machine was a stationary platform, while the top steadily lowered, uniaxially compressing the concrete specimen.



Figure 12: Concrete block specimen in compression machine with bearing pads on the top and bottom

Unlike the previous tests, these specimens were not loaded continuously to failure. Instead, each underwent a series of loading and unloading cycles. During the Block 1 experiment, data was collected in sets, as shown below in Figure 13. Although the load was still increased in increments of 5 kips, the maximum load limit increased for each cycle was incremented by 25 kips each time. After each loading cycle was complete, the block was unloaded to 5 kips and the process was repeated.

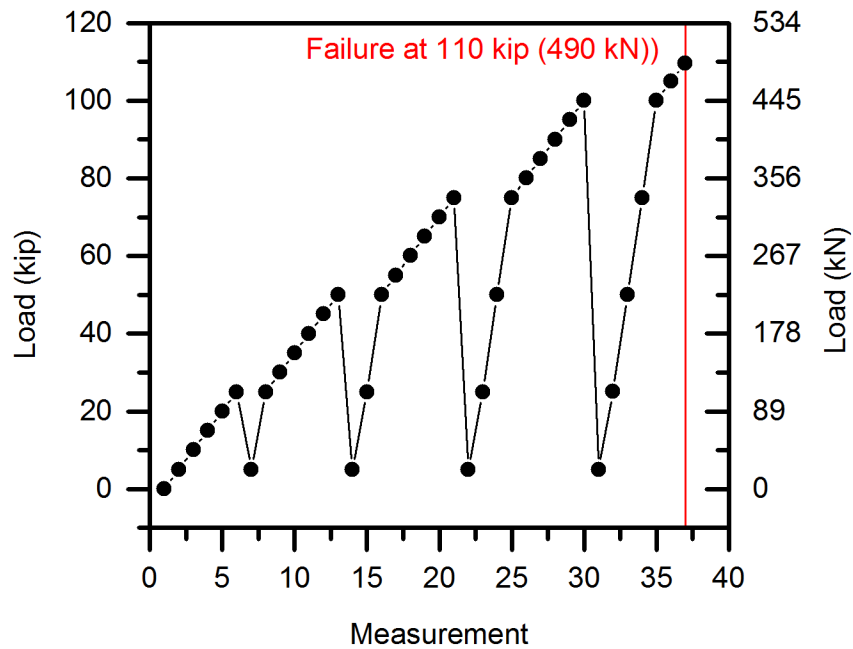


Figure 13: Loading and unloading cycles for Block 1, specimen failing at 110 kips load

For example, the first set of data recorded from 22 kN to 111 kN (5 to 25 kips)—five sets of data total. After this, the specimen was unloaded back to 22 kN (5 kips) and the next set of data was collected such that readings are taken at 22, 111, 133, 156 kN (5, 25, 30, 35 kips) and continued to 222 kN (50 kips). This unloading and reloading procedure was repeated until the concrete reached ultimate strength and failed (Figure 14).



Figure 14: Concrete block 1 failure: (left) side view and (right) top view

In the Block 2 test, the loading protocol was adjusted such that after each loading cycle, the load was not directly released back to 22 kN (5 kips). Instead, it is similarly unloaded in 22 kN (5 kip) increments. In this fashion, again this specimen was loaded to failure, which happened at a similar load, as expected. In this case though, many more measurements were taken, thus allowing for more cases to compare in the analysis. The following analysis in Section 2.5 includes data grouped by the loading/unloading cycle and that of the measurements taken at the same load across the different cycles.

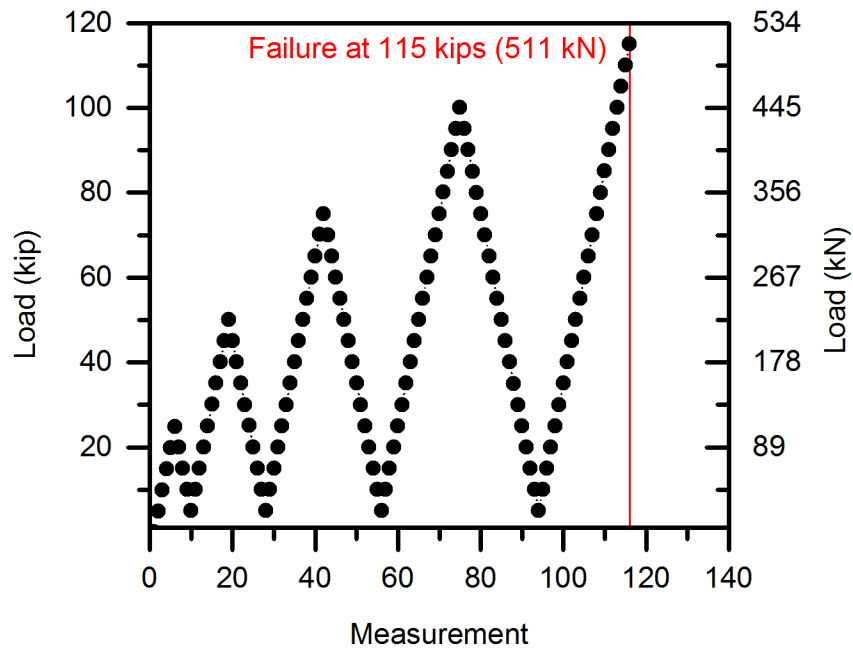


Figure 15: Loading and unloading cycles for Block 2, specimen failing at 115 kip load

This is an opportune moment to clarify the significance of the measurements we were taking at each load. At each level of applied stress σ , measurements were taken with shear waves traveling through the width of the concrete in the two polarization directions. After all the data was collected, it was analyzed to examine whether it uncovered any information relevant to the expected change in ultrasonic velocity due to the acoustoelastic effect.

2.5 Data Processing and Analysis

2.5.1 Frequency

The first test conducted in this study was on Cylinder 1, in order to determine the basics necessary to establish a method for estimating in-situ stress in concrete. The main focus of this test was to compare the use of different frequencies for the ultrasonic pulse and determine which worked best. The following compares shear waves induced about four different center frequencies: 25, 50, 75 and 100 kHz. In Figure 16, the data collected in an unloaded specimen is shown together, with the input wave depicted in green and the received wave in blue.

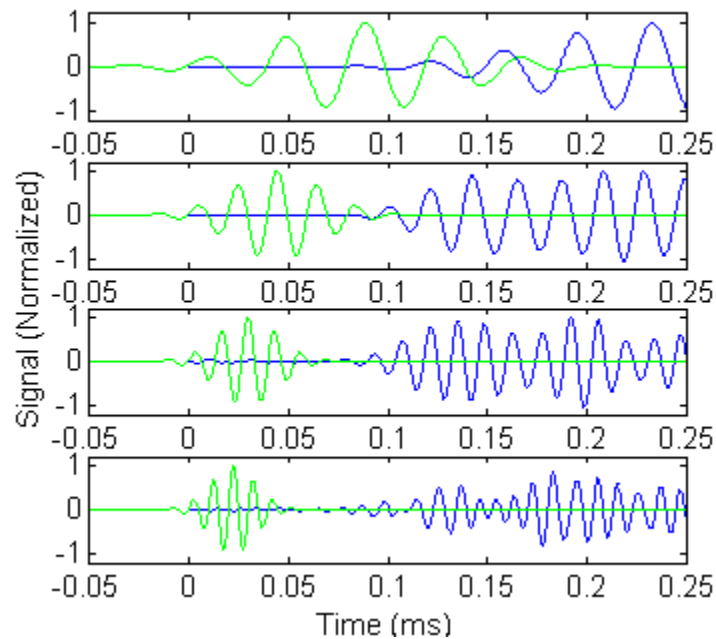


Figure 16: Transmitted excitation and received signals (normalized) at 25, 50, 75 and 100 KHz (top to bottom)

Looking at the behavior of the concrete at the different frequencies visually shows that for 25 and 50 kHz, the input signal was still entering the concrete even when the first part of it was already detected at the receiving transducer. It is also apparent that the nature of the received signal is different, as a result of the elastic wave's sensitivity to the aggregates and other inclusions in the concrete.

As already shown earlier in Figure 21, there are different degrees of noise in each of these received signals. In order to calculate the time it took for the wave to travel through the specimen, it was critical to identify when the signal was first received. With 75 kHz frequency and above, this proves unnecessarily challenging, likely as a result of the heterogeneities interfering with the shorter wavelengths. In the higher ranges, the wavelength becomes smaller and more comparable to the size of heterogeneities in the concrete, thus resulting in greater multiple scattering [28]. If we were presented this data to calculate the *time of flight (TOF)*, there are methods to achieve this even with lower signal-to-noise ratios.

What about 25 kHz at the low end of the spectrum? Let us plot the results of the initial Cylinder 1 test in Figure 17. The black squares represent the change in the *TOF* of the wave polarized in the direction parallel to the load (21) and the red dots represent the direction perpendicular to the load (23). These are plotted versus the stress ratio—the applied stress as a fraction of the ultimate strength, f_c . The shaded lines between data points the standard error between the three measurements taken for each stress level. Due to the minimal variance between each measurement, standard error bars would interfere with the data points and thus were not used.

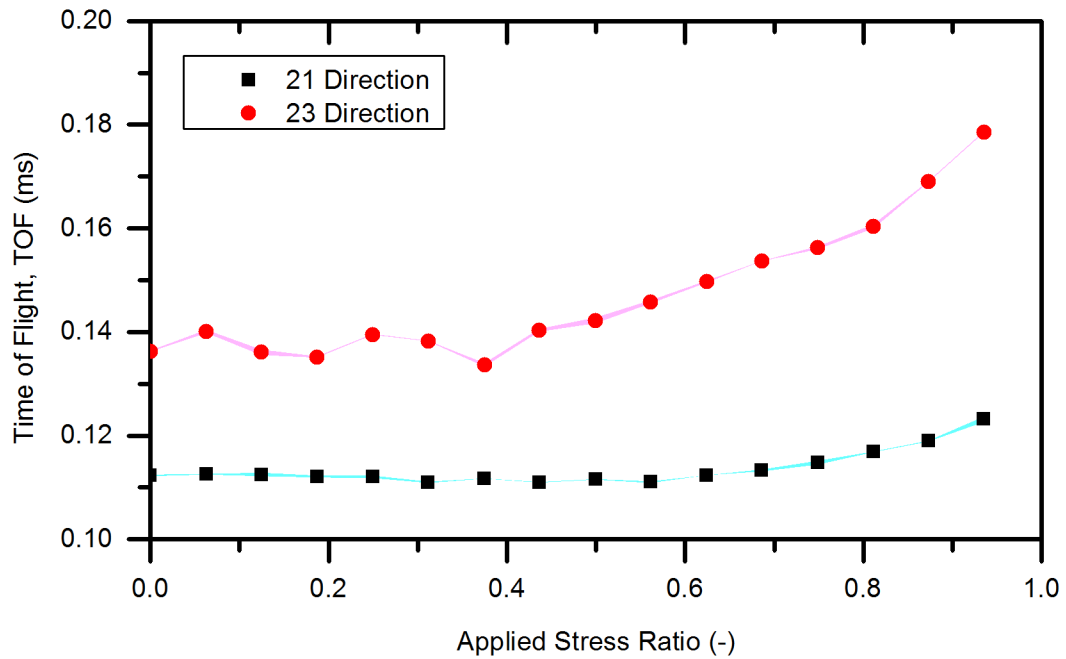


Figure 17: Cylinder 1 shear wave readings at 25 KHz, not aligned at same origin

Although there is clearly a correlation between the increasing stress in the concrete and the resulting *TOF* recorded, this frequency betrays a lack of sensitivity to the underlying acoustoelasticity that we seek to measure. To begin, there is significant oscillation in the readings for the 23 direction, transverse to the applied stress up to approximately 40% of applied ultimate stress. Furthermore, the *TOF* and thus the velocity of the waves are significantly different starting from time zero. This is unexpected because the ultrasonic vibrations sent into the concrete are travelling along an identical travel path. Thus, the *TOF* at time zero should be essentially identical. In fact, this is what we find for the data sets of the other tested frequencies.

We will return to the following plot in Section 2.6.1 where we explain the details in depth. For now, our focus is understanding that this serves as a qualitative comparison between the different frequencies. Ultimately, this research is based around a method for calculating the *TOF ratio*, B , which is a single parameter dependent on the *TOF* of each of the measurements in the two independent directions. For the 25 kHz example, the two lines in Figure 17 are combined the form top line in Figure 18.

To conclude and all things considered, 50 kHz is a fair compromise between the high signal-to-noise ratio achieved by the 25 kHz and the sensitivity to change in applied stress at the 75 KHz and above. It can also be observed that there is a clear trend in B as a function of the applied stress with little data variation.

The results for the 100 kHz data set was not included. This is because it was not possible to identify the necessary features to calculate the elapsed time between the input and received signals (*TOF*) itself using the method explained in Section 2.5.3; the signal could not be clearly distinguished from the noise. Although the plots shown in this section are post-filtering, the process of noise filtering itself deserves an explanation. The analysis cannot proceed before this is accomplished.

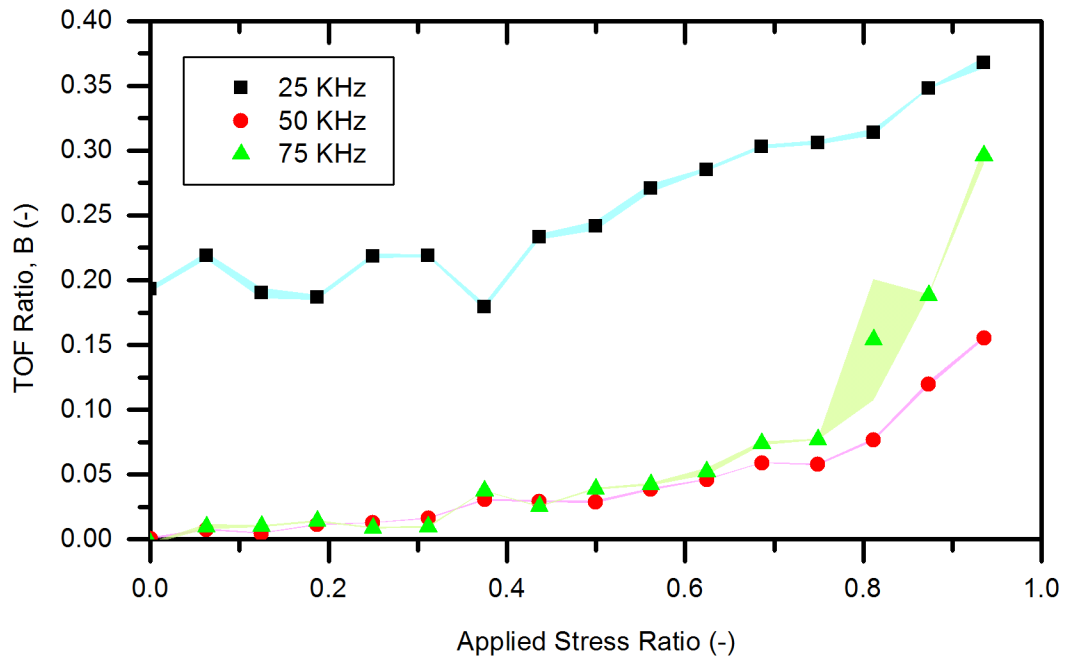


Figure 18: Cylinder 1, *time of flight* ratio increasing as function of applied stress

2.5.2 Filtering

Before the data can be interpreted, the presence of noise needs to be addressed. Although the input signal was detected clearly, the received signals contained additional noise that clouded the useful information. Noise is the random undesired data that is introduced during the recording process. Removing as much of this as possible through a filter eliminates extraneous data that corrupts the true signal, effectively smoothing the data. By reducing the degree of noise apparent in the data, we increased the signal-to-noise ratio and consequently made it easier to calculate *TOF*. It should be recognized that a trade-off exists when filtering out noise, i.e. if the filters are set too aggressively, actual signal content may be lost as well. Following are the steps that were taken to consider that.

By performing a fast Fourier transform (FFT) on the data sets, the frequency content of the signals can be extracted and used. A look at the FFTs of a pair of transmitted and received signals showed a clear difference in the frequency spectrum. For the example shown in Figure 19, the shear wave transmitted into the concrete is clearly centered on 50 kHz in the form of a Gaussian shape which is expected from a Morlet-type pulse.

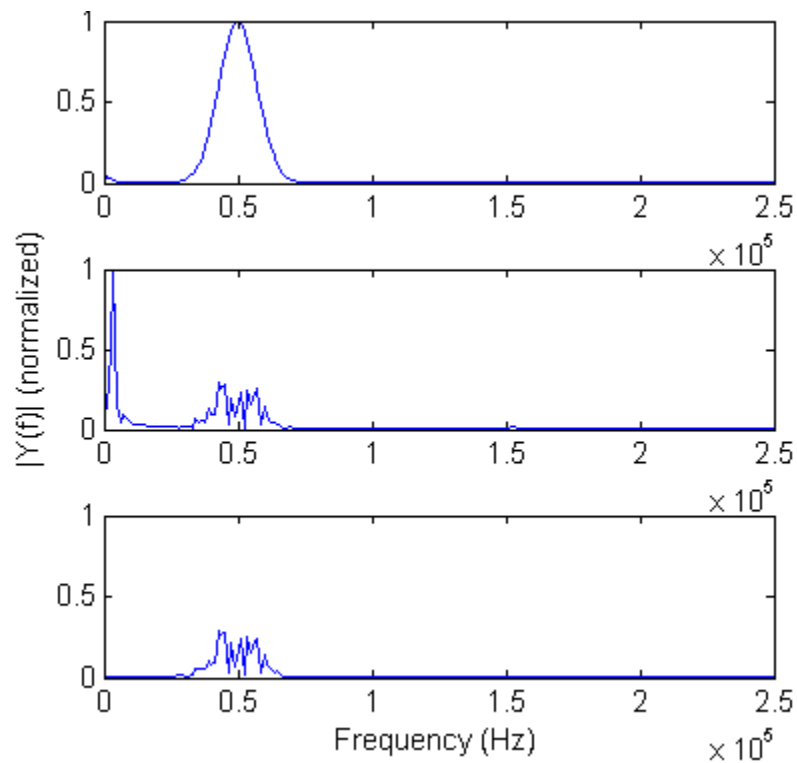


Figure 19: FFT of (top) input wave with center frequency of 50 kHz, (mid) unfiltered received signal and (bottom) received signal with applied bandpass filter

However, this signal changed as it propagated through the solid medium. The frequency of the received signal was affected by wave dispersion and attenuation (explained in Section 1.4). Consequently, the shape of the pulse was distorted. Instead of a clear maximum amplitude occurring at the center frequency, the information of interest around 50 kHz was superimposed by additional low frequency content.

Since the characteristics of our transmitted wave are known, it follows that any recorded information far below the intended frequency was not of interest. Furthermore, this can complicate the analysis. This additional noise in the frequency spectrum correlates with additional low-frequency vibrations added to the true signal in the time domain. Without noise, it is expected that in an unloaded state, the receiver would record 0 V for the entire period it is recording. In Figure 20, the top is the original recorded signal shown in contrast to the filtered version below it.

By applying a bandpass filter with frequencies between 25 and 75 kHz, we effectively removed low-frequency vibrations and high-frequency noise and increased the signal-to-noise ratio. Even so, there is more to consider. In this example, we looked at only one possibly frequency at which the elastic shear wave can be transmitted. Instead of 50 kHz, it could anything else within reason – such as 100 kHz. Even after employing the bandpass filtering technique, there can still be significant noise present in the signal. Looking at just the earlier portion of the received signal at 50 kHz and 100 kHz, there were clearly two different results. Although a quick calculation showed that the sent signal should not be detected at the receiver until after 0.05 ms, there were clearly oscillations in the 100 kHz data. Note that the amplitudes

of the signals shown in Figure 18 have been normalized. In reality the 100 kHz waveform would have a much lower amplitude and thus lower signal-to-noise ratio.

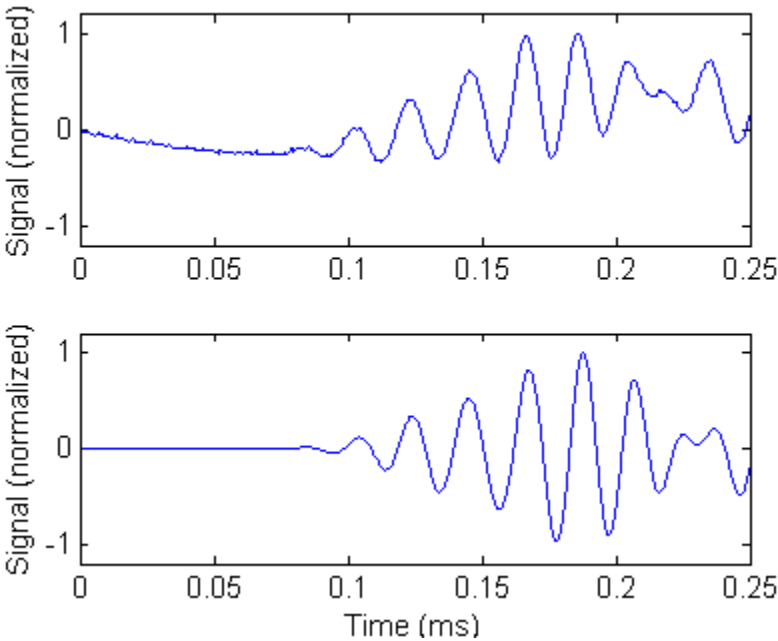


Figure 20: (top) unfiltered received signal at unloaded state and (bottom) signal with applied bandpass filter

This difference stems from the very nature of the medium carrying the ultrasonic wave. Concrete is a complex material, consisting of graded aggregates distributed throughout the material in an inexact way, bound in a cement matrix. Thus, it exhibits heterogeneous structure with local variations in material property. As a result, a signal with wavelengths smaller or equal the nominal aggregate size will be highly scattered and attenuated [1]. What this means is that through Equation (1), which was

introduced in Section 1.4, we know that to maintain a larger wavelength, we needed to use lower frequencies (particularly compared to steel).

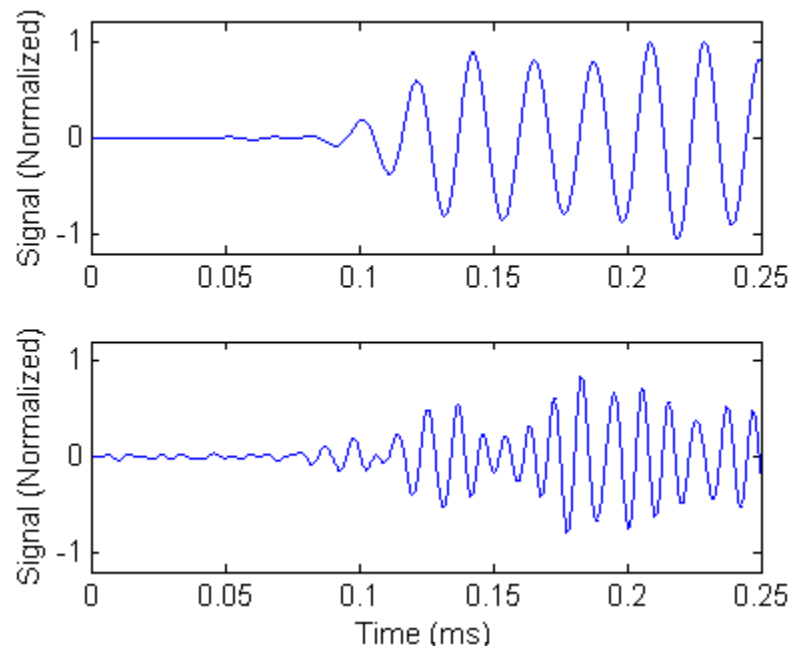


Figure 21: Comparison of received signal from transmitted waveform at (top) 50 kHz and (bottom) 100 kHz frequency, all else the same

To further complicate the situation, most structural concrete also contains reinforcing steel. This would clearly affect the measured wave velocity. However, since the goal of this study is to establish basic research for acoustoelasticity in concrete, this factor is currently ignored. Unfortunately it is not possible to do that for cracks, voids and other internal discontinuities that will inherently be present in the material. In general, studies have shown that only relatively large discontinuities will

significantly reduce the measured velocity [1]. Nevertheless, identifying an appropriate frequency helps to reduce the impact of internal discontinuities on our data. This leads to the next topic in our consideration of acoustoelasticity.

2.5.3 Time of Flight

After a frequency was chosen (50 kHz) and the signal filtered (bandpass filter between 25 and 75 kHz), the transmitted and received signals can be compared in detail to determine the effect of acoustoelasticity. To do this, first the *TOF* (= time of flight) of the ultrasonic shear waves was calculated.

An example of the data is shown in Figure 22, where the signal amplitude was normalized for ease of analysis. As explained in Section 1.4, when a stress wave travels through the concrete, the waveform is not the same when it is received. Furthermore, the receiver will not only record the direct wave from the transmitter, but because the input pulse radiates isotropically from the source, the received signal also includes energy from reflections off of the cylinder boundaries.

As explained in Section 2.4.2, the ultrasonic stress wave radiates in every direction outward from the origin of the transducer into the concrete. Thus, there are different paths that the input wave can take to reach the receiver. In fact, there are waves traveling throughout the entire volume of the specimen after some time has passed. As they propagate, they scatter and reflect at the boundaries at different angles and continue to dissipate energy.

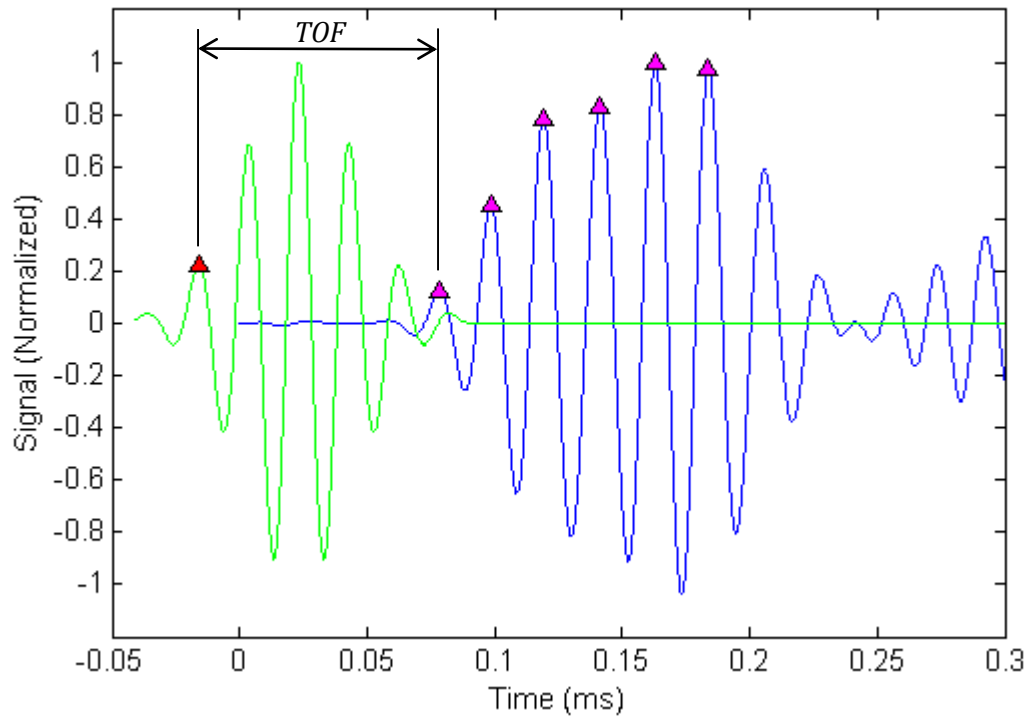


Figure 22: Example of normalized transmitted input signal (green, left) and received signal (blue, right) with the elapsed TOF labeled

A more thorough consideration of multiple-scattering is given in Section 3.2. That discussion focuses on the later portions of the signal, as scattering continues to propagate throughout the specimen. In contrast, the analysis in this chapter, focuses on the earliest portion of the signals. In the early portion, the signals are not yet affected by waves reflecting off the specimen boundaries.

In calculating the *TOF*, the absolute amplitude of the signal is not important. As long as the noise is adequately low that the signal is clearly defined, the amplitude is irrelevant. Of concern is the difference between the time at which the sent and received signals are detected. Although it is possible to use different parts of the

signals to calculate the *TOF*, such as the various positive peaks in the waveform, these results are based on the second positive peak. *TOF* is defined as the travel time of the wave between the transmitting and receiving transducers.

The *TOF* was calculated for each of the three measurements for each of the two polarized directions. Thus, for each load step there are a total of six measurements recorded. For each direction at each load/stress, there is an associated set of data that resembles the plot shown in Figure 22. The *TOFs* can then either be plotted with stress separately or combined. The primary concern was not the absolute values of the *TOFs*, as can be the case in conventional ultrasonic testing. Rather, the focus was on whether the relative change in the *TOF* can be manipulated to demonstrate a pattern.

To that end, we propose that the relative change in velocities be calculated by combining the pair of *TOFs* in both directions for each load step to represent a singular value as proposed by Nogues, et al. [48]. Thus, the normalized *time of flight* ratio, *B* is calculated as:

$$B = \frac{TOF_{23} - TOF_{21}}{\frac{1}{2}(TOF_{23} + TOF_{21})} \quad (8)$$

where TOF_{21} and TOF_{23} are the times of flight for the ultrasonic shear waves polarized in the parallel and perpendicular direction to the applied stress, respectively. This is essentially the difference between the *TOFs* normalized with the average *TOF* which

offers a consistent parameter eliminating the influence of transverse deformations due to the Poisson's effect.

To understand why we do all of this, we first look at a superposition of the two waves at 5 kips, recorded well within the elastic region (Figure 23). Visually they are very similar, particularly at the beginning of the waveform, when they both reach the receiver. This is expected since the travel path along Axis 2 is exactly the same distance for both waves. The variance was apparent after this initial point due to the differences in the geometry of the two polarized directions and thus the resulting dispersive energy arriving from reflections off the specimen boundary walls. Although the *TOF* in these two signals was essentially identical at a low stress, this changed at higher stresses due to the acoustoelastic effect introduced in Section 2.3.

As the applied stress on the concrete increased, the velocity of the wave polarized in the direction parallel to the load (v_{21}) was expected to increase. At two different stresses, we can see that although small in absolute terms, there was a difference in this response observable as illustrated in Figure 24. While these are visually similar waveforms, they are not identical. As stress increased, the same input waveform was detected at the receiver at different times. It is these small differences in velocity that could lead to a quantitative measure of the system. It should be noted though that since concrete is highly inhomogeneous, with its inclusion of cement, fine to coarse aggregates, and air bubbles, ultrasonic measurements have typically only been valid for forming qualitative conclusions [45].

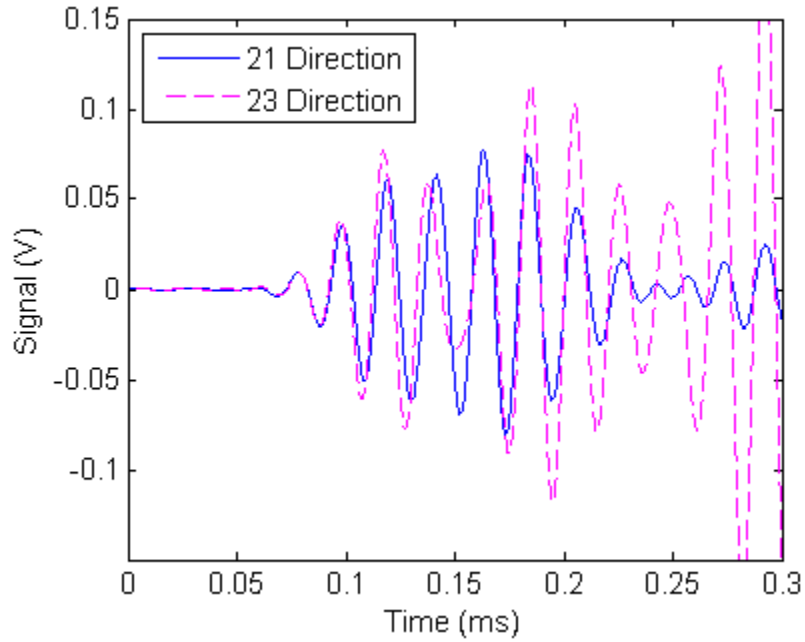


Figure 23: Received signals at 5 kip load for both polarized shear waves

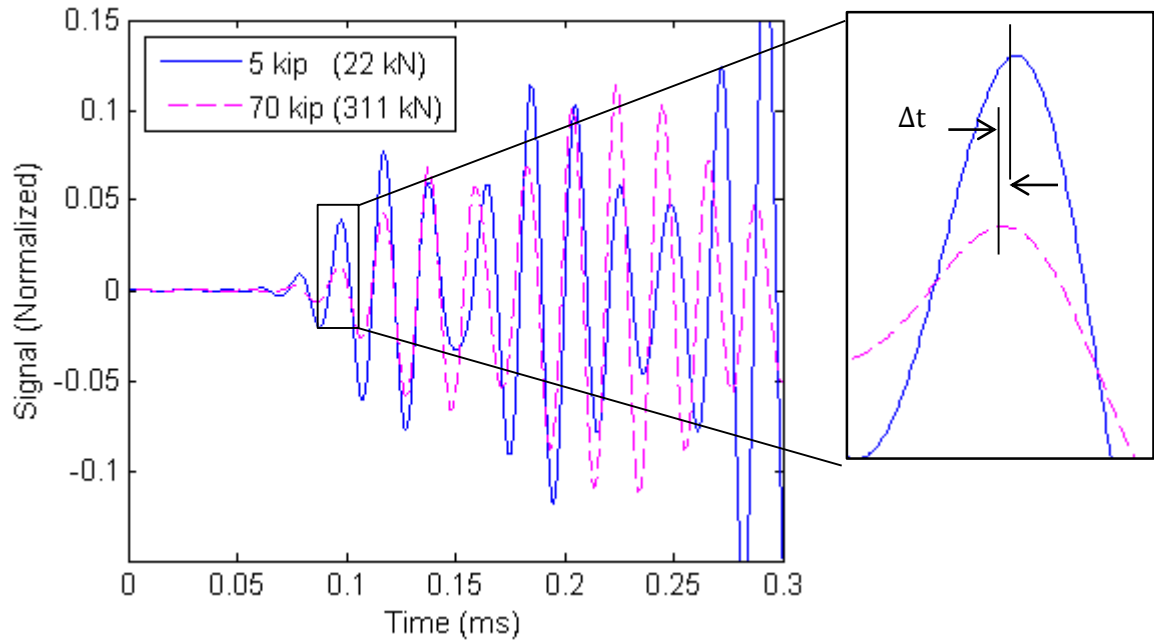


Figure 24: Difference between signals in transverse direction at different applied stresses, magnification showing change in the *time of flight*

To put this part of the overall experiment into context, each measurement taken for Cylinder 2 is shown in Figure 29. Indeed, as predicted, the *time of flight* in the parallel direction dropped, at least initially, and that of the perpendicular direction stayed relatively flat. Since the stress was acting uniaxially in only the Axis 1 direction, there is theoretically no impact on a wave polarized in the perpendicular direction. In practice, this supports Egle and Bray's findings with steel rail that the acoustoelastic effect is greater when the wave is polarized in the same direction as the load [18].

Of particular interest in our study are Equations (4) and (5), explained in Section 2.3.2. Although the following discussion does not explicitly use the equations, it is worth noting that the transverse waves, v_{21} and v_{23} would theoretically be equal in an unstressed state. As the stress increases though, v_{21} is expected to change, and that at a faster rate than v_{23} , which is consistent with the negative third-order constants discussed above.

This is also consistent with classic linear elastic theory. Since v_{21} is polarized in the same direction as the applied stress, it stands to reason that this wave will be affected by the magnitude of stress. Likewise, v_{23} has particle motion perpendicular to the applied stress. Thus, without accounting for acoustoelasticity, this wave would be independent of σ_{11} . As can be seen from the equations though, even in this direction, velocity is a function of stress. Assuming typical concrete properties, as stress increases, v_{21} and v_{23} both also increase. However, v_{21} (parallel to applied stress) is expected to increase more quickly.

Thus, while acoustoelastic theory can explain the change in wave velocity due to elastic deformation from applied stress, this does not fully explain the entire behavior from the unloaded state up to failure. Looking at the trends for each of these two sets of data, it is difficult to fit a meaningful trend that can be applied to other concrete members with different properties. Instead of considering these two sets of data separately, it is possible to combine them together into a singular plot, resulting in Figure 25 shown below.

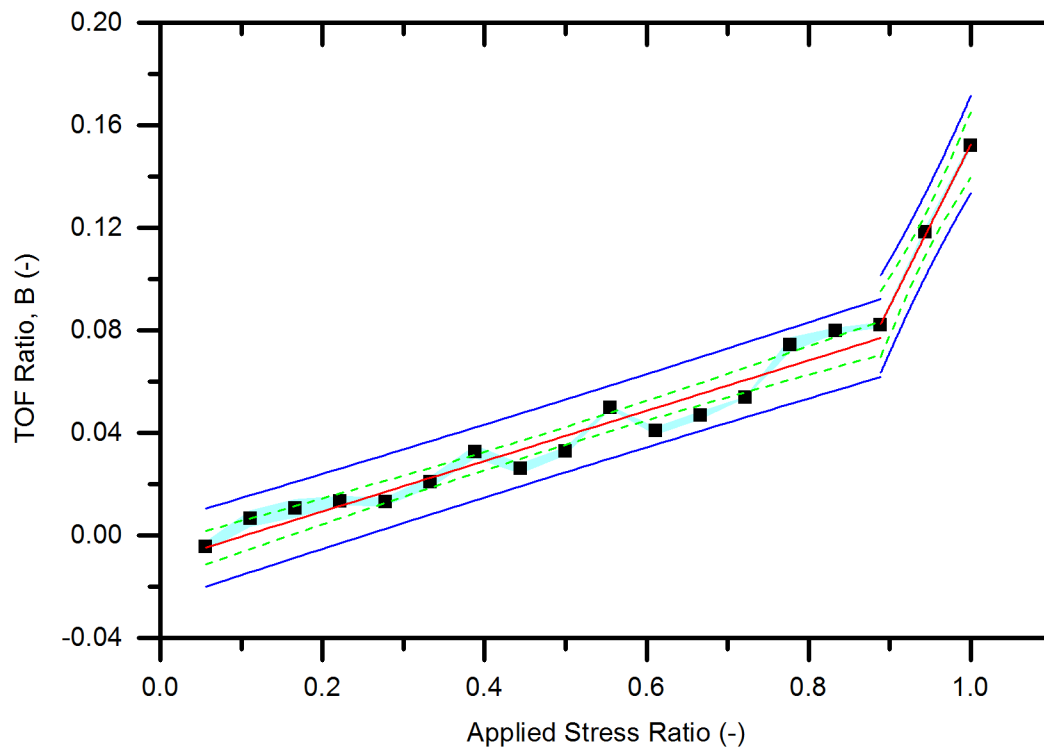


Figure 25: Combined *TOF ratios, B* using Equation (8)

As initially suggested earlier in Section 2.5.1, these two sets of data appear to fit well together. While providing illuminating insight into the behavior of concrete under uniaxial stress, the separate *TOF* data can also be combined into the *TOF ratio*, B using Equation (8). The result appears to be a bilinear trend between B and the stress ratio, shown in red (Figure 25). The discussion of these results are detailed in Section 2.6.

Next, recall that the *TOF* is calculated as the elapsed time between the second positive peak of the input signal and the positive peak of the corresponding received signal. This point of reference was not chosen arbitrarily, as shown in the next section.

2.5.4 Different Options in Computing Time of Flight

As mentioned earlier, the *time of flight (TOF)* is calculated as the difference between the time the second positive peak of the input is detected and the second positive peak of the output. However, there are other choices. The choice of using a local peak at all is to make it easier to quantifiably identify a reference point in the two signals. The analysis could also have been performed using the peaks occurring later in the signal.

Due to the dispersion and attenuation in the concrete, it follows that picking a reference point earlier in the signal would be logical. Aside from this consideration, it is possible to also directly compare the results using different peaks as the reference. To illustrate the differences, the *TOF* plots generated using the second and sixth peaks are shown in Figure 26, where it is clear that the data collected in the transverse

direction became random at higher stresses. As the concrete started to crack and deform, the cylinder expanded outward. Consequently, the later portions of the received signal became more unpredictable as the initial wave dispersed and reflected off the boundaries throughout the specimen.

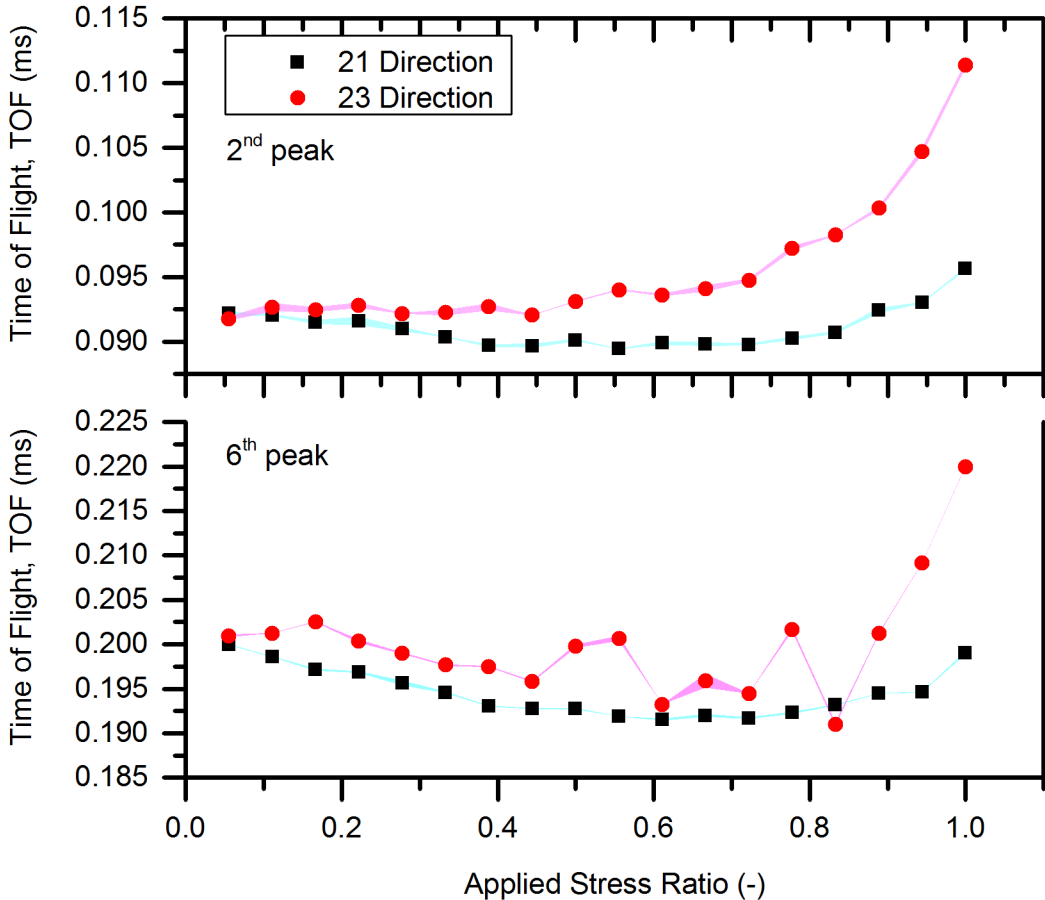


Figure 26: Cylinder 2 comparison of wave velocity calculated with input wave and chosen (top) second positive peak and (bottom) sixth peak of the received wave

In comparing the *TOF* data, choosing the second peak produced smoother curves. Taking this a step further, we can also look at the resulting *TOF ratios*. In this analysis of the values corresponding to Peaks 1 to 6, visually it already appears that Peak 2 achieves the best fit overall (Figure 27). Going a step further, this can be confirmed quantitatively.

Table 2 shows that the bilinear fit for Peak 2 indeed had the highest R^2 values, matching the lower residuals shown in Figure 28. Peak 1 is the closest to the beginning of the signals. In order to minimize the loss of ultrasound energy in the concrete, this is preferable to Peak 2. And the goodness of fit for the first two plots are comparable. A practical complication though is that the first positive peak in the chosen waveform has a considerably lower amplitude than the others, due to the characteristics of the Morlet waveform. As the initial excitation pulse travels from the sending transducer through the concrete, much of the energy is already dissipated by the time the receiver picks up the wave. As a result, even at 50 kHz with a relatively clean signal, it is more difficult to identify exactly where Peak 1 occurs on the received signal. In this experimental setup, it appeared that choosing Peak 2 produced more consistent results.

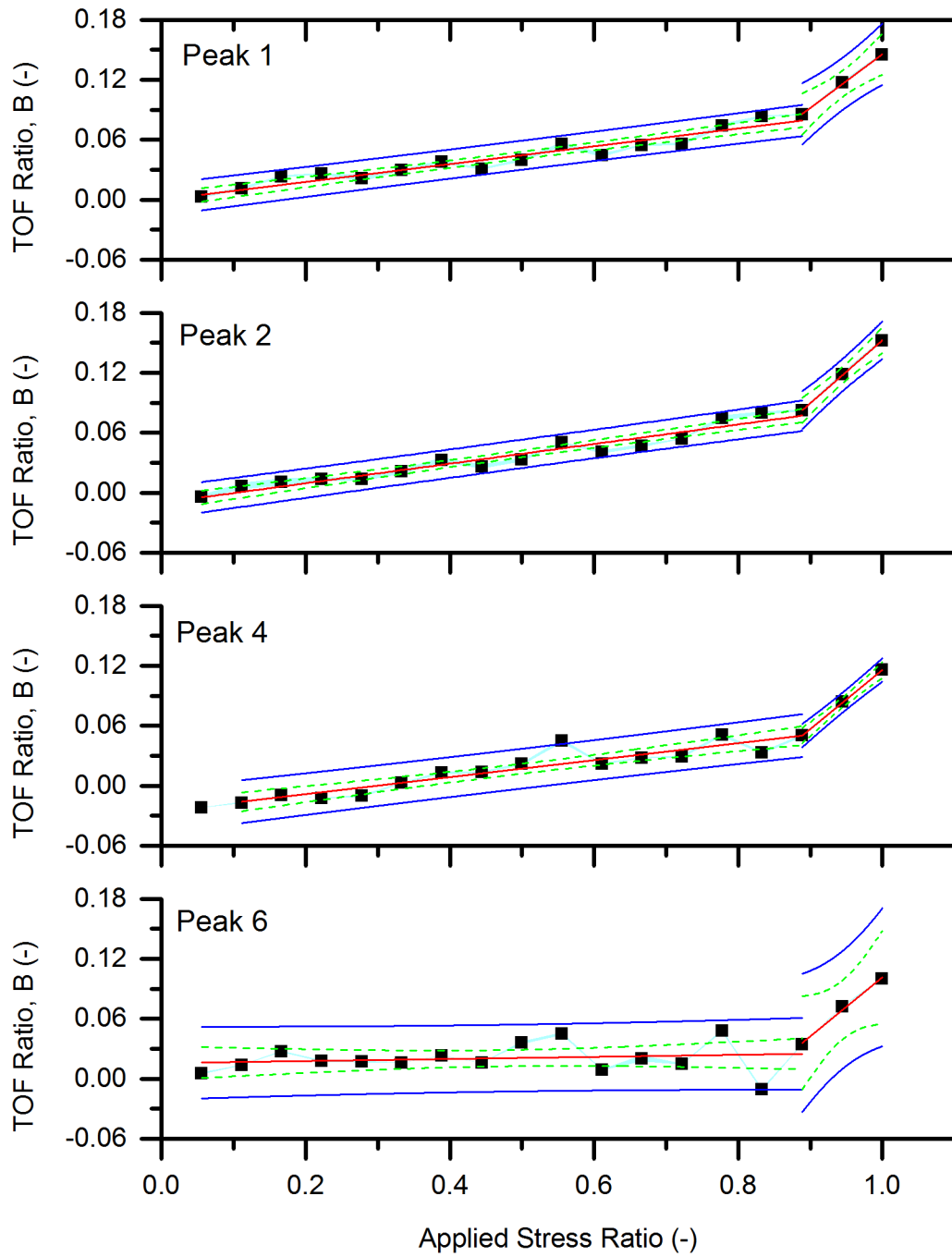


Figure 27: The *TOF* bilinear fit lines shown in with 95% confidence (green) and prediction (blue) limits for different peaks for Cylinder 2

Table 2: Numerical values of bilinear regression shown for Cylinder 2 for received signal's positive peaks

Peak	Adj. R ² 1	Slope 1	Adj. R ² 2	Slope 2
1	0.9274	2.803E-05	0.9964	1.691E-04
2	0.9727	1.967E-06	0.9998	1.980E-04
4	0.9262	2.671E-05	0.9989	1.859E-04
6	0.1850	3.267E-06	0.9963	1.858E-04

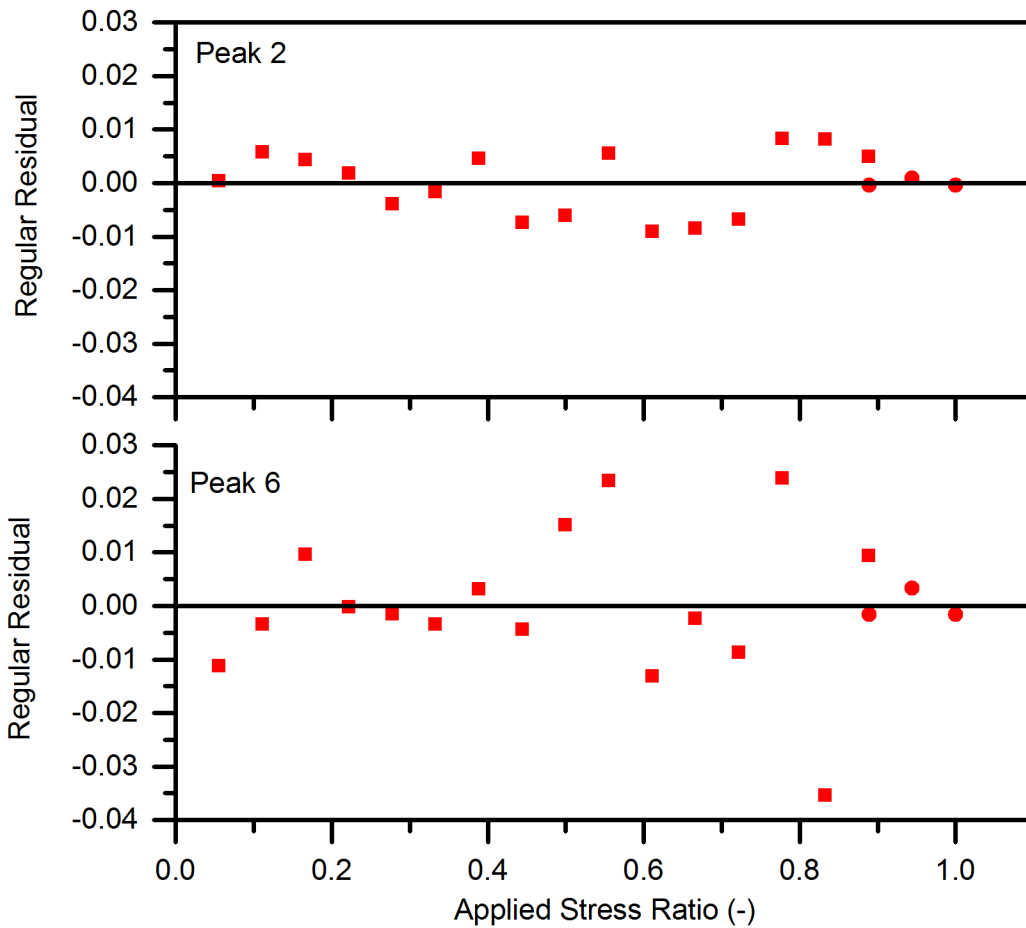


Figure 28: Comparison of residuals for bilinear regression of *time of flight* ratios for Cylinder 2

2.6 Results and Discussion

Following the discussion of the analysis procedures detailed in Section 2.5, this section aims to explain the purpose of each of the four performed experiments and discusses the significance of the results. Cylinders 1 and 2 were used to establish the principle of using the previously mentioned *TOF ratio* (Section 2.5.3) in order to form a relationship between ultrasonic wave velocity and applied stress, per acoustoelastic theory. A discussion of how this could ultimately be used to estimate in-situ stresses is explained in Section 2.6.1. Afterward, Blocks 1 and 2 were tested using similar procedures in order to analyze the effects of cyclical loading on this *TOF ratio* method. The results are examined in Section 2.6.2.

2.6.1 Advantage of Acoustoelasticity

First, the Cylinder 1 was performed to examine the effect of different frequencies on the recorded signal. In comparing 25, 50, 75 and 100 kHz pulses, in Section 2.5.1 we found that 50 kHz struck a good balance between the higher signal-to-noise ratio with lower frequencies and the sensitivity of higher frequencies. At this level, the transducers are able to detect subtle changes in the concrete from applied stress without excessive scattering due to the local heterogeneities in the cement matrix (i.e. aggregates and voids).

Using the 50 kHz wave, *time of flight (TOF)* measurements are recorded at incremental stress levels for two polarized directions: one in the direction parallel to the applied stress and one perpendicular. There is more than one way to identify the total elapsed time between when the pulse was initiated at the source and when it was

first detected at the receiver. As explained in Section 2.5.4, the local peaks in the input and output signals can be used to calculate this value; in the analysis, using the second positive peak appeared to generate results with the highest correlation and smallest residuals.

Next, we compared the plotted *TOF* values calculated for each of the polarized directions, separately (Figure 29). As expected, the *TOF* in the parallel (21) direction drops, at least initially, and that of the perpendicular direction stays relatively flat. The test specimens and procedure for Cylinders 1 and 2 are nearly identical. As a result of the initial findings in Cylinder 1, the next test with Cylinder 2 was performed to verify these results. Due primarily to the variations in material properties (specimens cast from different batches of concrete), the resulting values are not identical. However, the trends observed from both experiments were essentially the same.

Since the stress was acting uniaxially in only the Axis 1 direction, conceptually, the impact on a wave polarized in the perpendicular direction should be minimal. In practice, this supports Egle and Bray's findings with steel rail that the acoustoelastic effect is greater when the wave is polarized in the same direction as the applied stress [18]. This is also consistent with findings which demonstrate that concrete stays within the elastic region typically below 30% of its ultimate strength. Although micro-cracking is present in the concrete even before loading, its effect on elasticity is not detected through conventional methods until the stress level surpasses this point. After approximately 30%, concrete enters a quasi-brittle region, where bond cracks rapidly grow in size and quantity until they change the behavior of the concrete

(Section 2.3.5.2) [25]. For our concrete cylinder specimen, the theory of acoustoelasticity should hold at least up to this boundary between the elastic and quasi-brittle regions.

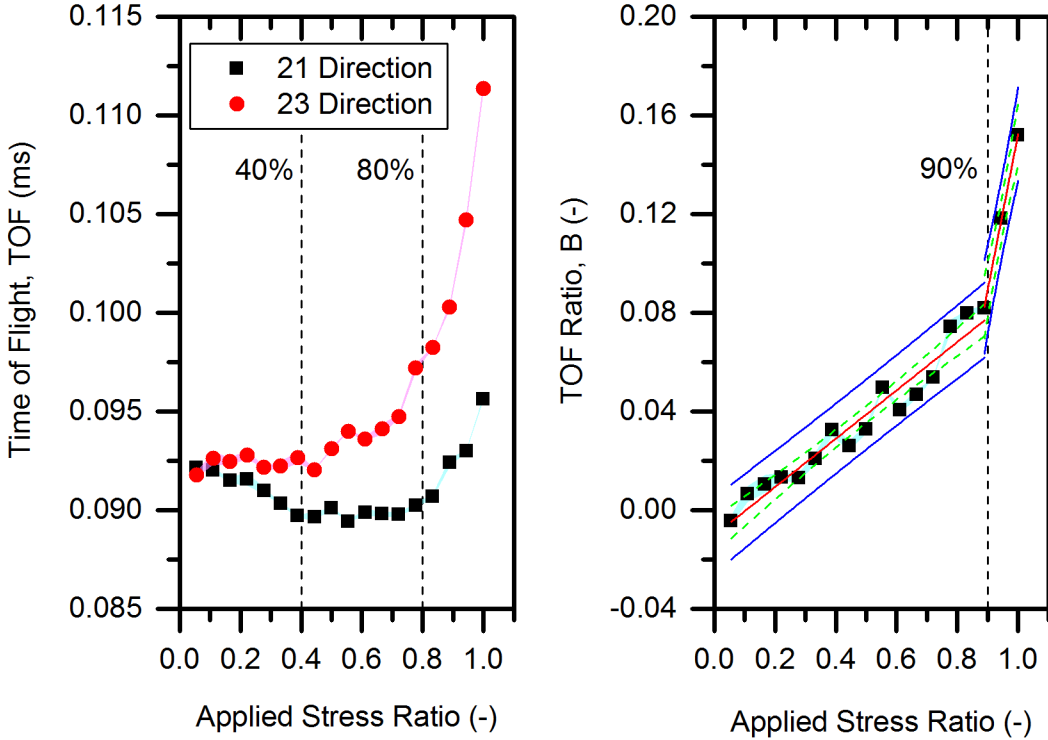


Figure 29: Calculated individual *TOFs* (left) and combined *TOF ratios, B* (right) with marked regions at percentage of ultimate strength for Cylinder 2

Our results show three distinct phases. The first phase shows a relatively constant TOF_{23} and a consistently decreasing TOF_{21} up to approximately 40% of ultimate strength which can be explained by theory. After that, in the second phase, TOF_{21} is fairly constant and TOF_{23} is steadily increasing up to approximately 80% of

ultimate strength. This can be explained by the formation and propagation of micro-cracking. In the final third phase both *TOF* values are increasing indicating a significant decrease in both shear wave velocities which can be explained by further micro-level cracking and initiation of macro-cracking. The results of our experiment indicate that the behavior of ultrasonic shear waves polarized through concrete do not strictly follow the theory of acoustoelasticity. The formation and propagation of cracks as the concrete is compressed seems to take over, thus highlighting that the assumption of a homogeneous and isotropic medium is not appropriate.

Since there is no consistent and unique trend of either one of the *TOF* curves they could not be reliably used as a prediction tool individually. Instead of looking at the separate *TOF* curves, now we look at the aforementioned *TOF ratio*, *B* defined by Equation (8). By combining these two curves, the result shows a clear and steadily increasing relationship (Figure 29). By applying a bi-linear curve-fit, the resulting squared correlation coefficients, R^2 , are 0.97 and 0.99 for the lower and upper stress portions of the fit, respectively. Also computed and shown are 95% confidence (full red line) and prediction (green dashed line) limits of the fits which indicate a surprisingly small data variance with a mean y-intercept close to zero. It can be observed that a clear change in the trend occurs at approximately 90% of the ultimate strength and this dramatic change in slope may potentially be useful to develop an indicator for impending failure. Towards the end of the test, although the *TOFs* of both polarized waves are increasing (and the velocities therefore decreasing), the *TOF* of the wave perpendicular to the stress increases more dramatically. One reason for

this may be that the concrete develops shear-type cracking aligned with Axis 1, which may interfere more strongly with the wave motion in this direction.

Although we currently have no quantifiable explanation for the sudden change in the *TOF ratio* curve towards the upper end of the specimen's strength, the data suggests a significant physical change in the material's structure that is most likely related to the formation of macro-cracks. This change is consistent with other research, such as that performed by Shokhouni et al., which reported macro-cracking developing after 80% of ultimate strength [38]. This also corresponds with the nonlinear behavior seen in a typical stress-strain curve, as mentioned earlier in Section 2.3.5.2.

The data suggests that the effect of applied stress on the concrete can be estimated – at least in part – through the use of acoustoelastic theory. Ultimately, when this method is applied to a structural member, *TOF ratios* would be calculated and plotted similarly to the ones shown in this chapter. Given that comparison measurements are established with comparable concrete properties, measurements could be taken in the field and the calculated *B* value could be used as the input to estimate in-situ stress.

2.6.2 Effects of Cyclic Loading

The experiments with Blocks 1 and 2 are significantly different from that of Cylinders 1 and 2. While the cylinders were loaded progressively from zero load to failure, the blocks were loaded cyclically—unloading and reloading to a higher stress

each time until failure. The specific loading protocols were outlined in Section 2.4.3.

Although the dimensions of the two blocks are different, the significance of the results for both are similar. Thus, the resulting data are considered together in this section.

The *TOF* plots of the 21 and 23 directions for Block 1 are shown in Figure 30. Each curve represents the different loading cycles that were shown in Figure 13. As a result, each curves consists of a different number of data points, ending at increasing stresses.

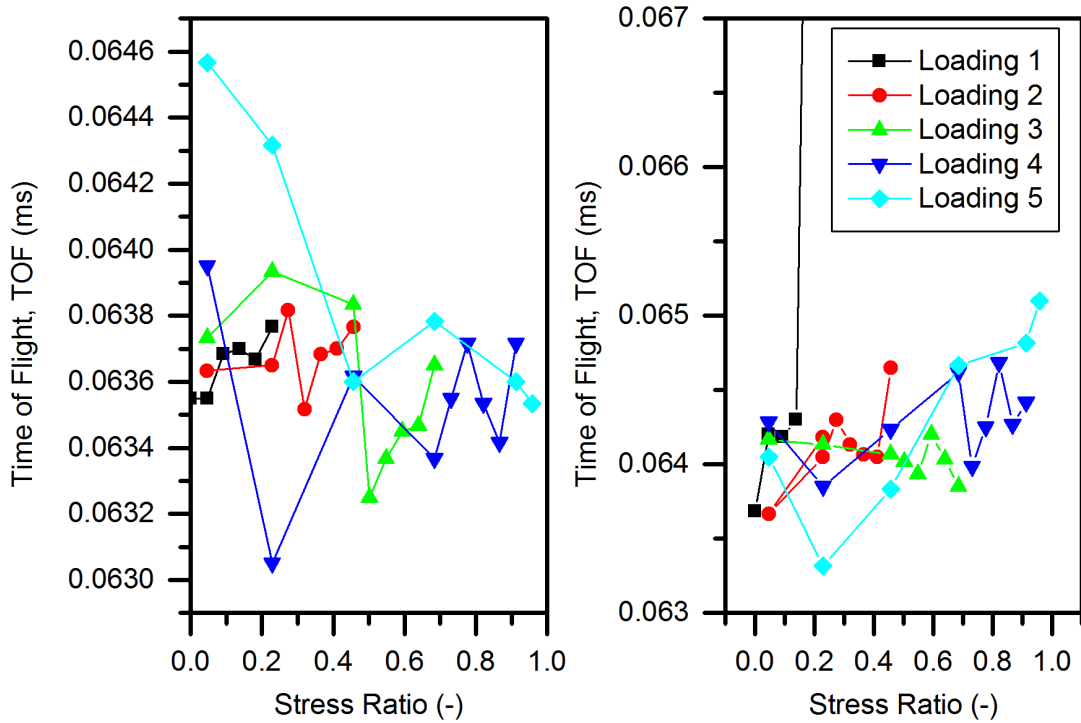


Figure 30: *TOF* of loading cycles for (left) 21 direction, parallel to stress and (right) 23 direction, perpendicular to stress for Block 1

While there is a general trend of the *TOF* decreasing in the parallel direction (left) and increasing in the perpendicular direction (right) similar to the trend seen in Cylinders 1 and 2, there is also a large amount of spread. Looking at just these plots, it

is difficult to see whether there is a consistent trend from one cycle to the next. According to the Kaiser effect, there should be no additional micro-cracking until the given stress exceeds any previously induced stresses on the specimen. Thus, the corresponding *TOF* curve for each cycle is expected to fall to only one consistent side of the previous cycle curves. However, this does not appear to be the case in the collected data. This is consistent with the difficulty in obtaining measurements in concrete, which consists of considerable local variations in the material. Consequently, if there is a method for extracting information regardless, this would be useful.

Instead of directly analyzing the *TOF*, we again look at the values of *B*, which are based on the individual *TOF* values of the two polarized directions. For Block 1, each of the five load sets are plotted together in Figure 31. Likewise, the same is done for Block 2 in Figure 32 with 5 “cycles” of increasing stress (loading) interwoven with 4 decreasing (unloading). Since there no measurements taken during the unloading process for the initial Block 1 test, each cycle is considered to begin at either a load of 0 or 34.5 MPa (5 kips) and ends at the specified upper range of the cycle before the specimen is unloaded for the next cycle.

To give a rough measure whether any of these sets of data follow any trend, linear regressions were fit to each. However, for clarity these were omitted in Figure 31 and shown in Figure 32. The corresponding adjusted R^2 values and slopes of the fitted lines for Block 2 are shown in Table 3. Evidently, the *B* values have a tendency to oscillate as the stress increases. Yet, there does appear to be a slight general increase in the *TOF ratio* values during the cyclical loading of Block 1. Although the

cleanest fit was found in the last loading cycle before failure, it is worth noting that this is also the only data set that includes negative B values. At most data points, the *time of flight* for the wave polarized in the perpendicular 23 direction was greater than the *TOF* in the parallel 21 direction. However, at the low stresses, the two swap places, such that the velocity in the perpendicular direction is greater. This is because as TOF_{21} is decreasing, TOF_{23} is increasing.

Table 3: Block 2 adjusted r-square values and slope of linear fit for each loading and unloading cycle

<i>Cycle</i>	Adj. R²	Slope
1	0.031	5.77E-06
2	0.488	3.79E-05
3	-0.114	-1.55E-06
4	-0.138	1.31E-06
5	0.395	4.97E-06
6	0.264	-6.13E-06
7	0.059	2.59E-06
8	0.139	-2.81E-06
9	0.578	5.18E-06

A similar trend also appears in the data of Block 2, which includes both loading and unloading cycles. The goodness of fit for each one varied, with R^2 values ranging from 0.07 to 0.9. The best fit was found in the last set of collected data before the concrete failed. The increase in B during loading is similar to that seen in Block 1, as expected; and B consequently generally decreases during the unloading. While we do not have the information to verify this, the reversed trend during the first two

unloading cycles and the second loading cycle could possibly be attributed to the consolidation of existing micro-cracks in the concrete (present before any loading occurred). This range corresponds to a maximum of 40% of the ultimate stress level.

As seen in the figures, there is significant scatter in the data points and they do not adhere strictly to a unifying equation. This indicates that there was an underlying change in the system as time elapses, from the beginning of the experiment until the concrete failure.

Moreover, there was an additional complication with the experiment. Block 1 failed at 21.0 MPa (3046 psi) and Block 2 at 22.8 MPa (3301 psi)—considerably lower than the estimated strength of the block: 26.1 MPa (3788 psi). During the Block 1 experiment, the elastomeric bearing pads were being visibly squeezed outward through the Poisson effect. With a lack of appropriate stiffness in the pads, they cannot be relied on to transfer the stresses from the compression machine directly in the vertical direction of loading. However, the results of Block 2 also exhibit a severe lack of precision.

The mode of failure for both experiments was similar and a picture of Block 1 is shown in Figure 14, where the concrete split exactly from the center, cracking through the full height in two planes. This could indicate that the bearing pad was also introducing a horizontal tensile stress across the cross-section of the concrete block. Thus, for more accurate results, the experiment could be rerun with stiffer pads.

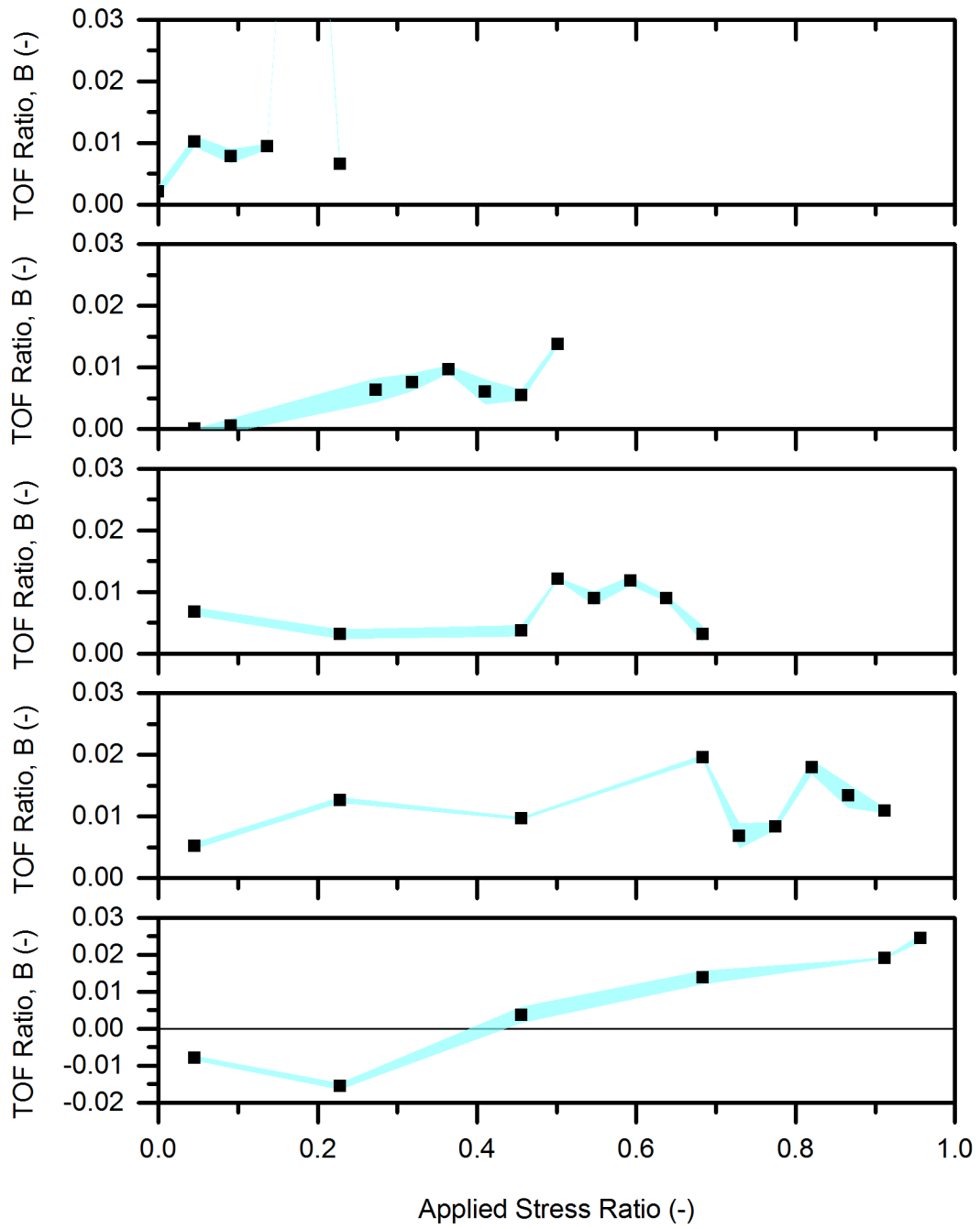


Figure 31: Block 1, *time of flight* ratios for each successive loading cycle until failure (five total)

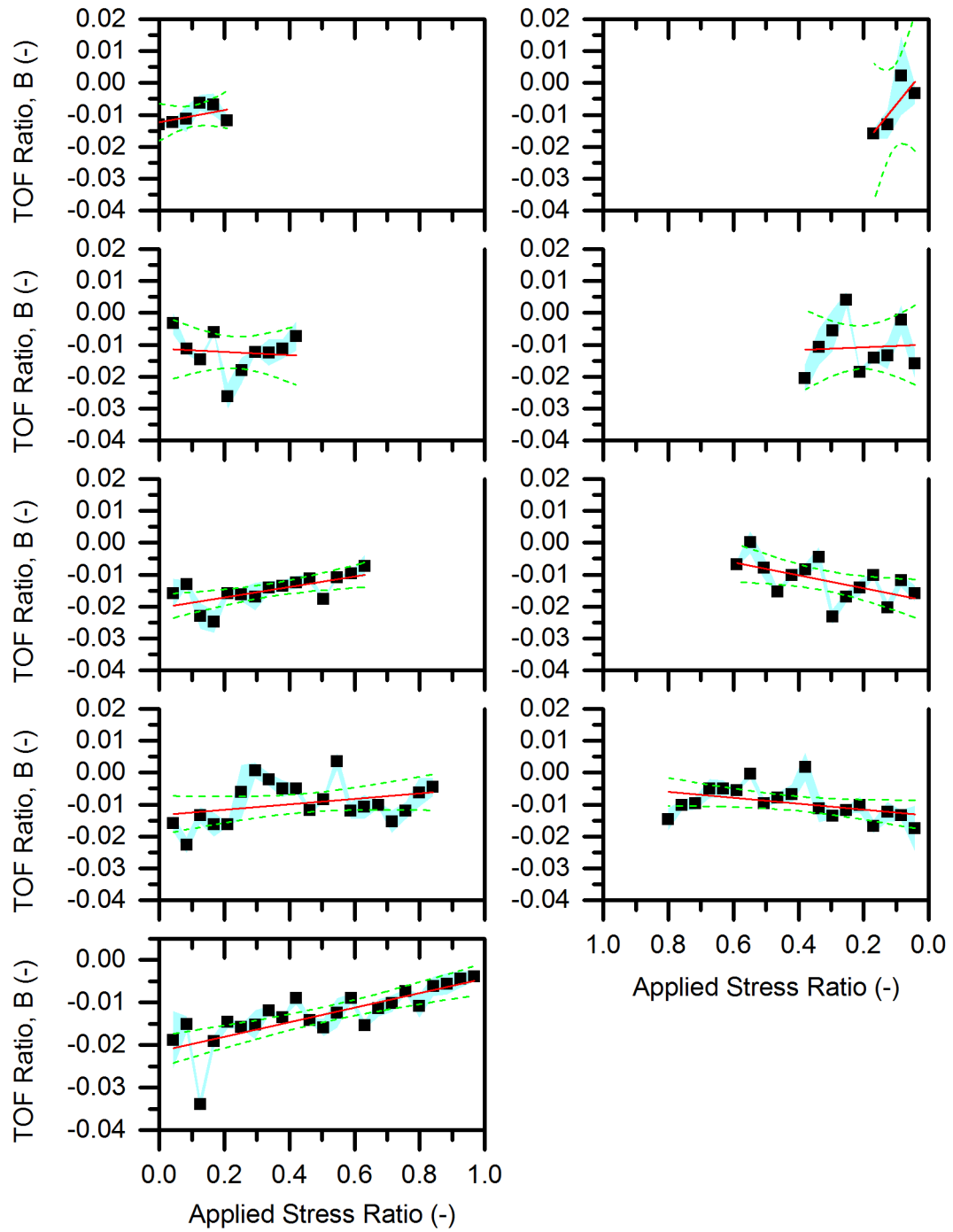


Figure 32: Block 2 successive (left) loading and (right) unloading cycles shown with *time of flight* ratios and fitted linear regression and corresponding 95% confidence intervals

Even using stiffer pads, the results of the following experiment for Block 2 produced a relatively high degree of scatter. One additional variable introduced to the experiment was the dependence of the results on the operator. Over the course of the experiment, there were three different operators that manually held the transducers against the concrete and rotated those 90° to the two different polarization orientations; the operator was consistent across any given loading cycle. As a result of this variability, it is evident in Figure 32 that certain loading cycle plots generally contain lower residuals and thus tighter fitting confidence intervals (green dashes).

It is clear that the results are not consistent between each loading and unloading stage. By examining the values collected for each data set, it is seen that the *time of flight* ratios were not always the same. To further analyze different results produced through a combination of micro-cracking and nonlinear behavior attributed to acoustoelasticity, the *TOF ratios* computed for the same load step were plotted together with the individual *TOF* curves (same values as in Figure 30). The results for the 22, 111 and 222 kN (5, 25 and 50 kips) in Block 1 are shown in Figure 33 with corresponding linear fit adj. R^2 and slope displayed in Table 4.

Table 4: Block 1 adjusted R-square values and slope of linear fit at shown loads

<i>Load (kN)</i>	<i>Load (kip)</i>	Adj. R^2	Slope
22	5	0.344	-0.0032
111	25	0.083	-0.0038
222	50	0.104	-0.0024

The value recorded for load cycle 1 is the first measurement at the load taken after starting the experiment and the value at load cycle 5 is the last one recorded before the concrete block failed. Although there were relatively few data points, each one shows a trend of decreasing B from the beginning to the end of the experiment. This suggests that the change in velocity is due not only due to the acoustoelastic effect but also a change in the structure of the concrete. More specifically, this is a sign that as the specimen is cyclically loaded, it sustains damage in the form of micro-cracking. It is expected that a given B value does not exceed the value of a previous loading cycling. Again, this is likely attributed to experimental and operator error.

For comparison, the B vs. loading cycle plots are also shown for Block 2 in Figure 34. The cycles shown include values that were recorded both during loading and unloading. Up to 89 kN (20 kips), which corresponds to approximately 15% of ultimate strength, there appear to be decreasing linear trends. After this point, the 20 and 40% (25 and 50 kips) curves start to flatten and possibly even reverse slope direction. In comparison, this trend is not apparent in Block 1. Note also though that the 21 direction wave path in Block 2 is also considerably greater than that in the Block 1. Therefore, a smaller slope to begin at lower stress levels is expected. Furthermore, since there was less scatter in the data, the Block 2 data may also be more sensitive to changes in the microstructure. As we know though from Section 2.3.5.2, bulk waves have been observed to exhibit changes in micro-cracking even at low stress levels (below 20%) [6].

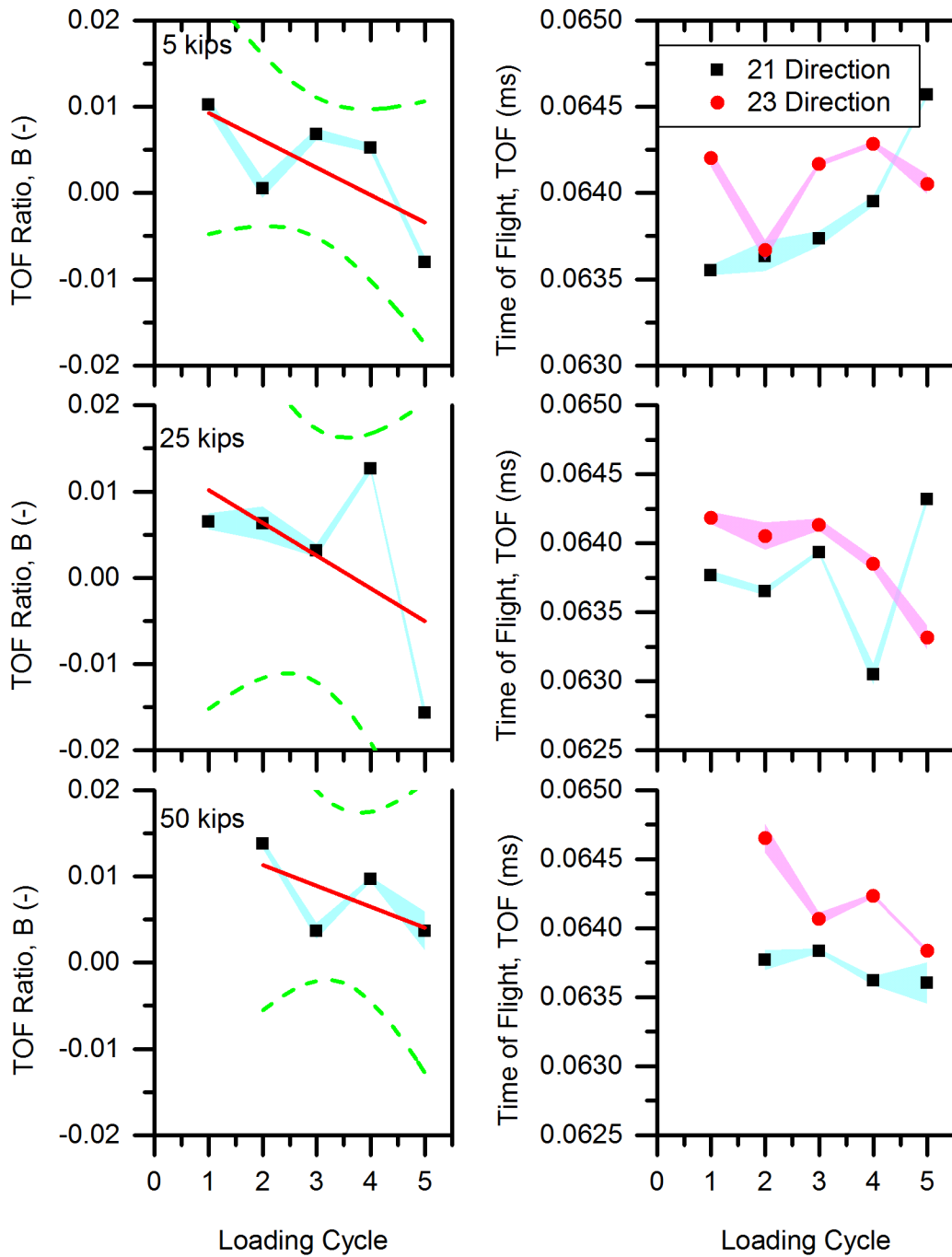


Figure 33: (left) Total *time of flight* ratios for each loading cycle at 5, 25 and 50 kips in the Block 1 experiment and (right) corresponding *time of flight* for the separate directions

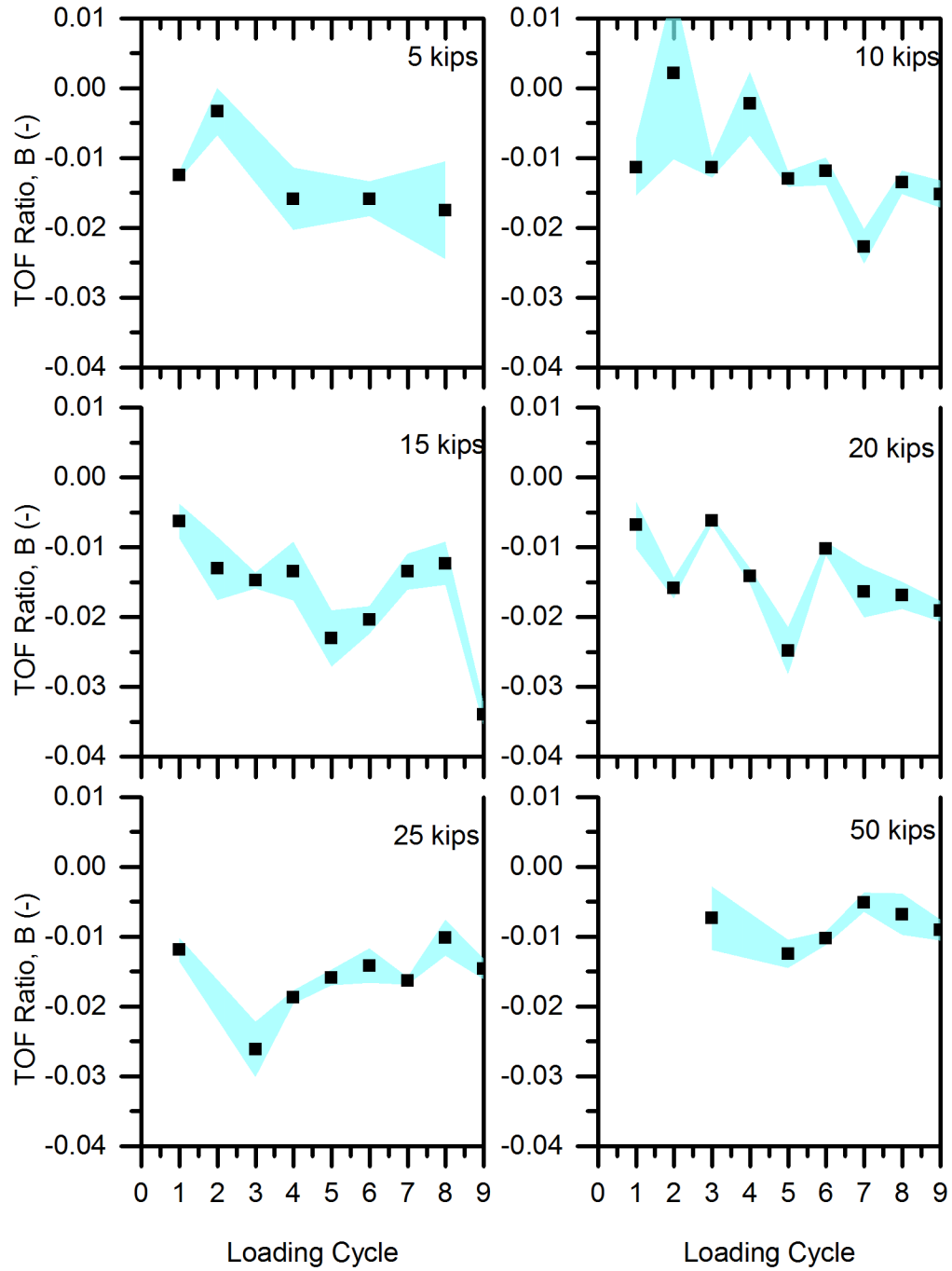


Figure 34: Block 2, *time of flight* ratios recorded for the same load over the course of several loading cycles

Overall, it is difficult to conclude by looking at only a plot of all the *TOF ratios* together as a function of stress that there is a clear trend from one cycle to the next. Certain sets follow a clearer line with less scatter, likely corresponding to differences in the operator. Separately though, the data appears to indicate that micro-cracking is occurring and that it may be possible to quantify using *TOF ratios B*.

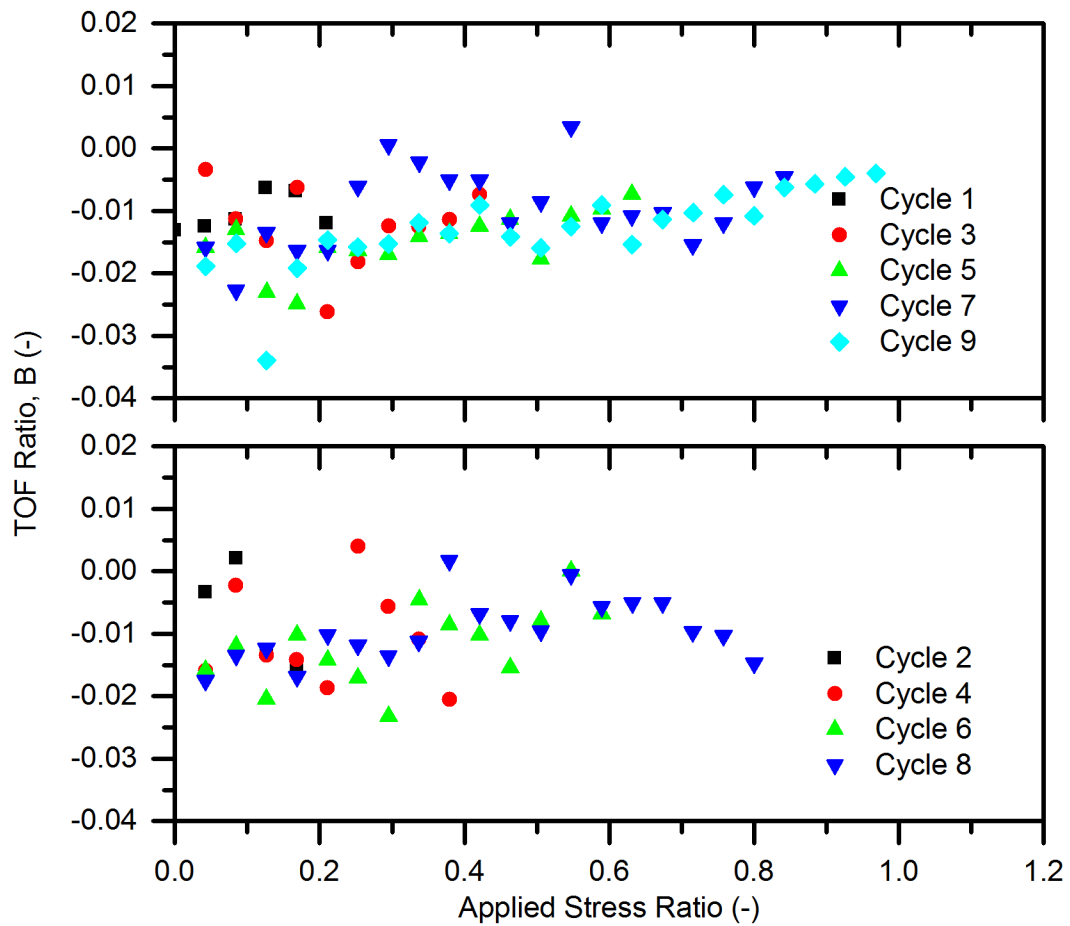


Figure 35: *Time of flight* ratios for each (top) loading cycle and (bottom) unloading cycle in Block 2

2.7 Conclusions and Future Work

Although the results of this preliminary experiment do not conclusively prove that they could lead to a method for estimating in-situ stresses in concrete, the correlation between applied stress and polarized ultrasonic shear wave velocities is promising. The data suggests that the effect of applied stress on the concrete can be explained – at least in part – through the use of acoustoelastic theory.

Yet, there remains the question of how to quantify these changes over the entire loading curve. Ultimately, a method that can be applied to an in-service structure must account for all of the factors that significantly impact ultrasonic wave propagation through concrete. These include considerations such as the aggregate content, concrete strength, and moisture content, among others. When this method is applied to a structural member, *TOF ratios* would be calculated and plotted similarly to the ones shown in Figure 25. After the measurements are taken in the field, the calculated *B* value would be used as the input to estimate the in-situ stress.

By combining the separate *TOF* measurements of the waves polarized parallel and perpendicular to the uniaxial stress, we are able to plot the combined *TOF ratios*. From the experiments on Cylinders 1 and 2, the trend is similar and shows the behavior of the concrete distinctly changing as the concrete is loaded to failure. The data also suggest that the nonlinear trend observed is in large part due to the effects of micro- and macro-cracking in the concrete. Consequently, the changes in *TOF* suggest that the trend may be broken down into at least three distinct regions. In an analysis of the *TOF* plots, acoustoelasticity primarily governs the behavior during lower stress,

within the elastic region approximately below 30-40% of ultimate strength, as seen in Figure 29. Concurrently, prior research suggests that pre-existing micro-cracks may be closing during the early portion of the curve until the stress creates more micro-cracks that grow larger until they develop into macro-cracks. The transition in the cracks in macro-scale appears to occur around 80% in our experiments.

In contrast, the plot of B values appear to follow a bilinear trend. In this case, the data points appear to increase along one slope linearly until the specimen approaches failure. Around 90% of the ultimate strength, the slope of the trend appears to change instantaneously to a significantly greater slope. This second portion can likely be attributed to the growth of macro-cracks and the consequently large change in underlying concrete structure. Since the slope rapidly increases, this means the TOF in the 21 direction parallel to load increases more quickly relative to the 23 perpendicular direction. Since the concrete is unconfined in the radial direction, this is consistent with expectations.

In studying the effects of cyclic loading, the results seem to further support the premise that micro-cracking significantly affects the ultrasonic wave velocities under applied stress. This is supported by our observations that the resulting B values generally decrease over time, as the specimens are subjected to repeated loading up to increasing maximum limits. Further work would be required to ascertain whether or not this contribution from micro-cracking is consistent and predictable. In comparing the data from the different loading and unloading cycles, there was a large degree of scatter that was not seen in the cylinder experiments. Although, there are certain

cycles that show a clearer trend than other, it would be beneficial to repeat the cyclical experiments using a revised methodology.

Future considerations will include measuring strain and comparing that to the change in shear wave velocity. In addition to uniaxial members, beam elements are also likely candidates for this approach. Furthermore, this particular experiment was performed on a specimen consisting of only unreinforced concrete. To evaluate this method in a more realistic setting, the study would benefit from experiments on specimens containing embedded reinforcing steel. Additionally, in-service structures would benefit from a similar understanding of the acoustoelastic effect in not only members in compression, but also beam elements in flexure. During the development of this technique, it would also be important to study the effects of different material composition and environmental effects. To conclude, as this method is further developed, there is potential for using polarized shear waves to estimate the in-situ stresses in structures.

Chapter 3

DIFFUSE WAVE FIELDS

3.1 Research Goal

Ultrasonic inspection traditionally relies on an operator moving a transducer (or an array of transducers) across a surface to search for a critical flaw which can be time consuming. Another approach is acoustic emission monitoring where a large number of sensors are installed on the surface to monitor for fracture events [49]. In this case the monitoring system has to be working continuously to ensure no events of interest are missed. In this research we explore an approach where a small number of transducers is used to monitor changes remotely with minimal work and energy required after setting up the system. The route we chose to achieve this is by analyzing the late portion of a received ultrasonic signal, also known as diffuse wave field, resulting from an active source after scattering has occurred throughout a structural member. More recently diffuse wave fields have also been referred to as coda waves [50]. Both terms will be used interchangeably from now on. Due to the extreme sensitivity of the diffuse wave field, a system where the transducers are not moved is necessary [51]. Currently, there are no widely accepted methods or standards for correlating changes in the diffuse wave field for flaw characterization.

In this study, we have two goals: (1) to evaluate the use of diffuse wave fields measured with few sensors for detecting flaws in structural steel members and (2) to

establish a methodology to correlate the measured signals with the size of a flaw. For future work, we believe this would provide a foundation for extending the methodology for also locating the flaws. While considerable research has recently been performed in utilizing coda wave interferometry (CWI) for civil engineering applications [50], in our study we simply compare two wave forms collected from two different damage states. For this study we define increasing damage with the increasing length of the introduced flaw, i.e. groove. One limitation of this study is that we did not consider the effect of temperature variation. This has been shown to influence ultrasonic wave propagation in steel [11] but it could also be controlled in a real-world scenario by taking the measurements at a defined temperature.

The historical background and explanation of diffuse waves is presented in Section 3.2.1. This is then followed by an overview of the experimental setup and testing procedures in Section 3.3. After the general information is presented, this leads into the data analysis and discussion of the results in Sections 3.4 and 3.5.

3.2 What are Diffuse Wave Fields or Coda Waves?

The current understanding of diffuse ultrasonic elastic waves stems primarily from two different sources. From one branch, the principles of room acoustics (which originated in the 1940s) were adapted to diffuse waves in elastic solids in the 1980s through the work of Egle and Weaver, both theoretically and experimentally [52], [53]. Meanwhile, the analysis of coda waves originated in the 1960s through the work of Aki to extract information about the change in subsurface stresses due to earthquakes [54]. Whether called diffuse waves or coda waves, the subject is the same.

3.2.1 Development of Methodology

Initially, the coda information was discarded in analyses due to their ostensibly random nature. During the nascent years of research, laboratory ultrasonic research focused on analyzing spectral energy distributions, assuming that phase information is lost through the scattering process. In contrast, the seismic analyses focused more on velocity changes in the diffuse wave field. In the 1980s, Poupinet et al. [55] proposed the seismic *doublet* technique, which in recent years has come to be known as *coda wave interferometry* (CWI). This method compares the phase shift in the coda portion of two signals within discrete time windows. Incidentally, this technique is similar to diffuse wave spectroscopy (DWS) used in the field of optics. More recently, *stretching* of the time axis has been developed as an alternative technique for analyzing velocity changes under the CWI umbrella [56].

In a solid material, an ultrasonic pulse generates a wave field consisting of the ballistic (coherent) direct arrivals in the beginning and a diffuse (incoherent) wave field afterward – also known as the coda (Figure 36). The loss of coherence in this latter portion is a result of wave scattering in the medium. Central to diffuse wave theory, the total wave field is the sum of all waves travelling along every possible path as they scatter throughout a medium. In a relatively homogeneous medium such as steel, the diffuse field is generated by multiple scattering and reflections from the plate boundaries and discontinuities (e.g. flaws). In comparisons of similar signals, the early portions of the signals may be well aligned, such as in Figure 36 b, but they slowly adapt different features in later portions of the coda (Figure 36 c).

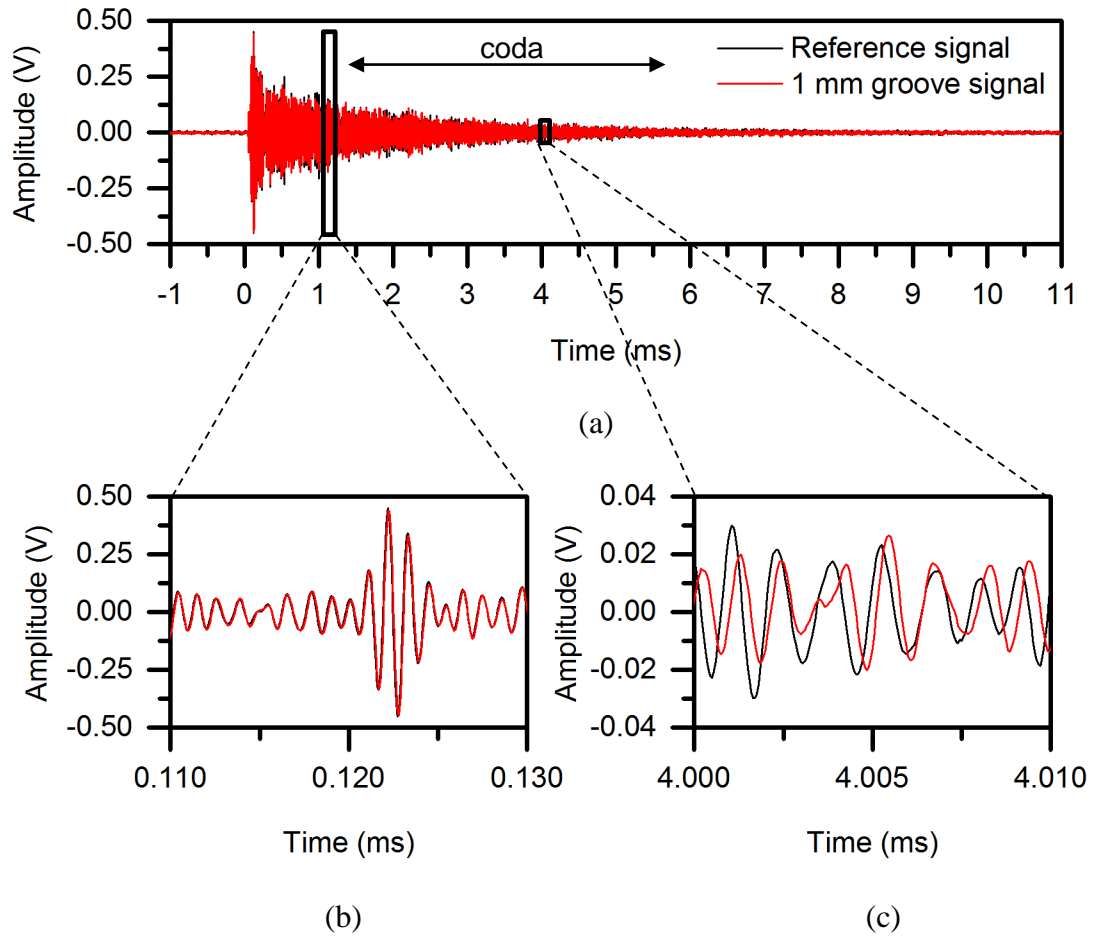


Figure 36: Entire recorded signal of Plate 2 baseline and with (a) 1 mm groove and magnified portion of (b) coherent and (c) incoherent (diffuse) portion of wave field

Although the diffuse portion appears random and has proven resistant to quantitative analysis, there is an advantage to analyzing this portion compared to the coherent field. As the scattered waves travel along longer paths, they become much more sensitive to changes in the medium. In fully diffuse fields, ultrasound has been used to both detect damage and also reconstruct local elastic behavior from remote sources and accurately estimate the Green's function [39], [57], [58]. As the traveled

wave path increases and waves propagate over a damaged area multiple times, this amplifies the change in the signal.

Conventionally, ultrasonic testing focuses on the variation in velocity from the direct waves. However, since this approach only allows the induced stress waves to sample a feature (or defect) only once, the resulting change may be too small to produce reliable results. While the sensitivity increases over time, it comes at the loss of clear spatial information present from the direct waves, experiencing exponential decay through the coda. Consequently, selecting an optimal portion of the recorded signals to study may be highly dependent on the conditions during an experiment. In this study, we seek to balance the loss of spatial information with the sensitivity to change in the recorded signals.

Although many methods for applying diffuse wave theory have been proposed through the years, few NDT and SHM applications have progressed beyond laboratory testing. CWI has been extensively applied to geophysics problems and starting in the early 2000s, has also been adapted for laboratory testing of solids such as aluminum [59] and concrete [4] [39] [40] [60] [61]. In general, ultrasonic waves have an inherent advantage that they are sensitive to changes, even to the point of detecting changes at the microstructure level, such as we saw in our coverage of acoustoelasticity in Chapter 2. Although the computation we propose is different from those established by other researchers, it is consistent with other methods in that it proposes a way to quantify small signal differences between a measured signal and a previously recorded baseline signal of the undamaged structure [62]. We follow the methodology proposed by Grosse [63] using the concept of magnitude squared coherence (MSC). We also consider both passive and active testing.

3.3 Coda Wave Experiment

3.3.1 Specimens and Test Setup

In this chapter, we discuss the experimental process, the results and present the analysis and discussion centered on coda waves. Two experiments were performed, one on each of two identical square 305 x 305 mm (12 x 12 in.) Grade A36 steel plate with a thickness of 19 mm (0.75 in.), designated as Plate 1 and Plate 2.

The setup is illustrated in Figure 38, showing the placement of the Glaser/NIST point-contact sensors (Figure 37) on the two different test specimens and the location of the cut groove. These sensors provide unique capabilities as they have been found to be extremely sensitive while having a flat frequency response over a large frequency spectrum [64]. Additionally, they have a very small aperture size, or tip diameter (approx. 1 mm dia.) which allows for an open sound field. This is seen as advantageous since we are trying to penetrate the entire steel plate with one ultrasonic pulse without focusing in a particular direction. The sensors are positioned such that a transmitter is mounted on one side of the plate and the receivers are placed in arbitrary locations around the plate boundary. For Plate 1, one transmitter and receiver each were used. In contrast, one transmitter and two receivers were used for Plate 2.



Figure 37: Point-contact sensor used in the experiment

An arbitrary waveform generator in conjunction with a high-fidelity amplifier were used to generate the input signals (Figure 39). Both the transmitted and received signals were amplified and recorded by a high-speed data acquisition system and transferred to a standard personal computer. This recorded data was then used to perform the analysis. The analytical procedures that were followed for Plates 1 and 2, and each will be explained in detail in Sections 3.4 and 3.5.

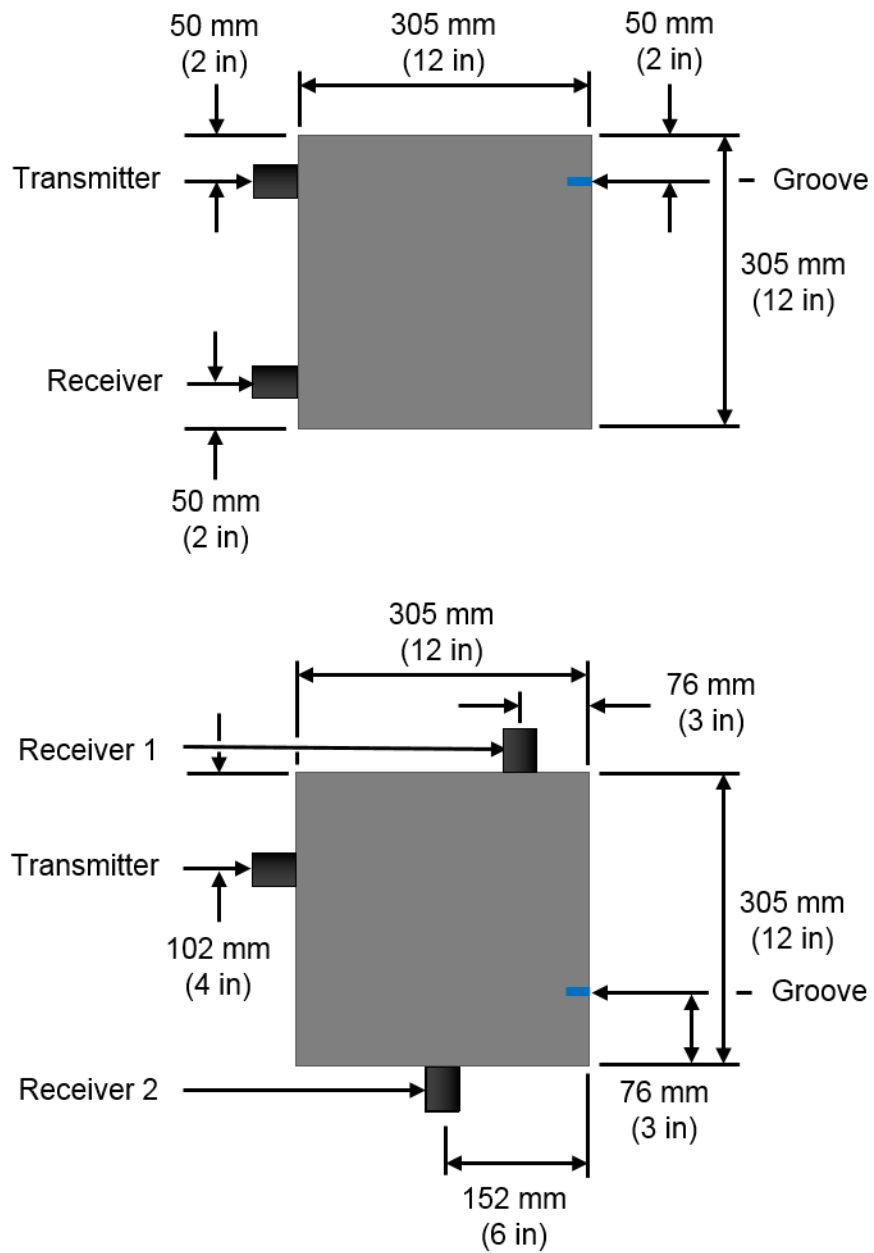


Figure 38: Dimensions of test setup for (top) Plate 1 and (bottom) Plate 2

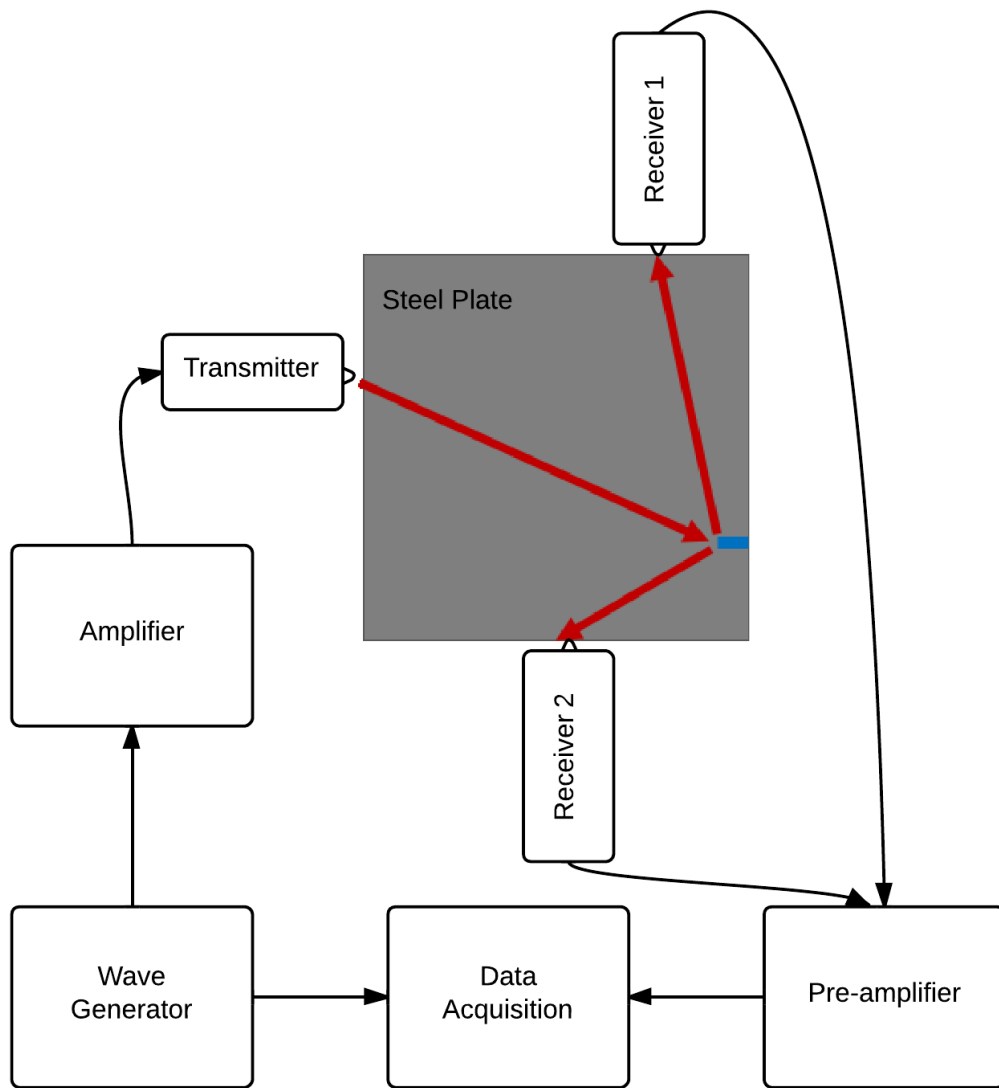


Figure 39: Test setup for ultrasonic wave measurements with Glaser/NIST point-contact sensors for Plate 2 to measure signals with increasing groove size. The direct (= shortest) wave paths are indicated by red arrows

The measurements were taken with the following equipment:

- Three high-fidelity Glaser/NIST point-contact sensors
- Elsys AG TraNET 4045 data acquisition system
- KRN AMP-4BB-J amplifier (to amplify signal from receiving transducer)
- Trek 2100HF amplifier (to amplify signal from waveform generator)
- BK Precision 21.5 MHz waveform generator
- PC running TranAX data acquisition software

3.3.2 Testing Overview

First, for each of the two experiments, three sets of baseline measurements were collected from the undamaged specimen using a 1 MHz Morlet-type pulse as illustrated in Figure 41 (bottom). The sampling rate was 20 MHz with low-pass anti-aliasing filters set to 2 MHz. The data acquisition system was set up to record for a duration of 12 ms in order to adequately capture both the coherent and the diffuse wave portions of each generated signal. Ultimately the analysis is performed on a partial signal window, excluding data irrelevant to the study. Subsequently, a full depth groove (width approximately 1 mm) was introduced into one side of the plate (Figure 40), and increased in length in approximately 1 mm (0.04 in.) increments. For Plate 1, this was increased until a depth of approximately 10 mm (0.4 in) was reached. For Plate 2, the groove was increased in depth until approximately 13 mm (0.5 in). For this plate, a last cut was performed to increase the groove to 30 mm (1.18 in.) depth before taking a final measurement. For each groove depth, three sets of measurements were taken. For Plate 1, two scenarios were considered: one using just the receiver to

passively recording without a coherent source and one using the transmitter to induce the ultrasound pulse and then receiving the resulting output. The analysis was performed using MATLAB, Microsoft Excel, and OriginPro. The proposed technique for analyzing the condition of the plate is explained in the next section.

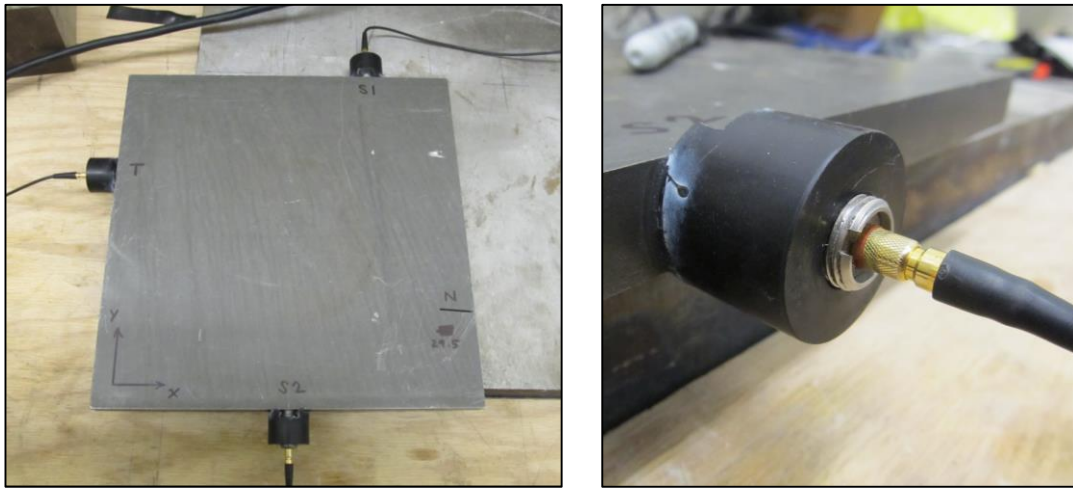


Figure 40: (left) Test setup for Plate 2 with one transmitter T and two receivers S1 and S2 and (right) close up of sensor mount with attached cable at S2

3.4 Data Analysis

Due to the ultrasonic waves propagating in all directions throughout the steel plate, there are many different possible travel paths for a wave travelling from the transmitter to arrive at the receiver. As shown in Figure 41, these paths include direct, singly-scattered and multiply-scattered waves. With the continual recording of the received signal, the coda portion consists of waves travelling from all directions as a result of multiple scattering on the plate boundaries and internal discontinuities such as cracks. There is energy being transmitted even considerably after the first direct

arrival of the wave, albeit with decreasing amplitudes. This information can be detected in the signal until the energy has completely dissipated and only random noise remains.

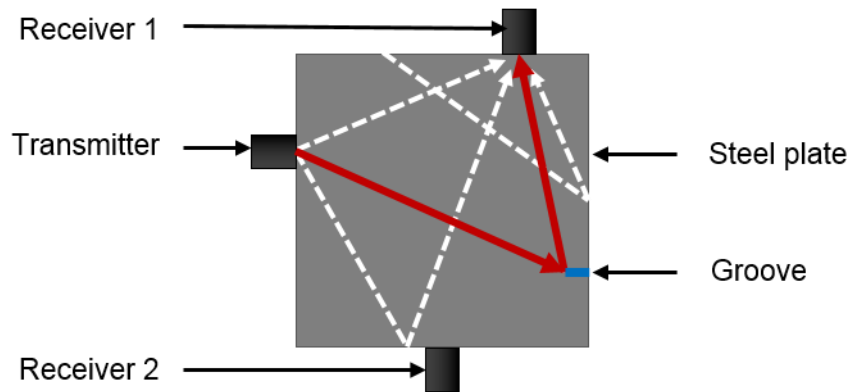


Figure 41: Selection of possible travel paths to arrive at given receiver, for waves traveling through plate and reflecting off flaws and boundaries

An example of the received signals is shown in Figure 42. The direct wave arrival occurs early in the recording, starting around 0.07 ms. At this point, the originally transmitted Morlet-wavelet is seen clearly, containing the greatest degree of energy (highest amplitude). It is possible to calculate the different *times of flight* (*TOF*) in this arrival from one signal to the next, analogous to what we did in Chapter 2. However, as we will see in Section 3.5, this method lacks sensitivity to small changes in damage in the unstressed specimen and does not provide the desired quantifiable information about the analyzed system. In order to compare the reference

and groove signals, we use both *cross-correlation* and *magnitude-squared coherence* (*MSC*). We also try analyzing the signals in both fixed windows and sliding windows.

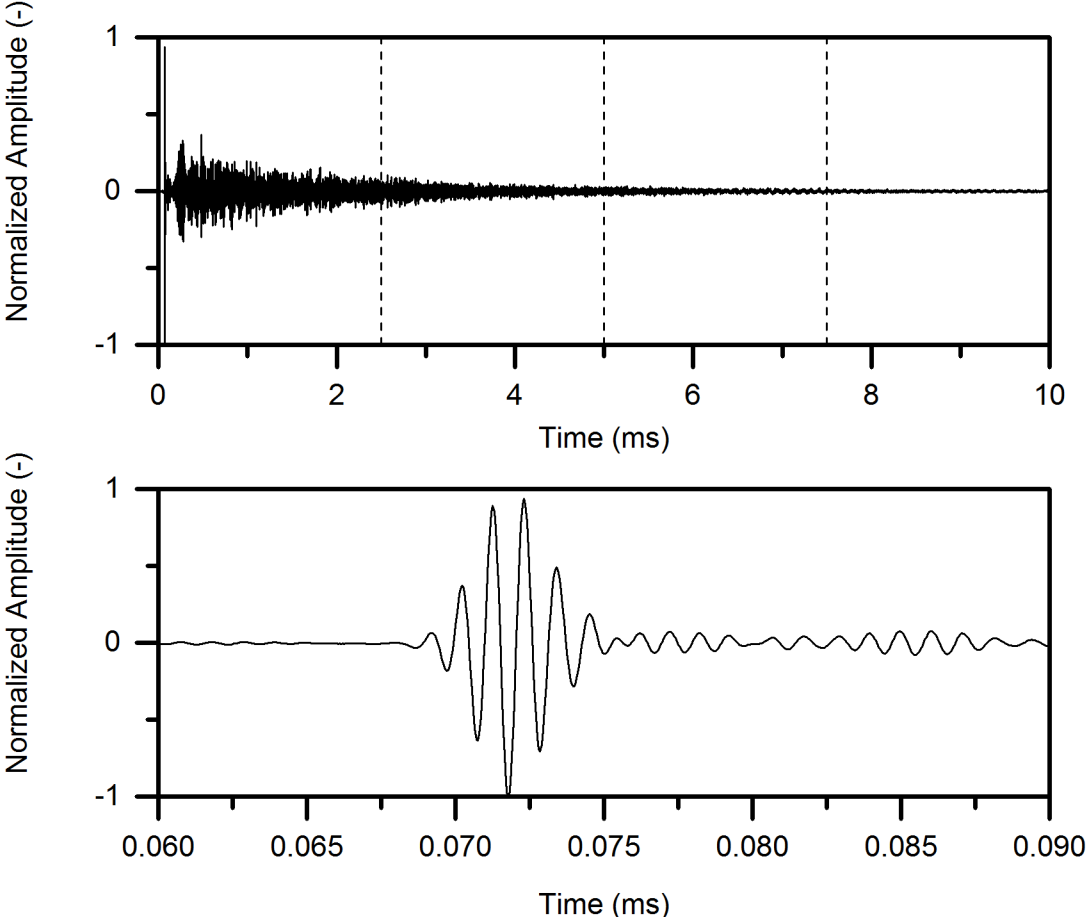


Figure 42: (top) Analyzed portion of Plate 1 signal divided into four equal windows with (bottom) zoom-in of initial wave arrival at the receiver

3.4.1 Cross-correlation

Cross-correlation is a signal processing technique commonly used to analyze diffuse wave fields, in order to identify the time lag between two different signals of identical length. The true cross-correlation sequence and is defined as [65]:

$$R_{xy}(m) = E\{x_{n+m}y_n^*\} = E\{x_ny_{n-m}^*\} \quad (9)$$

where x_n and y_n are the two compared signals, from $-\infty < n < \infty$ and $E\{\cdot\}$ is the expected value operator. In MATLAB, the cross-correlation is taken as a vectorized finite sequence and takes a sliding dot product of the signals to obtain a function of twice the length of the original signals. An underlying assumption is that the compared signals are indeed similar. If they are not, then the cross-correlation may produce erroneous results. This is what happens when a signal is dominated by noise.

In the resulting function, the point with the largest value indicates the greatest degree of alignment between two signal features. In other words, this is a measure of lag between the two signal features. However, since the experiments are performed in a lab setting under fixed temperature conditions and there are no resulting geometric changes, the difference between signals is expected to be minimal and possibly insignificant.

3.4.2 Magnitude-squared Coherence

More importantly, this analysis focuses on the use of statistical *magnitude squared coherence (MSC)*, which is defined as [66]:

$$C_{12}(f) = \frac{|P_{12}(f)|^2}{P_{11}(f)P_{22}(f)} \quad (10)$$

where $P_{11}(f)$ and $P_{22}(f)$ are the power spectral densities of signals 1 and 2 (of the same length), and $P_{12}(f)$ is the cross power spectral density. As a result, $C_{12}(f)$ is a function of normalized frequency and varies between 0 and 1. By taking the integral of this function numerically, we can calculate one single value representing a measure of similarity between two signals [63]:

$$MSCI = \int_0^1 C_{12}(f) df \quad (11)$$

This new value, called a *magnitude squared coherence integral MSCI*, is between 0 and 1, where 1 indicates the two signals are identical. For example, Figure 43 shows the result of $C_{12}(f)$ between two identical signals, resulting in $MSCI = 1.0.$, whereas Figure 44 shows two compared signals with resulting $MSCI = 0.2.$

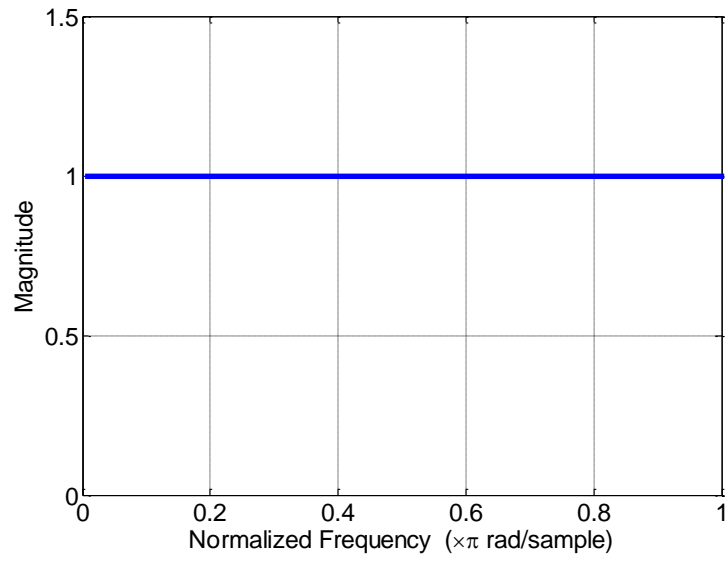


Figure 43: Example of *MSCI (MSC Integral) = 1.0*

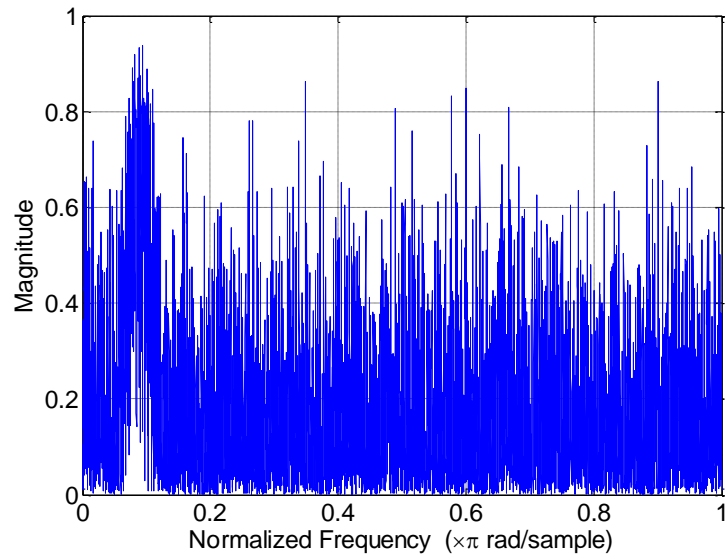


Figure 44: Example of *MSCI (MSC Integral) = 0.2*

3.4.3 Fixed vs Sliding Windows

To account for the changes in the signal due to increasing groove size (= increasing damage), our initial analysis was performed on Plate 1 (Figure 38 top). First, *cross-correlation* and *MSCI* values were determined between the reference signals, showing they were identical. Afterward, each grooved signal was compared to the reference baseline, first using the entire signal and then segmented into separate fixed windows in the time domain.

For example, segmenting a pair of signals into $N = 4$ windows looks like Figure 42 (top). Instead of one single value representing the level of similarity for each groove depth, there are four. Following these comparisons, first the signals were time-shifted based on the results of the *cross-correlation* before performing the *MSCI* computations. The results of this approach are detailed in Section 3.5.1.

For Plate 2, *MSCI* is calculated using a sliding window of fixed length in the time domain. Part of the difficulty is in deciding what the ideal window length is for the signal comparison. A shorter window offers more sensitivity but important portions can potentially be missed. Yet, a longer window increases the likelihood of capturing signal differences but the sensitivity is less due to the averaging effect that the longer window has. After comparing several options, a window of 500 points appeared to be an acceptable compromise.

For each window location, the individual *MSCI* values were computed which generated a data point at each window location – corresponding to a given time in the compared signals – and results in a curve that represents their similarity as a function

of time. The benefits of this approach compared to the static window approach is discussed in Section 3.5.2.

3.5 Results and Discussion

In this simplified laboratory study, the studied specimens have a simple geometry and were maintained at an approximately constant temperature during each recording. Since the change in the signal is dependent primarily on the introduction of a discontinuity in the plate and not due to a geometric change or environmental effects, no stretching of the signal was expected. As a result, any deviation in the signal from the baseline should result from a change in the damage level in combination with noise.

3.5.1 Static Windows

Using Plate 1, the initial testing was performed to determine the feasibility of using *cross-correlation* and *MSCI* in order to detect the changes in the groove depth. First, the passive measurements were analyzed, where the receiving sensor recorded for the set time without any external excitation. Secondly, the measurements are considered where the transmitter first induced the ultrasonic pulse.

3.5.1.1 Passive Measurements

The values of *cross-correlation* and *MSCI* for the passive measurements are plotted as a function of the increasing groove depth. Although the values are not constant, the variance is small and more importantly, do not appear to follow any distinct trend (Figure 45). First shifting the signals by identifying the points of peak

similarity by using cross-correlation and then performing the *MSCI* did not have a significant effect.

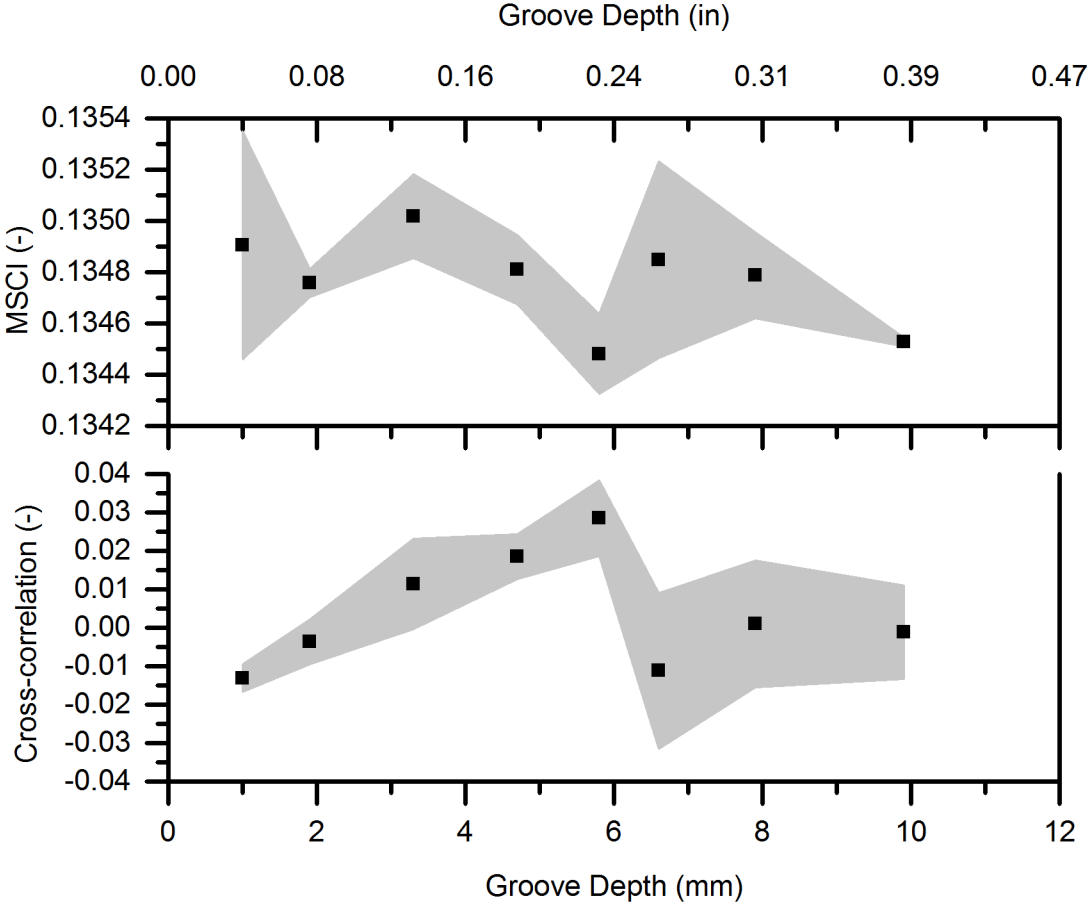


Figure 45: (top) *MSCI* values and (bottom) cross-correlation plotted vs change in groove depth for Plate 1

After comparing the entire signals to each other, this procedure was carried out by dividing the signals into varying numbers of segments (windows). Even by breaking the recordings down into small segments, there did not appear to be any

distinct change to the results. Consequently, this shows that these methods were not sensitive to the change in groove depth in the steel plate specimen. This would have had the advantage that active transmitters would not be required in a SHM application and follow an approach similar to that of acoustic emissions.

3.5.1.2 Active Measurements

Instead of relying on detecting changes in the plate passively, the next analysis is on the data collected after first transmitting an ultrasonic pulse on one boundary of the specimen. Also, it may be worth noting that time-shifting the signals prior to calculating the *MSCI* based on *cross-correlation* was determined that this had a negligible effect on the resulting *MSCI* values, as previously predicted. This was prevalent across the experiments testing the use of coda wave analysis.

The analysis was performed using windows, numbering $N = 1, 2, 4, 8, 16$ and 100 . The trend from each of these cases were similar and representative examples are shown in Figure 46—analyzing the entire signals (one window) and dividing the signals into four windows ($N = 4$)—and Figure 47 which considers a hundred windows ($N = 100$). Since the standard error for the measurements were small and standard error bars would interfere with the presentation of the data, shaded lines were used instead to indicate the error.

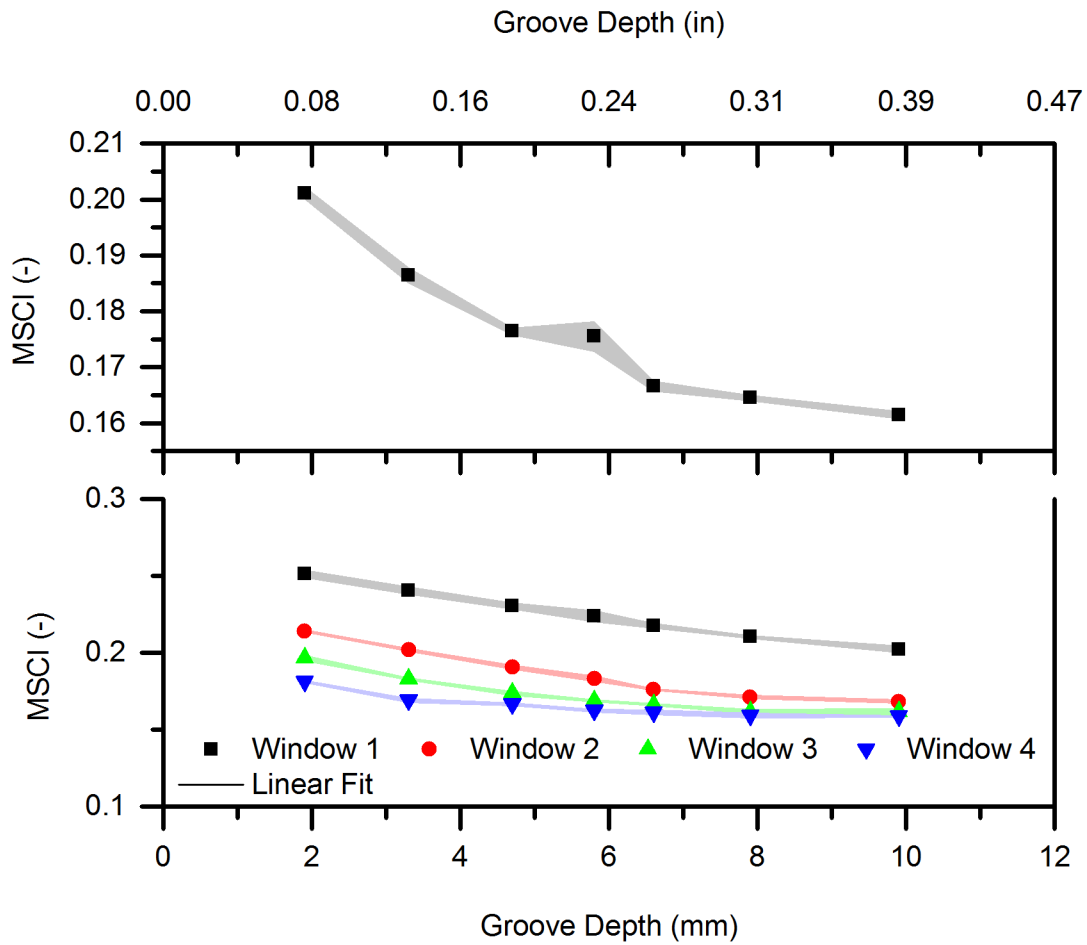


Figure 46: *MSCI* values for Plate 1 (top) comparing the entire signals of different groove depths with reference and (bottom) using four static windows

Compared to the ambient measurement results, an observation can already be made from the *MSCI* values of $N = 1$. As the groove depth is increased, the *MSCI* value decreases and thereby indicating that the recording possesses a decreasing similarity to that of that original undamaged specimen. Since the reference measurements were not accurately recorded during the experiment, for the sake of this analysis, the signals recorded for the 1 mm deep groove were used as the baseline.

From Figure 46 (bottom), it can be seen that the different windows contain different information. The magnitude of the values drop in the later windows, which correspond to later time in the recorded signal. This is consistent with the understanding that waves continue to scatter and propagate throughout the medium, the features become increasingly indistinguishable. Aside from this, the data points appear to follow a similar trend. The difference between the different windows can be seen more clearly in the context shown in Figure 47 and corresponding Table 5. In this figure, the signal is divided into smaller portions (100 window). Each window represents a smaller portions of the total signal. Thus, the local variations over the course of a signal are more defined. In this plot, the *MSCI* values are shown for selected windows.

Window 1 contains primarily random noise and as a result, there is very little change in the computed values. However, as we look later in the signals with the later windows, there is a trend that the slope is becoming increasingly negative. At Window 10, this peaks and also corresponds to the highest R^2 value for the linear fit. After this point, the trend begins to reverse. In Window 100 (the last portion of the analyzed signal), the slope becomes relatively flat again, with characteristics similar to that of the first window. Both of these contain primarily noise. However, the difference between the two is attributed to the fact that in Window 100, the energy from the initial excitation pulse has not completely dissipated from the coda. Thus, stress waves are still continuing to propagate throughout the plate—albeit with lower intensity.

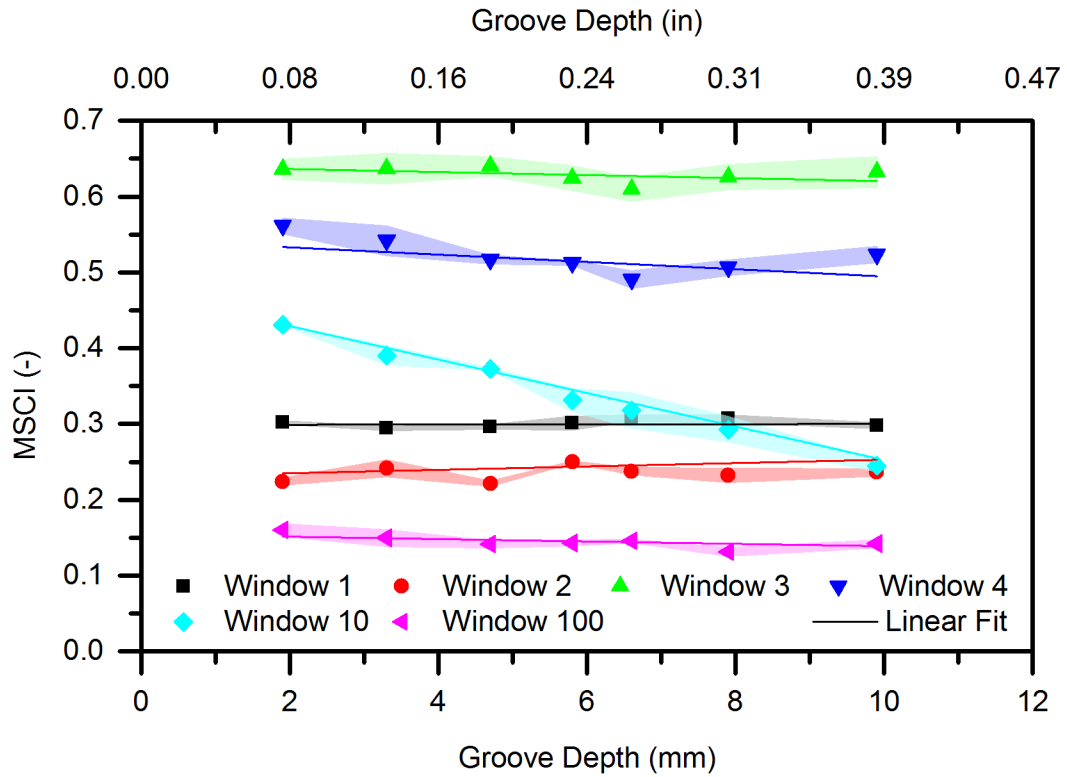


Figure 47: *MSCI* values in Plate 1 analyzing the signal in 100 static windows

Table 5: Linear fit values corresponding to specified windows analyzing *MSCI*

<i>Window</i>	R^2	Slope
<i>1</i>	0.1309	0.0001
<i>2</i>	0.0293	0.0022
<i>3</i>	0.3184	-0.0020
<i>4</i>	0.6397	-0.0048
<i>10</i>	0.9551	-0.0221
<i>100</i>	0.2036	-0.0016

The drawback of using a fixed window approach is that this is a time consuming process and moreover, given signals from testing of structural members of varying geometry, it would require identifying an optimal window from which to draw conclusions. Additionally, Window 10 which appeared to produce a fit with the highest slope has MSCI values ranging within 0.2 of each other. If there is a way to further increase the sensitivity of defect detection and characterization, this would be preferable. Consequently, the experiment on Plate 2 was performed using sliding windows, based upon the foundation established with Plate 1.

3.5.2 Sliding Window

3.5.2.1 Receiver 1

Although the later portions of the coda wave have been demonstrated to provide more information than the earlier portion of the signal, this benefit needs to be weighed against the increasing presence of noise. In the tested steel plate – and typical of complex structures – not only does the signal amplitude decay exponentially but the signal is also accompanied by random noise. Thus, the results will change depending on the portion of the signal analyzed. As a result, identifying the portions of the signal that contains the clearest relationship between the recorded signals and degree of damage is critical to this method. Figure 48 visually shows this process with Receiver 1 and Figure 52 for Receiver 2 for comparison.

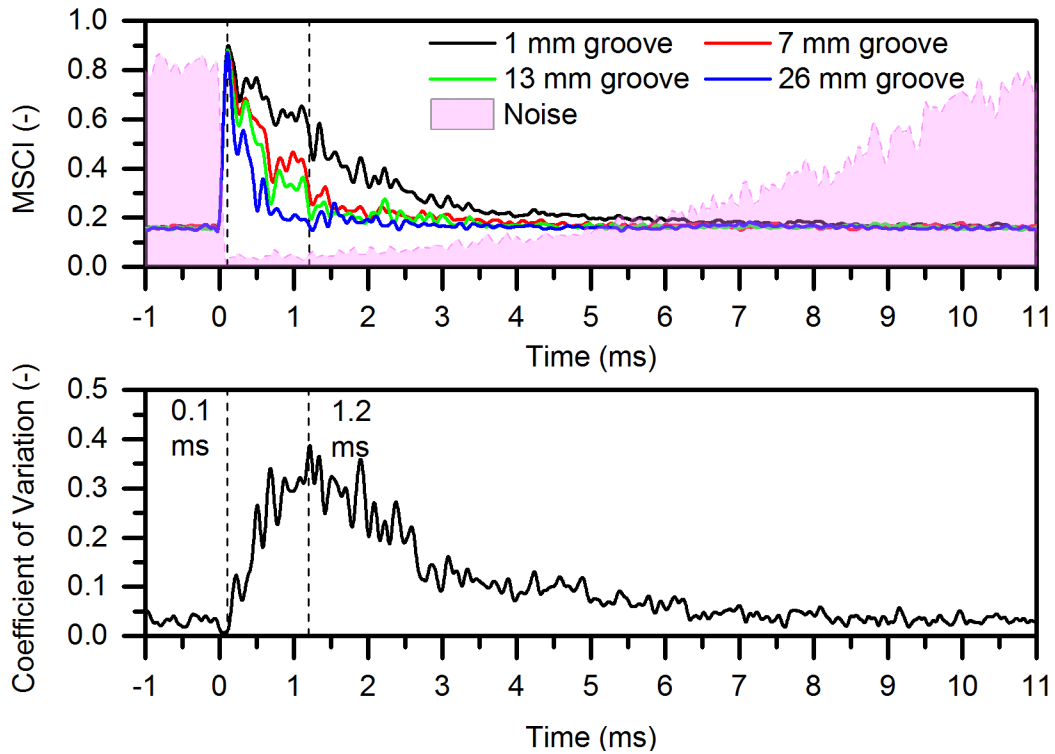


Figure 48: (top) *MSCI* between the baseline and signals from the grooved Plate 2, Receiver 1 with noise shown as shaded area and (bottom) the coefficient of variation (CV) showing dispersion between all sets of *MSCI* with first wave arrival and point of maximum dispersion marked with dashed lines

In order to compare the different signals, it is useful to consider the effect of noise on the system. To this end, the *MSCI* is computed between two baseline signals under essentially identical conditions. The inverse of this curve can be interpreted as the normalized noise-to-signal ratio and is shown as the shaded area in Figure 48 (top). In order to minimize the signal fluctuations, the curve was smoothed using a fast Fourier transform (FFT) filter, removing frequencies over 10 MHz.

At the beginning of the recording until the receiver first detects the most direct path input wavelet at approximately $t = 0.04$ ms, there is no correlation between the two signals, and hence there is only noise. As soon as the pulse arrives, the noise no longer dominates the signal and the value of the *MSCI* spikes to a high value. This peaks at 0.1 ms, approximately when the first reflection off of the groove is expected to arrive at the receiver. After this reflection arrives at the receiver, the *MSCI* immediately begins to drop sharply, indicating a difference between the signals. As energy continues to dissipate through wave scattering, the noise increases and at the end of the recording, the signal approaches pure noise.

Representative curves comparing the signals recorded on the plate with increasing groove side and the baseline are overlaid onto the same plot. These are also smoothed following the same procedure as the aforementioned noise indicator. While the *MSCI* equals approximately 0.9 for each curve soon after the receiver first detects the input wave, the signals are influenced by singly and multiply-reflected waves. Thus, the curves spread out before starting to once again converge as time increases.

In a conventional ultrasonic test, the analysis would focus primarily on the early portion of the recorded signals. In a magnified plot of the post-processed signals (shown in Figure 48), it is apparent from Figure 49 that each of the computed curves are nearly identical towards the beginning of our recording. There is almost no sensitivity to changes from the groove by comparing the effect of the direct waves. In comparing the *MSCI* values for each groove signal, the peak value always occurred at either $t = 0.109$ or 0.104 ms. Note that this is the result of analyzing post-smoothed curves. Yet, even considering the original data set, the peak value is also relatively constant at $t = 0.089$ ms. Firstly, this confirms that the smoothing process decreases

the accuracy of spatial information. Furthermore, this demonstrates that for this method, looking at the earliest portion of the signals does not produce favorable results. In contrast, we know that analyzing the latest portions of the signals, noise dominates and again no usable information can be extracted. As a result, the desired information is likely within these two extremes.

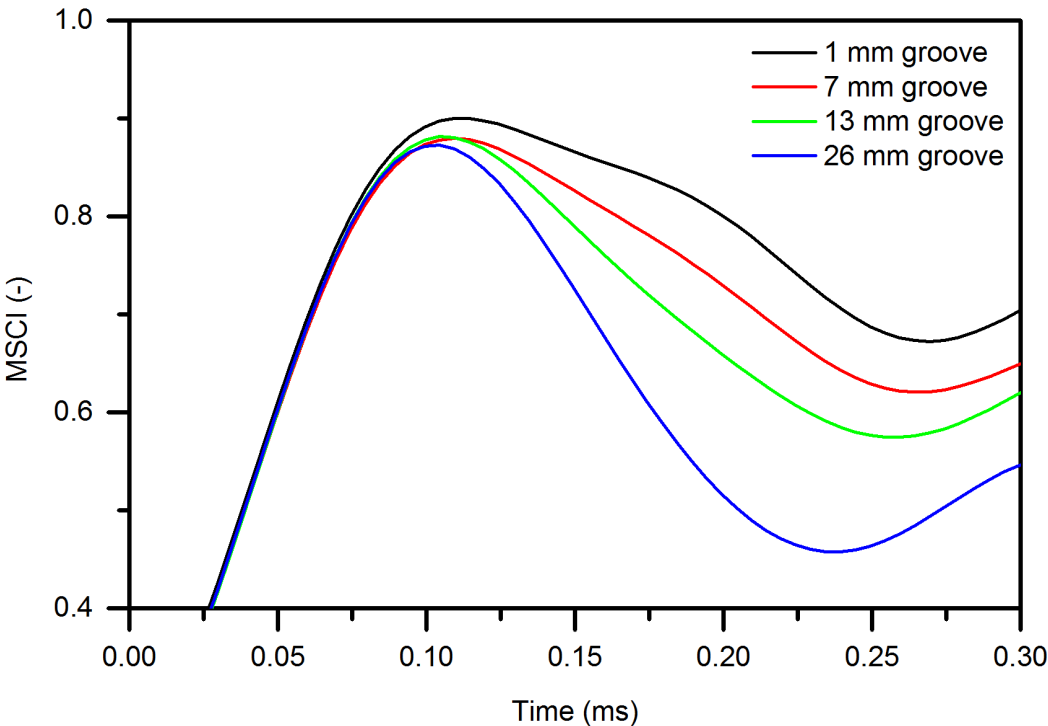


Figure 49: Magnification of first arrival of ballistic (direct) waves shown as *MSCI*

We can determine where this is by analyzing the signal-to-noise ratio. To this end, we consider the degree of dispersion between all of the *MSCI* curves. In order to measure this dispersion between the curves, the *coefficient of variation (CV)* was computed as a function of the *MSCIs* at each recorded groove depth for each time

window location. This value indicates how well the different *MSCI* curves are separated. This in turn can be interpreted as a measure for the sensitivity of the *MSCI* as a function of time. In Figure 48 (bottom) it can be observed that the variation between the curves for Receiver 1 increases steadily and peaks around 1.2 ms before decreasing and approaching zero. This is similar to the pattern exhibited even when there is no smoothing performed on the *MSCI* curves prior to computing the *CV*. However, pre and post-smoothing both serve the purpose of discriminating between the absolute peak and local variations.

To better understand the significance of these *MSCI* and *CV plots*, we now look at the original recorded signals during different times. Figure 50 (top) shows that as the groove size increases, the signals deviate further from the baseline measurement. Around time $t = 1.2$ ms, the waveforms exhibit similar amplitudes and a slight phase shift. This may be an experimental error since our specimens did not experience geometric distortions, e.g. caused by temperature changes.

In the later portions of the coda (Figure 50 bottom), the waveforms seem to be much more different and those differences not associated with a simple phase shift. Furthermore, the dissimilar waveforms are further complicated by varying amplitudes. Although the nature of the signals appears random and distinct spatial features are indistinguishable, this portion of the waveforms is more sensitive to changes to the studied medium.

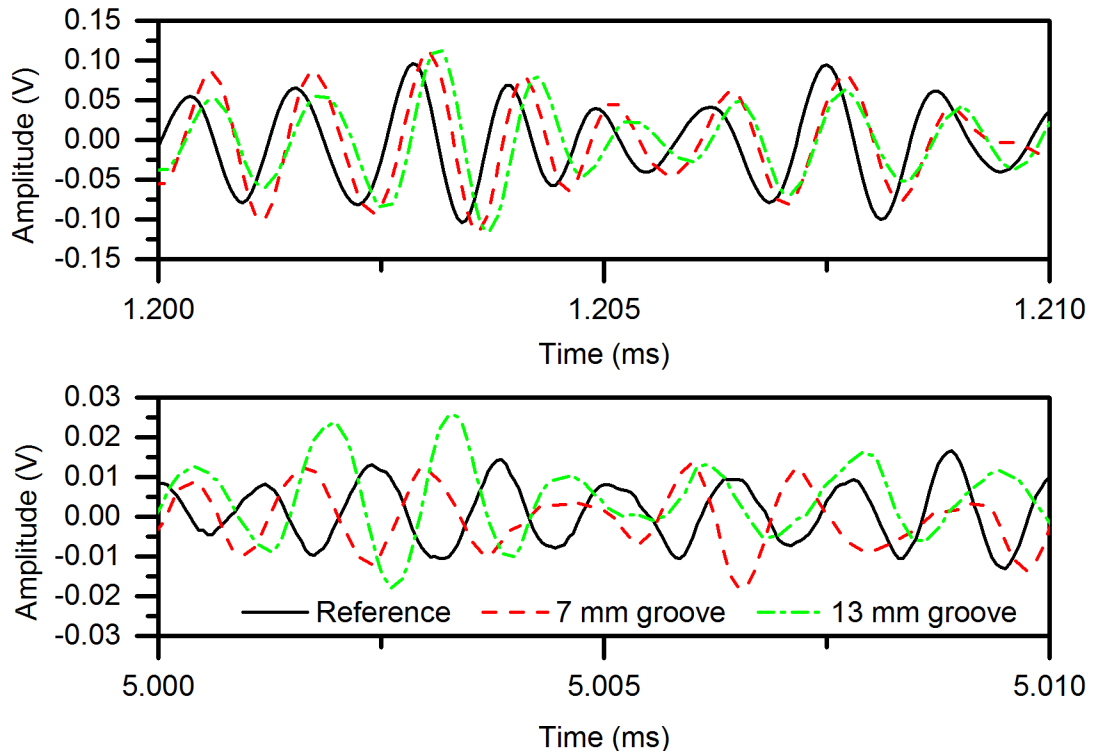


Figure 50: Amplitude comparison between (top) baseline signal and increasing groove size signals in time window in early portion of coda and (bottom) later in the coda as waves continue to scatter in the plate

Figure 51 shows discrete slices of the *MSCI* curves extracted from Figure 48 (top), corresponding to the similarity between the baseline and damaged signals at a given time. The earlier determined time $t = 1.2$ ms is compared with (1) only noise at $t = -0.5$ ms; (2) a still fairly coherent portion at $t = 0.5$ ms; and (3) an incoherent portion with moderate noise at $t = 5$ ms. Furthermore, each of these are likewise compared to the results of the *MSCIs* calculated between the entire recorded signals. Each of these were fitted with an exponential curve, aside from the results for $t = -0.5$ ms which showed a fairly constant *MSCI* value due to the randomness of both compared signals at that point in time. Although the coherence between the entire

signals showed the best fit, with a squared correlation coefficient $R^2 = 0.99$, the values vary relatively little as a function of groove depth indicating there is not much sensitivity.

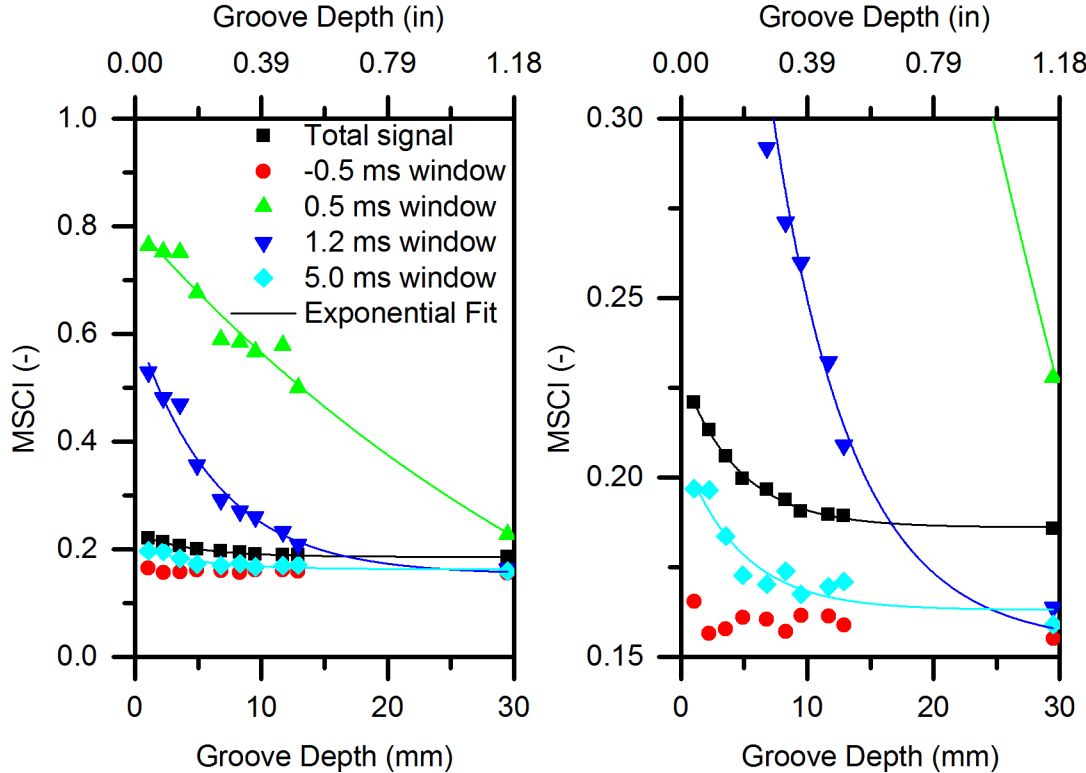


Figure 51: *MSCI* as function of damage level between entire recorded signal and results of time window approach with fitted exponential regression models (left) and magnified plot of the same results (right) for Receiver 1

A fitted curve around $t = 1.2$ ms gives a better fit than time windows before and after this point, resulting in $R^2 = 0.97$. As a result, although there is slightly more spread, there is an increase in sensitivity and therefore robustness favorable for testing more complicated geometries. The results for $t = 0.5$ ms show the highest sensitivity

but also a larger data spread. For our experiments, it appears that both of these time instances would work. In comparison, these curves are also more sensitive than the ones determined from the fixed window approach detailed in Section 3.5.1.

3.5.2.2 Receiver 2

Next, we consider the data collected from the same experiment at Receiver 2 (placement of sensors shown in Figure 38). In comparison to the previously analyzed *MSCI* and dispersion curves shown in Figure 48, this second set of data shown below in Figure 52 reveals similar results. Just as we saw in Section 3.5.2.1, the *MSCI* for each groove signal peaks around $t = 0.1$ ms. This demonstrates a lack of sensitivity in terms of determining precise *time of flight*, which may be problematic for estimating the location of the groove.

Since the wave path length between the transmitter and each receiver is different, it is expected that in actuality, the *MSCI* will peak at different times. A visual assessment of the pairs of signals received at the different receivers shows that the two have similar shapes. Yet, the signal from Receiver 2 peaks at an earlier time than Receiver 1—consistent with a theoretical computation. For the sake of minimizing computational effort, the sliding window size was determined to be 500 points wide. Additional computations would be required in order to determine whether a small window size would both increase sensitivity to initial wave detection and also provide adequate results for the damage level curves. A refinement of this method or an alternative to determining the *time of flight* from the transmitter to the crack and then to the receivers is a necessary prerequisite for locating an in-situ crack.

According to Tua et al., signals from at least three transmitter-receiver pairs using active transmission are required to unambiguously localize a crack [67].

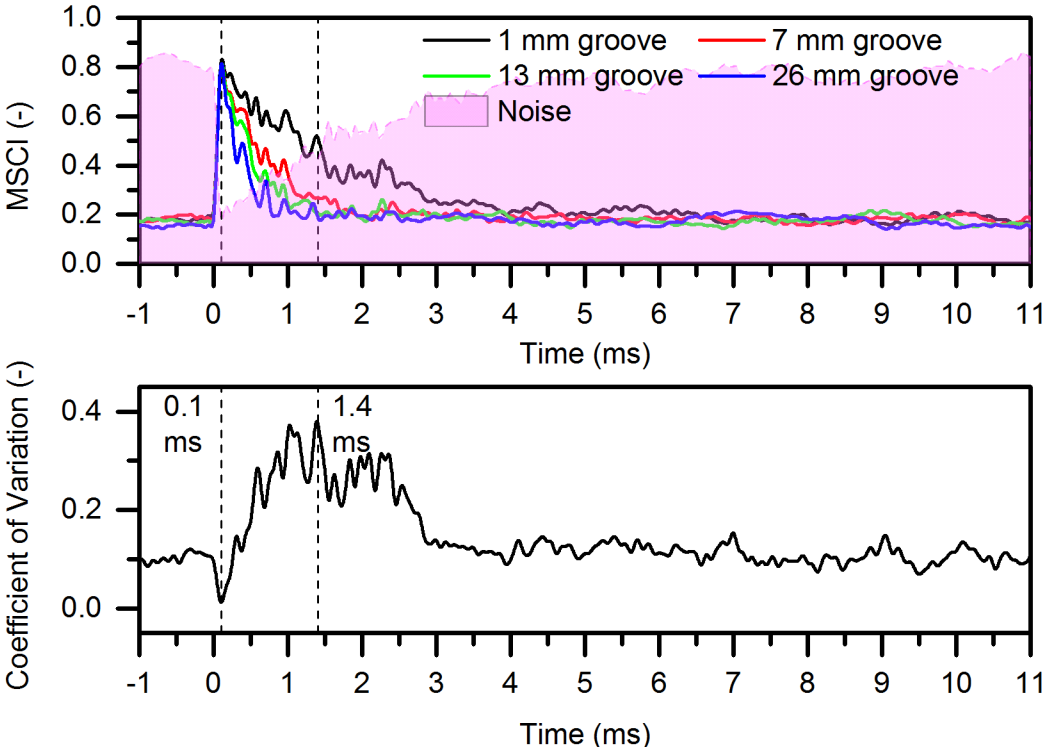


Figure 52: (top) *MSCI* between the baseline and signals from the grooved Plate 2, Receiver 2 with noise shown as shaded area and (bottom) the coefficient of variation (*CV*) showing dispersion between all sets of *MSCI* with first wave arrival and point of maximum dispersion marked with dashed lines

One other difference between the Receiver 1 and 2 data is that the signals recorded by Receiver 2 contained more noise. This is likely a result of the relative placement of the testing equipment in the experimental setup. Despite the presence of considerable noise, following the previously detailed process for determining the

dispersion curve and subsequently extracting the *MSCI* vs Groove Depth curves produces similar results.

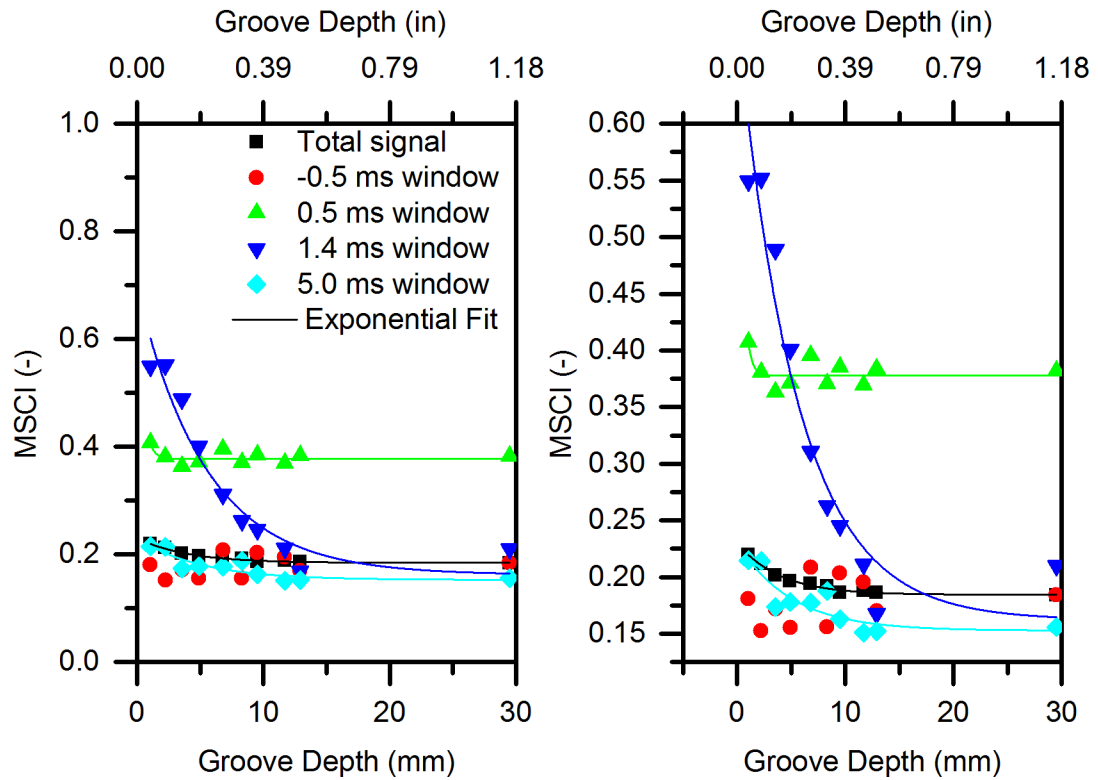


Figure 53: *MSCI* as function of damage level between entire recorded signal and results of time window approach with fitted exponential regression models (left) and a magnification of the same results (right) for Receiver 2

In this case, the maximum dispersion was found at approximately $t = 1.4$ ms. At this time, the *MSCI* follows a similar exponential trend as in Receiver 1, at least for lower groove depths: below 15 mm (0.6 in). For this curve, the fitted line does not match well with the recorded data at 30 mm (1.18 in). Furthermore, unlike Receiver 1, the curve at $t = 0.5$ ms possesses relatively little sensitivity and possesses a lower

MSCI (relative similarity) initially. Although the noise is relatively low at this point during the signal, since the magnitude of noise is higher than at the other receiver, this could contribute to the difference in sensitivity. While there is overall more noise, this is not offset by the additional sensitivity contributed by the additional wave information contained further into the coda. Aside from these differences, the pattern observed from both receivers is similar.

3.6 Conclusions and Future Work

The results of our work show that, at least in a laboratory setting, it is possible to use our proposed *MSCI value* to estimate distinct localized damage to a steel plate of simple geometry. Although passive measurements using our setup did not produce usable results and fixed windows provided limited flexibility, a sliding window approach with *MSCI* provided quantifiable information about the changes to the signals as the groove depth increased. While this is a work in progress and some factors were not considered in this initial study, the results show this approach could potentially be used as part of an integrated methodology for automated damage monitoring.

It is important to consider that for a method to effectively detect damage for in-situ applications, it is necessary to (1) develop a robust method capable of handling complex geometry and (2) discriminate between changes due to the damage and that of environmental effects. Both of these factors require further analysis. To address the first, utilizing different time window lengths and varying the portion of the signals to be analyzed may be adequate. However, it is important to consider that the groove cut into the steel specimens were in close proximity to the attached sensors. Yet, this may

resemble all in-field situations. Since the waves travel in a primarily heterogeneous steel medium, the multiple-scattering relies primarily on the boundaries. If the boundaries in a monitored member are far from the sensors, this may require additional adjustments. This could take the form of using a grid of sensors throughout a critical area or adjustments to the data analysis procedure.

For the second issue, the work of Weaver and Lobkis [51] showed that a complex waveform undergoes a direct dilation when an elastic solid is subject to temperature change. As an extension of this research, Michaels and Michaels [68] and Lu and Michaels [11] analyzed the effects of temperature on damage detection. As a result, likely multiple baselines would be necessary to account for temperature changes, unless the recordings can be taken at approximately the same temperature every time. Additionally, in subsequent testing we intend to utilize the data collected by both receivers together in order to refine the technique for locating the damage location, i.e. crack tip.

Chapter 4

CONCLUSIONS

4.1 Conclusions

This research covers two topics of nondestructive ultrasonic testing. After the general background and motivation was presented in Chapter 1, the remaining of this thesis was devoted to acoustoelasticity in Chapter 2 and coda waves in Chapter 3. In each one, we developed basic research for these topics and proposed methodologies for testing based on our experimental data. These tests were performed in a laboratory setting on both small-scale concrete and steel specimens.

In Chapter 2, we considered the effect of acoustoelasticity in concrete and sought to establish a relationship between applied stress and ultrasonic velocity up to structural failure. The data suggested that the change in behavior of the transmitted ultrasonic waves was explained primarily by acoustoelasticity and micro-cracking. By normalizing the two sets of data from shear waves polarized parallel and perpendicular to the uniaxial load, we established a *time of flight (TOF) ratio B* which we related to the applied stress. As a result, we computed a plot of this *TOF ratio* vs applied stress that showed a clear bilinear trend.

Additionally, this research considered the effects of cyclical loading on the concrete and tracked the changes across varying loading and unloading cycles. Although there was an excessive amount of experimental error introduced into these

tests, the results corroborate the observation that micro-cracking occurs even at low stresses and changes the *TOF* across different cycles at the same stress level.

In Chapter 3, we focused on utilizing the diffuse/coda wave portion of the recorded signals to track changes in damage in steel. In place of cracking in the plate specimens, a notch arbitrarily cut into each plate specimens and then varied in depth was used instead. Through the use of *magnitude-squared coherence (MSC)*, an approximately exponential relationship was fit between the computed *MSC integral (MSCI)* values and the varying groove depth. Through the tested analysis procedure, we sought to balance the noise present in the signals and the sensitivity to change in the coda. The results showed that a sliding window approach performed better than decomposing the signals into static windows.

4.2 Future Work

The viability of using either of the two covered methods for in-situ monitoring strongly depends on the ability to differentiate between the effect of changing stress or damage and the change to ultrasonic signals from environment effects (i.e. cracking, surface changes, and temperature). Additionally, it is necessary to be able to apply the techniques to structural members of varying geometry and configurations. This is particularly important for the *TOF ratio* methodology, due to the nature of the analysis and the complexity of concrete. To make it possible to obtain in-situ measurements, it is necessary to obtain data on more test members that represent varying properties. These include factors such as concrete strength, porosity, and inclusion of steel reinforcement. Finally, further analysis needs to be done for the coda wave methodology in order to provide functionality for localizing damage.

REFERENCES

- [1] G. Workman, D. Kishoni and P. Moore, "Infrastructure Applications of Ultrasonic Testing," in *Nondestructive Testing Handbook Vol 7 Ultrasonic Testing*, P. Moore, Ed., Columbus, OH, American Society of Nondestructive Testing, 2007, pp. 476-491.
- [2] P. Lundqvist and N. Rydén, "Acoustoelastic effects on the resonance frequencies of prestressed concrete beams – Short-term measurements," *NDT&E International*, vol. 50, pp. 36-41, 2012.
- [3] V. Hauk, *Structural and Residual Stress Analysis by Nondestructive Methods: Evaluation – Application – Assessment*, Amsterdam, Netherlands: Elsevier, 1997.
- [4] Y. Zhang, O. Abraham, F. Grondin, A. Loukili, V. Tournat, A. Duff, B. Lascoup and O. Durand, "Study of stress-induced velocity variation in concrete under direct tensile force and monitoring of the damage level by using thermally-compensated coda wave interferometry," *Ultrasonics*, vol. 52, no. 8, pp. 1038-1045, 2012.
- [5] American Society of Civil Engineers (ASCE), "Report Card for America's Infrastructure," American Society of Civil Engineers, Reston, VA, 2013.
- [6] C. a. W. K. Nogueira, "Ultrasonic testing of damage in concrete under uniaxial compression," *ACI Materials J.*, vol. 98, no. 3, pp. 265-275, 2001.
- [7] A. Santos and D. Bray, "Comparison of acoustoelastic methods to evaluate stresses in steel plates and bars," *J. Pressure Vessel Technol.*, vol. 124, no. 3, pp. 354-358, 2002.
- [8] T. Voigt, Y. Akkaya and S. Shah, "Determination of early age mortar and concrete strength by ultrasonic wave reflections," *J. of Mater. In Civil Eng.*, vol. 15, no. 3, pp. 247-254, 2003.

- [9] P. Rizzo and F. Lanza di Scalea, "Effect of frequency on the acoustoelastic response of steel bars," *Experimental Techniques*, vol. 27, no. 6, pp. 40-43, 2006.
- [10] I. Lillamand, J. Chaix, M. Ploix and V. Garnier, "Acoustoelastic effect in concrete material under uni-axial compressive loading," *NDT&E International*, vol. 43, no. 8, pp. 655-660, 2010.
- [11] Y. Lu and J. Michaels, "Feature extraction and sensor fusion for ultrasonic structural health monitoring under environmental conditions," *IEEE Sensors Journal*, vol. 9, no. 11, pp. 1462-1471, 2009.
- [12] "NDT Resource Center," Collaboration for NDT Education, [Online]. Available: http://www.ndt-ed.org/EducationResources/CommunityCollege/Ultrasonics/cc_ut_index.htm. [Accessed 15 11 2013].
- [13] A. Guz' and F. Makhort, "The Physical fundamentals of the ultrasonic nondestructive stress," *International Applied Mechanics*, vol. 36, no. 9, pp. 1119-1149, 2000.
- [14] S. Chaki and G. Bourse, "Stress level measurement in prestressed steel strands using acoustoelastic effect," *Experimental Mechanics*, vol. 49, no. 5, pp. 673-681, 2008.
- [15] P. Antonaci, C. Bruno, A. Gliozzi and M. Scalerandi, "Monitoring evolution of compressive damage in concrete in concrete with linear and nonlinear ultrasonic methods," *Cement and Concrete Research*, vol. 40, no. 7, pp. 1106-1113, 2010.
- [16] H. Chung, "Effects of embedded steel bars upon ultrasonic testing of concrete," *Magazine of Concrete Research*, vol. 30, no. 102, pp. 19-25, 1978.
- [17] D. Hughes and J. Kelly, "Second-order elastic deformation of solids," *Phys. Rev.*, vol. 92, no. 5, pp. 1145-1149, 1953.
- [18] D. Egle and D. Bray, "Measurement of acoustoelastic and third-order elastic constants for rail steel," *J. Acoust. Soc. Am.*, vol. 60, no. 30, pp. 741-744, 1976.
- [19] R. Benson and V. Raelson, "Acoustoelasticity," *Prod. Eng.*, vol. 30, pp. 56-59, 1959.

- [20] R. Bergman and R. Shahbender, "Effect of statically applied stresses on the velocity of propagation of ultrasonic waves," *J. Appl. Phys.* , vol. 29, no. 12, pp. 1736-1738, 1958.
- [21] G. Johnson and G. Mase, "Acoustoelasticity in transversely isotopic materials," *J. Acoust. Soc. Am.* , vol. 75, no. 6, pp. 1741-1747, 1984.
- [22] D. Crecraft, "The measurement of applied and residual stresses in metals using ultrasonic waves," *J. Sound Vib.* , vol. 5, no. 1, pp. 173-192, 1966.
- [23] E. Imanishi, M. Sasabe and Y. Iwashimizu, "Experimental study on acoustical birefringence in stressed and slightly anisotropic materials," *J. Acoust. Soc. Am.* , vol. 71, no. 3, pp. 565-572, 1981.
- [24] N. Hsu, "Acoustical birefringence and use of ultrasonic-waves for experimental stress analysis," *Experimental Mechanics*, vol. 14, no. 5, pp. 169-176, 1974.
- [25] I. Shkolnik, "Effect of nonlinear response of concrete on its elastic modulus and strength," *Cement & Concrete Composites*, vol. 27, no. 7-8, pp. 747-757, 2005.
- [26] S. Gokhale, "Determination of applied stresses in rails using the acoustoelastic effect of ultrasonic waves," Texas A&M University, 2007.
- [27] F. Murnaghan, "Finite deformations of an elastic solid," *American Journal of Mathematics*, vol. 59, no. 2, pp. 235-260, 1937.
- [28] C. Payan, V. Garnier, J. Moysan and P. Johnson, "Determination of third order elastic constants in a complex solid applying coda wave interferometry," *Appl. Phys. Lett.*, vol. 94, no. 011904, pp. 1-3, 2009.
- [29] T. Wu and T. Lin, "The stress effect on the ultrasonic velocity variations of concrete under repeated loading," *ACI Materials J.* , vol. 95, no. 5, pp. 519-524, 1998.
- [30] S. Popovics, J. Rose and J. Popovics, "The Behavior of Ultrasonic Pulses in Concrete," *Cement and Concrete Research*, vol. 20, no. 2, pp. 259-270, 1990.

- [31] A. Shah and S. Hirose, "Nonlinear ultrasonic investigation of concrete damaged under uniaxial compression step loading," *Journal of Materials in Civil Engineering.*, vol. 22, no. 5, pp. 476-484, 2010.
- [32] Y. Zhang, O. Abraham, V. Tournat, A. Duff, B. Lascoup, A. Loukili, F. Grondin and D. O., "Validation of a thermal bias control technique for coda wave interferometry (CWI)," *Ultrasonics*, vol. 53, no. 3, pp. 658-664, 2013.
- [33] D. Muir, "One-sided ultrasonic determination of third order elastic constants using angle-beam acoustoelasticity measurements," Georgia Institute of Technology, 2009.
- [34] P. Theobald, B. Zeqiri and J. Avison, "Couplants and their influence on AE sensor sensitivity," *J. Acoustic Emission*, vol. 26, pp. 91-97, 2008.
- [35] X. Huang, D. Burns and M. Toksöz, "The effect of stress on the sound velocity in rocks: theory of acoustoelasticity and experimental measurements," Massachusetts Institute of Technology Earth Resources Laboratory, Cambridge, MA, 2001.
- [36] Y. Berthaud, "Damage measurements in concrete via an ultrasonic technique. Part I experiment," *Cement and Concrete Research*, vol. 21, no. 1, pp. 73-82, 1991.
- [37] P. Shokouhi, "Stress- and damage-induced changes in coda wave velocities in concrete," in *QNDE*, Denver, Colorado, 2012.
- [38] P. Shokouhi, A. Zoëga, H. Wiggenhauser and G. Fischer, "Surface wave velocity-stress relationship in uniaxially loaded concrete," *ACI Materials J.*, vol. 109, no. 2, pp. 131-139, 2012.
- [39] E. Larose and S. Hall, "Monitoring stress related velocity variation in concrete with a 2×10^{-5} relative resolution using diffuse ultrasound (L)," *J. Acoust. Soc. Am.*, vol. 125, no. 4, pp. 1853-1856, 2009.
- [40] S. Stähler, C. Sens-Schonfelder and E. Niederleithinger, "Monitoring stress changes in a concrete bridge with," *J. Acoust. Soc. Am.*, vol. 129, no. 4, pp. 1945-1952, 2011.

- [41] C. Payan, V. Garnier and J. Moysan, "Effect of water saturation and porosity on the nonlinear elastic response of concrete," *Cement and Concrete Research*, vol. 40, no. 3, pp. 473-476, 2009.
- [42] J. Cantrell and K. Salama, "Acoustoelastic characterisation of materials," *International Materials Reviews*, vol. 36, no. 4, pp. 125-145, 1991.
- [43] E. Niederleithinger and C. Wunderlich, "Influence of small temperature variations on the ultrasonic velocity in concrete," in *Denver, Colorado*, 2012.
- [44] N. Nikitina and L. Ostrovsky, "An ultrasonic method for measuring stresses in engineering materials," *Ultrasonics*, vol. 35, no. 8, pp. 605-610, 1998.
- [45] T. Philippidis and D. Aggelis, "Experimental study of wave dispersion and attenuation in concrete," *Ultrasonics*, vol. 43, no. 7, pp. 584-595, 2005.
- [46] M. Hernández, M. Izquierdo, A. Ibáñez, J. Anaya and L. Ulate, "Porosity estimation of concrete by ultrasonic NDE," *Ultrasonics*, vol. 38, no. 1-8, pp. 531-533, 2000.
- [47] Z. Lafhaj, M. Goueygou, A. Djerbi and M. Kaczmarek, "Correlation between porosity, permeability and ultrasonic parameters of mortar with variable water/cement ratio and water content," *Cement and Concrete Research*, vol. 36, no. 4, pp. 625-633, 2006.
- [48] M. Noguez, T. Jacquot and U. Hofmann, "Residual stress evaluation on industrial heavy plates by acoustical birefringence," in *WCNDT*, Montreal, CA, 2004.
- [49] R. Miller and E. Hill, *Nondestructive Testing Handbook Vol 6 Acoustic Emission Testing*, P. Moore, Ed., Columbus, OH: American Society of Nondestructive Testing, 2007.
- [50] R. Weaver and O. Lobkis, "Diffuse fields in ultrasonics and seismology," *Geophysics*, vol. 71, no. 4, pp. S15-S19, 2006.
- [51] R. Weaver and O. Lobkis, "Temperature dependence of diffuse field phase," *Ultrasonics*, vol. 38, no. 1-8, pp. 491-494, 2000.
- [52] R. Weaver, "Laboratory studies of diffuse waves in plates," *J. Acoust. Soc. A.*, vol. 79, no. 4, pp. 919-923, 1986.

- [53] D. Egle, "Diffuse wave fields in solid media," *J. Acoust. Soc. Am.*, vol. 70, no. 2, p. 476, 1981.
- [54] K. Aki, "Analysis of seismic coda of local earthquakes as scattered waves," *Journal of Geophysical Research*, vol. 74, no. 2, pp. 615-631, 1969.
- [55] G. Poupinet, W. Ellsworth and J. Frechet, "Monitoring Velocity Variations in the Crust Using Earthquake Doublets - an Application to the Calaveras Fault, California," *Journal of Geophysical Research*, vol. 89, no. NB7, pp. 5719-5731, 1984.
- [56] C. Hadziioannou, E. Larose, I. Coutant, P. Roux and M. Campillo, "Stability of monitoring weak changes in multiply scattering media with ambient noise correlation: laboratory experiments," *J. Acoust. Soc. Am.*, vol. 125, no. 6, p. 3688-3695, 2009.
- [57] R. Snieder, "The theory of coda wave interferometry," *Pure Appl. Geophys.*, vol. 163, no. 2-3, pp. 455-473, 2006.
- [58] O. Lobkis and R. Weaver, "On the emergence of the Green's function in the correlations of a diffuse field," *J. Acoust. Soc. Am.*, vol. 110, no. 6, pp. 3011-3017, 2001.
- [59] O. Lobkis and R. Weaver, "Coda-wave interferometry in finite solids: recovery of P-to-S conversion rates in an elastodynamic billiard," *Phys. Rev. Lett.*, vol. 90, no. 25, pp. 1-4, 2003.
- [60] D. Schurr, J. Kim, K. Sabra and L. Jacobs, "Damage detection in concrete using coda wave interferometry," *NDT&E International*, vol. 44, no. 8, pp. 728-735, 2011.
- [61] P. Shokouhi, "Stress- and damage-induced changes in coda wave velocities in concrete," in *QNDE*, Burlington, VT, 2012.
- [62] K. Worden, C. Farrar, G. Manson and G. Park, "The fundamental axioms of structural health monitoring," *Proc. R. Soc.*, vol. 463, no. 2082, pp. 1639-1664, 2007.
- [63] C. Grosse, "Quantitative zerstörungsfreie Prüfung von Baustoffen mittels Schallemissionsanalyse und Ultraschall," University of Stuttgart, Stuttgart, Germany, 1996.

- [64] G. McLaskey and S. Glaser, "Acoustic emission sensor calibration for absolute source measurements," *J. Nondestruct. Eval.*, vol. 31, no. 2, pp. 157-168, 2012.
- [65] Mathworks, "Signal Processing Toolbox: User's Guide (R2013b)," [Online]. Available: <http://www.mathworks.com/help/signal/ref/xcorr.html>. [Accessed 12 9 2013].
- [66] MathWorks, "Signal Processing Toolbox: User's Guide (R2013b)," [Online]. Available: <http://www.mathworks.com/help/signal/ref/mscohere.html>. [Accessed 12 9 2013].
- [67] P. Tua, S. Quek and Q. Wang, "Detection of cracks in plates using," *Smart Mater. Struct.*, vol. 13, no. 4, pp. 643-660, 2004.
- [68] J. Michaels and T. Michaels, "Detection of structural damage from the local temporal coherence of diffuse ultrasonic signals," *IEEE Transactions on Ultrasonics, Ferroelectrics, and Frequency Control*, vol. 52, no. 10, pp. 1769-1782, 2005.